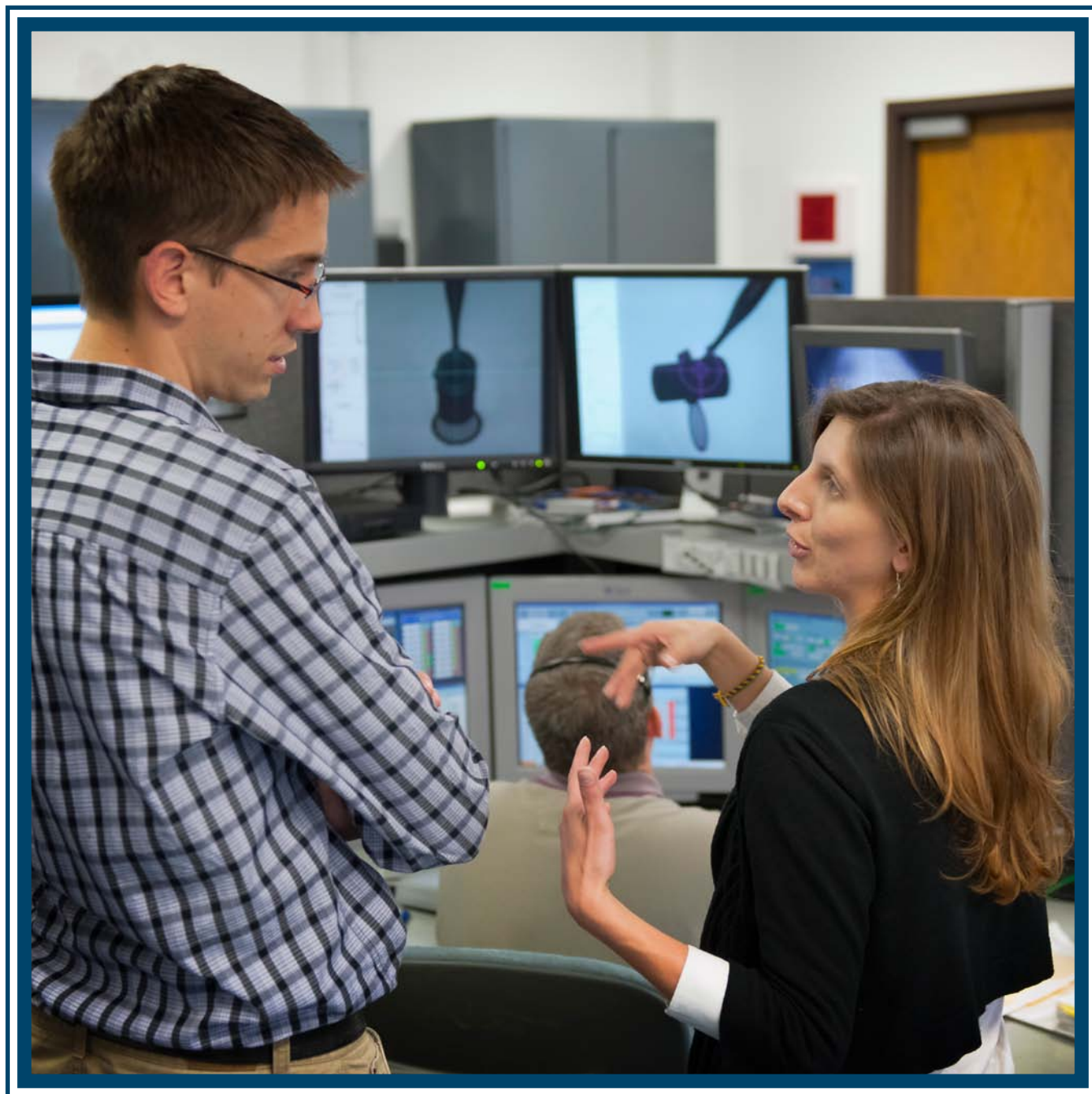


LLE Review

Quarterly Report



About the Cover:

The cover photo highlights Lawrence Livermore National Laboratory (LLNL) scientists Dr. Maria Barrios and Dr. Dayne Fratanduono discussing experimental details for shot campaigns being executed on the OMEGA Laser System. The scientists have worked on equation-of-state (EOS) measurements to characterize the high-pressure behavior of germanium-doped glow-discharge-polymer (GDP) ablator materials used for National Ignition Facility ignition targets as well as ramp-compression experiments for Fe and diamond. Robust ignition simulations require knowledge of the ablator equation of state. The article on p. 47 details the first EOS measurements on GDP and Ge-GDP films. The actual target setup displayed on the background video screen was used for the ramp-compression experiments.



The photo shows (from left to right) Dr. Thomas Boehly, Ph.D. advisor, and graduating students, Maria Barrios and Dayne Fratanduono, in their academic regalia at the University of Rochester's 2011 doctoral commencement. Dr. Barrios and Dr. Fratanduono are now working as scientists at LLNL; they continue to work collaboratively with Dr. Boehly and the Laboratory for Laser Energetics to study issues relevant to inertial confinement fusion and high-energy-density physics.

This report was prepared as an account of work conducted by the Laboratory for Laser Energetics and sponsored by New York State Energy Research and Development Authority, the University of Rochester, the U.S. Department of Energy, and other agencies. Neither the above named sponsors, nor any of their employees, makes any warranty, expressed or implied, or assumes any legal liability or responsibility for the accuracy, completeness, or usefulness of any information, apparatus, product, or process disclosed, or represents that its use would not infringe privately owned rights. Reference herein to any specific commercial product, process, or service by trade name, mark, manufacturer, or otherwise, does not necessarily constitute or imply its endorsement, recommendation, or favoring

by the United States Government or any agency thereof or any other sponsor. Results reported in the LLE Review should not be taken as necessarily final results as they represent active research. The views and opinions of authors expressed herein do not necessarily state or reflect those of any of the above sponsoring entities.

The work described in this volume includes current research at the Laboratory for Laser Energetics, which is supported by New York State Energy Research and Development Authority, the University of Rochester, the U.S. Department of Energy Office of Inertial Confinement Fusion under Cooperative Agreement No. DE-FC52-08NA28302, and other agencies.

Printed in the United States of America

Available from

National Technical Information Services
U.S. Department of Commerce
5285 Port Royal Road
Springfield, VA 22161
www.ntis.gov

For questions or comments, contact Amy L. Rigatti, Editor, Laboratory for Laser Energetics, 250 East River Road, Rochester, NY 14623-1299, (585) 275-8016.

www.lle.rochester.edu

LLE Review

Quarterly Report



Contents

| | |
|---|-----|
| In Brief | iii |
| Precision Equation-of-State Measurements on NIF Ablator Materials from 1 to 12 Mbar Using Laser-Driven Shock Waves..... | 47 |
| Refractive Index of Lithium Fluoride Ramp Compressed to 800 GPa | 59 |
| Hot-Electron Heating Caused by Two-Plasmon- Decay Instability | 66 |
| Fusion Yield Enhancement in Laser-Driven Magnetized Implosions..... | 80 |
| Amplifying Nanosecond Optical Pulses at 1053 nm with an All-Fiber Regenerative Amplifier..... | 85 |
| Analysis and Suppression of Parasitic Processes in Noncollinear Optical Parametric Amplifiers | 90 |
| Stress Compensation in Hafnia/Silica Optical Coatings by Inclusion of Alumina Layers | 100 |
| Publications and Conference Presentations | |

In Brief

This volume of the LLE Review, covering January–March 2011, features “Precision Equation-of-State Measurements on NIF Ablator Materials from 1 to 12 Mbar Using Laser-Driven Shock Waves” by M. A. Barrios and D. E. Fratanduono [LLNL (previously at LLE)]; T. R. Boehly (LLE); D. D. Meyerhofer (LLE and Departments of Mechanical Engineering and Physics, University of Rochester); and D. G. Hicks, J. H. Eggert, and G.W. Collins (LLNL). In this article, the authors present results to characterize the high-pressure behavior of germanium-doped glow-discharge polymer (Ge-GDP) ablators used for NIF ignition targets (p. 47). Robust ignition simulations require knowledge of the ablator equation of state (EOS) and this study details the first EOS measurements on GDP and Ge-GDP films. The experiments used laser-driven shock waves on OMEGA to provide impedance-matching conditions with α -quartz as the standard material. The use of quartz as the IM standard along with a time-resolved VISAR diagnostic facilitated measurement of shock velocities to $\sim 1\%$ precision in transparent materials, which, in turn, minimized measurement errors in GDP and Ge-GDP EOS results.

Additional highlights of research presented in this issue include the following:

- D. E. Fratanduono and M. A. Barrios [LLNL (previously at LLE)]; T. R. Boehly (LLE); D. D. Meyerhofer (LLE and Departments of Mechanical Engineering and Physics, University of Rochester); and J. H. Eggert, R. F. Smith, D. G. Hicks, P. M. Celliers, D. G. Braun, and G. W. Collins (LLNL) report on the refractive-index measurements of LiF using ramp compression to 800 GPa (p. 59). LiF was observed to remain transparent over a 30- to 800-GPa pressure range—the highest pressure under which a transparent insulator has ever been observed. The refractive index of compressed LiF was found to depend linearly on density, and an effective single-oscillator model infers that the pressure-induced band gap closes monotonically with increasing density. Extrapolation of these results indicate that ramp-compressed LiF may remain transparent to >4000 GPa, making LiF a valuable window for extremely high pressure ramp-compression experiments.
- J. F. Myatt, J. Zhang, J. A. Delettrez, A. V. Maximov, R. W. Short, W. Seka, and D. H. Edgell (LLE); D. F. DuBois and D. A. Russell (Lodestar Research Corp); and H. X. Vu (University of California, San Diego) describe the dynamics of hot-electron heating in direct-drive-implosion experiments caused by two-plasmon-decay (TPD) instability (p. 66). TPD was identified as a potential source of target preheat in direct-drive experiments on OMEGA, and a physical model of electron heating has been developed that relies on extended Zakharov simulations to predict the nonlinearly saturated Langmuir wave spectrum. Because of the relatively low areal density of the targets during the time of TPD instability, hot-electron recirculation and reheating are potentially important effects. These effects were modeled by using a particular form of boundary conditions on the test-particle trajectories. Adoption of these boundary conditions was shown to lead to an increase in the computed hot-electron temperature by a factor of $3\times$.
- P.-Y. Chang, G. Fiksel, M. Hohenberger, J. P. Knauer, R. Betti, F. J. Marshall (LLE); D. D. Meyerhofer (LLE and Departments of Mechanical Engineering and Physics, University of Rochester); and F. H. Séguin and R. D. Petrasso (MIT) summarize the fusion yield enhancement in laser-driven magnetized implosions (p. 80). A seed magnetic field of ~ 80 -kG strength was embedded into spherical inertial confinement fusion (ICF) targets imploded by the OMEGA laser in a polar-drive beam-pointing geometry. As a result of the target’s hot-spot magnetization, the electron radial heat losses were suppressed

and the observed ion temperature and neutron yield were enhanced by 15% and 30%, respectively. This data represents the first experimental verification of ICF target performance being enhanced by magnetizing the hot spot.

- R. Xin and J. D. Zuegel (LLE) investigate the amplification of nanosecond optical pulses at 1053 nm using a Yb-doped all-fiber regenerative amplifier (AFRA) operating with a repetition rate of 10.5 kHz (p. 85). The pulses were amplified from 15 pJ to 240 nJ, achieving an overall gain of 42 dB, and is believed to be the highest AFRA output-pulse energy ever reported. The sensitivity of the output-pulse energy with respect to amplifier parameters has been tested with numerical simulation suggesting that operation of the amplifier at saturation will greatly improve the output stability. The AFRA is an attractive candidate as a chirped-pulse–amplification (CPA) seed source because of its high output-pulse energy in comparison to seed pulses commonly used in existing CPA systems.
- J. Bromage, C. Dorrer, and J. D. Zuegel (LLE); and J. Rothhardt, S. Hadrich, C. Jocher, S. Demmler, J. Limpert, and A. Tunnermann (Friedrich Schiller University, Germany) review the suppression of parasitic processes in noncollinear optical parametric amplifiers (NOPA's) for walk-off and non-walk-off compensating configurations (p. 90). Modeling shows the second-harmonic generation of the signal can reduce the NOPA output energy by 10%. Quantitative measurements on an ultra-broadband, few-cycle NOPA support these findings in the walk-off compensating case and the effect is reduced by an order of magnitude in the non-walk-off compensating case. Additionally, a detailed phase-matching analysis for the most common nonlinear crystals is presented as a guide for designing NOPA systems.
- J. B. Oliver, P. Kupinski, A. L. Rigatti, A. W. Schmid, J. C. Lambropoulos, S. Papernov, A. Kozlov, C. Smith, and R. D. Hand (LLE) evaluate the stress compensation in hafnia/silica optical coatings by the inclusion of alumina layers (p. 100). Hafnia/silica films deposited using electron-beam evaporation tend to exhibit high tensile stresses when used in vacuum or low-relative-humidity environments resulting in film cracking or crazing. The inclusion of alumina layers within the film stack leads to a compressive overall film stress negating this failure mode in the dry-use environments. A film-stress model incorporating the stress of the individual materials and material thicknesses along with the interfacial film effects was developed to calculate the overall film stress when designing multilayer coatings using alumina, since this film stress (compressive) was measured to be very different than the alumina monolayer film stress (tensile). While the slow diffusion of water in alumina films present some manufacturing and operational challenges, a large-aperture hafnia/silica/alumina polarizer coating was fabricated and installed in the OMEGA EP short-pulse cavity location, eliminating the crazing issue observed with the previous films.

Amy L. Rigatti
Editor

Precision Equation-of-State Measurements on NIF Ablator Materials from 1 to 12 Mbar Using Laser-Driven Shock Waves

Introduction

Hydrocarbons are often used as ablator materials for inertial confinement fusion (ICF) studies, satisfying low-surface-roughness constraints and enabling one to introduce dopant atoms that are chemically bonded to the hydrocarbon, preventing its migration through the capsule shell.¹ One of three target ablator designs for the National Ignition Facility (NIF)² calls for glow-discharge polymer ($\text{CH}_{1.3}\text{O}_{0.02}$) (GDP) ablators with various levels of germanium doping (Ge-GDP).^{1,3–5} Introducing a mid-Z dopant reduces preheating of the fuel by increasing the opacity to hard x rays generated close to the coronal plasma; it also lowers the Atwood number.^{1,5} This helps to optimize target performance and relaxes manufacturing constraints.

Ultimately, each proposed NIF target design has its strengths and weaknesses, and the choice of ablator relies on detailed hydrodynamic simulations to specify the shell dimensions, dopant levels, and laser pulse. The aim is to produce a sufficiently robust design such that ignition will be achieved despite experimental uncertainties and hydrodynamic instabilities. These simulations require knowledge of the ablator equation of state (EOS), setting constraints on tolerable capsule surface roughness, ablator thickness, and driver energy. Instability growth rates have been shown to strongly depend on the ablator compressibility and first shock strength as defined by its EOS.^{1,6}

Results presented here form part of a larger study that was aimed at better understanding the behavior of hydrocarbon ablators and to characterize the high-pressure behavior of germanium-doped GDP for NIF ignition targets. Initially there was concern that variation in material properties among GDP and Ge-GDP batches could compromise results. With this in mind, the EOS of CH (polystyrene) and CH_2 (polypropylene), two materials whose fabrication process is well known and reproducible, were measured to high precision.⁷ This resolved uncertainties in the high-pressure (≥ 1 -Mbar) behavior of CH and provided measurements on the high-pressure effect of changes in stoichiometry by varying the H-to-C ratio, through EOS measurements of CH_2 . This provided the basis for interim

tabular model development that described GDP and Ge-GDP for ignition target designs.

Until now, the EOS of CH has been used as a surrogate EOS to model GDP ablators. In comparison to CH, however, GDP has a higher H-to-C ratio and trace amounts of oxygen, absorbed by the films during the fabrication process. Material properties such as initial density and index of refraction also differ between CH and GDP/Ge-GDP films. Although the EOS of CH is known to high precision,⁷ it is not sufficient to accurately describe the behavior of GDP and Ge-GDP. It is still necessary to verify how differences in stoichiometry and material properties influence the EOS of such materials and compare with model predictions.

This study presents the first EOS measurements on GDP and Ge-GDP. These experiments used laser-driven shock waves to provide impedance-matching (IM) conditions with α -quartz as the standard material.^{8,9} Previous studies successfully used quartz as a standard, demonstrating a significant reduction in measurement uncertainties.^{7,9,10} By using velocity interferometry and transparent materials, $\sim 1\%$ precision was obtained in shock-velocity measurements.¹¹ GDP and Ge-GDP data are compared with available LEOS (Livermore equation of state) models, showing close agreement between measurements and model predictions. The IM technique, its associated error analysis, and optimization-enabling precision measurements are discussed in the next section. The sections that follow describe the experimental configuration, targets, and diagnostics, followed by the results and concluding remarks.

Impedance-Matching Technique

The impedance-matching technique allows one to determine a sample's particle velocity (U_p), pressure (P), and density (ρ) through shock-velocity measurements in a reference material, here z -cut α -quartz ($U_{s,Q}$), and the sample being tested, i.e., GDP ($U_{s,GDP}$) or Ge-GDP ($U_{s,Ge-GDP}$).^{12,13} Mass and momentum are conserved as the shock front transits the contact interface between standard and sample. The Rankine–Hugoniot equations¹² are valid at the contact interface, implying U_p and P must be continuous across this boundary. Measurement of the

shock velocity in the standard, at the contact interface, yields the initial shock state from where the standard releases (given the standard has higher impedance than the sample, as in this case). By measuring the shock velocity in the sample, at the contact interface, one can determine the conditions at which the standard and sample equilibrate, yielding the $P(U_p)$ state.

In this study the IM analysis was performed using quartz's experimentally determined Hugoniot^{8,14} and a constant Grüneisen parameter (Γ) to calculate off-Hugoniot states, as previously described.^{7,14,15} Using quartz ($\rho_0 = 2.65 \text{ g/cm}^3$, $n = 1.547$) as an IM standard provides higher precision than opaque standards by reducing errors associated with the standard's initial state, from which off-Hugoniot curves are launched. It also relaxes shock-stability constraints since changes in shock velocity are directly measured and can be accounted for in the analysis. By measuring *in-situ* shock velocities, one can measure observables ($U_{s,Q}$, $U_{s,GDP}$, and $U_{s,Ge-GDP}$) close to the contact interface, where the IM conditions are valid.

Data precision obtained through the IM technique is strictly correlated to the accuracy with which the states in the standard are known. Although not often accounted for, systematic uncertainties enter the IM analysis through calculation of the standard's Hugoniot and off-Hugoniot states. Quartz's shock EOS was previously measured in a large pressure range (~2 to 15 Mbar) through impedance matching with aluminum (Al) standard, using laser-driven shock waves.⁸ These experiments were in agreement with previous gas-gun and nuclear and chemical explosive studies, displaying linear behavior in the U_s-U_p plane, given by a piecewise linear function of general form $U_s = a_0 + a_1(U_p - \beta)$,

$$U_s = (6.914 \pm 0.028)(1.667 \pm 0.038)(U_p - 11.865),$$

for $U_p < 6.358 \text{ } \mu\text{m/ns}$,

(1)

$$U_s = (19.501 \pm 0.068)(1.276 \pm 0.022)(U_p - 11.865),$$

for $U_p \geq 6.358 \text{ } \mu\text{m/ns}$,

(2)

where an orthonormal basis is used such that resulting errors are uncorrelated.¹⁴ This fit was used in this study's analysis.

Quartz's release states were approximated via a Mie-Grüneisen EOS as described in McQueen *et al.*¹⁵ Based on solid and porous silica Hugoniot measurements,^{8,14,16,17} quartz's Grüneisen parameter was shown to be nearly constant with $\Gamma = 0.66 \pm 0.1$. Model predictions in a similar pressure range

estimate the value to be $\Gamma = 0.64 \pm 0.11$ (Ref. 9), in agreement with experimental results. This analysis uses the model-based value for Γ and corresponds to the only model-based parameter entering this IM analysis. By using quartz experimental principal Hugoniot and a Mie-Grüneisen formalism to approximate release states, one can propagate systematic uncertainties inherent in the IM technique.

Random uncertainties enter the IM analysis through calculation of the standard and sample Rayleigh lines, $P = \rho_0 U_s U_p$, describing the thermodynamic path taken during compression in the $P-U_p$ plane. These errors often involve only shock-velocity measurement uncertainties; in the case of GDP and Ge-GDP, uncertainties in their initial densities were also accounted for, translating to an increase in random errors in comparison to previous precision EOS measurements.⁷ The total error associated with the measured U_p , P , and ρ corresponds to the quadrature sum of both random and systematic uncertainties.

IM calculations are often performed in the $P-U_p$ plane since both of these quantities must be continuous across the contact interface between the standard and sample. In the previously described framework, the final $P(U_p)$ is a function of nine parameters: a_{0L} , a_{0H} , a_{1L} , a_{1H} , Γ , ρ_{0Q} , ρ_{0CH_x} , $U_{s,Q}$, and U_{s,CH_x} , and their corresponding uncertainties. The first four variables are fitting parameters for the quartz principal Hugoniot, where subscripts L and H refer to the low ($U_p < 6.358 \text{ } \mu\text{m/ns}$) and high ($U_p \geq 6.358 \text{ } \mu\text{m/ns}$) fits. The fifth parameter corresponds to the model-dependent Grüneisen parameter, and the last four correspond to the quartz and sample initial density and measured shock velocity. Because quartz's experimentally derived principal Hugoniot and Grüneisen-based release can be considered independent, error contributions from each parameter are found by calculating deviations from the nominal U_p , P , and ρ results. Note that this amounts to eight error contributions since no error is assumed for quartz's initial density.

Recent work on the Sandia Z Machine measured the EOS of quartz in the 1- to 16-Mbar pressure regime,¹⁸ observing curvature in the U_s-U_p plane not present in the EOS used herein. If real, this difference in EOS would cause systematic shifts in the derived sample EOS. Although these discrepancies in the principal Hugoniot of quartz have yet to be resolved, it is important to acknowledge them since they apply to the IM analysis. This subject is discussed in **Appendix A**, p. 56.

Experimental Method

Experiments were performed on the OMEGA laser,¹⁹ a frequency-tripled Nd:glass laser that produces 351-nm light.

Shock pressures were generated using ~250 to 2100 J delivered in a nominally 2-ns square pulse. Focal-spot profiles were smoothed using distributed phase plates,²⁰ leading to a uniform irradiation area with a 600- or 800- μm diameter. This resulted in average irradiances on target of 0.24 to 2.5×10^{14} W/cm².

Experiments were conducted using multilayered 3-mm \times 3-mm planar targets, which had a 20- μm CH ablator designed to prevent preheating of the target by minimizing x rays generated in the coronal plasma and a 90- μm -thick pusher made of z-cut α -quartz, used as the standard material for IM. On the rear side of the pusher were two samples: ~30 μm of Ge-GDP on the top half of the target and ~30 μm of GDP on the bottom half of the target. This allowed for simultaneous EOS measurements of both materials in a single shot to be conducted.

Ideally the probe beam used to diagnose shock velocities reflects off only the moving shock front; in practice, the system can register back-reflections and internal reflections from the target layers, referred to as “ghost fringes.” To mitigate these effects, the free surface of all targets, that opposite the drive beams, had an antireflection coating to minimize ghost reflections. Because IM measurements are performed at the contact interface between standard and sample, glue layers between these materials were kept at a minimum, estimated to be no more than 1 to 2 μm thick. For some shots, the GDP and Ge-GDP films were directly deposited onto the α -quartz, requiring no glue layer.

GDP and Ge-GDP films were made and characterized in small batches by General Atomics (GA).²¹ Material properties of these films, such as stoichiometry, initial density, and index

of refraction, varied slightly among batches (of the order of 1% to 3%). These differences were taken into account in the data analysis and are summarized in Table 126.I. Elemental compositional stoichiometry was based on x-ray fluorescence (XRF) chemical analysis and XRF calculations. Average initial densities were obtained by measuring the volume and weight of each film batch. The film length and width were measured within 0.1 mm, and thicknesses were measured by interferometry techniques to within 0.5 μm , resulting in initial density uncertainties between 1% and 2%. For each batch, a separate sample fabricated from the same batch material was used to measure index of refraction. This sample was submerged in various Cargille Laboratories²² series A index-matching fluids. White-light interferometry with a 532-nm filter was used to determine the best match among the various index-matching fluids. The index of refraction for the matching fluid was verified using an Abbé refractometer, finding agreement to ± 0.0005 . Both the Abbé refractometer and the index-matching fluids were referenced to the sodium D line at $\lambda = 589.3$ nm (at 25°C). The Cauchy equation, with coefficients provided by the vendor, were used to find the index of refraction at $\lambda = 532$ nm. Uncertainties associated with index-of-refraction measurements arise from estimated fringe offsets and wavelength correction.

Shock velocities were measured using a line-imaging velocity interferometer system for any reflector (VISAR),¹¹ with an 800- μm field of view. Two interferometers with different sensitivities were used to discern the 2π phase-shift ambiguity occurring at fringe jumps and breakout times. Uncorrelated velocity sensitivities of 2.732 and 6.906 $\mu\text{m}/\text{ns}/\text{fringe}$ were produced by using etalons with 18- and 7-mm thickness, respec-

Table 126.I: Material properties and associated errors at ambient conditions for ablator material films, as obtained for each batch. The shot numbers that used each of the batches are also indicated below.

| Material | Formula | Ge (at. %) | ρ_0 (g/cm ³) | $n(\lambda = 532 \text{ nm})$ |
|----------|--------------------------------------|------------|-------------------------------|-------------------------------|
| GDP* | CH _{1.36} O _{0.01} | — | 1.06 \pm 0.02 | 1.571 \pm 0.005 |
| GDP† | CH _{1.38} O _{0.02} | — | 1.05 \pm 0.05 | 1.571 \pm 0.005 |
| GDP‡ | CH _{1.35} O _{0.01} | — | 1.044 \pm 0.005 | 1.563 \pm 0.010 |
| Ge-GDP§ | CH _{1.42} O _{0.04} | 0.7 | 1.13 \pm 0.05 | 1.572 \pm 0.005 |
| Ge-GDP† | CH _{1.43} O _{0.05} | 0.66 | 1.13 \pm 0.05 | 1.572 \pm 0.005 |
| Ge-GDP | CH _{1.40} O _{n/a} | 0.5 | 1.13 \pm 0.05 | 1.572 \pm 0.005 |
| Ge-GDP‡ | CH _{1.35} O _{0.01} | 0.5 | 1.10 \pm 0.05 | 1.570 \pm 0.010 |

*Shots 54126, 54127, 54185, 54187, 52635

†Shots 55774, 55775, 55777–55785

‡Shots 57162–57164

§Shots 54127, 54185, 54187, 52630

||Shots 56115–56118

tively, where the velocity sensitivity in each material varied based on its index of refraction. The dielectric materials used were subject to drive pressures in the Mbar range, generating reflective shock fronts. The VISAR probe laser—a *Q*-switched, injection-seeded Nd:YAG laser operating at 532 nm with an ~50-ns full width at half maximum (FWHM)—reflected off the shock front. This signal was relayed to the set of interferometers and recorded on streak cameras with a 15- or 9-ns temporal window (one for each VISAR), providing streak images with temporal and 1-D spatial resolution. Since the shock fronts were highly reflective, the measured Doppler-shifted signal detected by VISAR is directly correlated to the velocity of the shock wave. Streak images were post-processed using a fast Fourier transform (FFT) method,^{11,23} resolving fringe jumps to ~5% of a fringe. This translates to ~1% precision in shock-velocity measurements, with typical measurements resulting in five fringe shifts. Although the streak cameras had temporal resolutions close to 10 ps, the diagnostic temporal response was dominated by etalon delay times of either 90 or 40 ps.

The experimental configuration is shown in Fig. 126.1(a); the OMEGA¹⁹ beams irradiate the front of the target, with VISAR aligned opposite the drive beams perpendicular to the rear surface of the target. Because targets were composed of only transparent materials, VISAR provided a continuous shock-velocity history as the shock wave transited each target layer. Figure 126.1(b) shows a section of the VISAR streak image, corresponding to the bottom half of the target (GDP). Here the quartz was driven to a shock pressure of 8.6 Mbar, corresponding to 4.90 Mbar in GDP and 5.08 Mbar in Ge-GDP. In Fig. 126.1(b) the laser drive starts at $t = 0$ and the shock enters the quartz at ~0.6 ns. By ~2 ns the shock in the quartz has equilibrated with the ablation pressure and its velocity stabilizes considerably. At ~4.5 ns, the shock reaches the GDP sample and reaches the sample's rear surface at ~6 ns. It is clear from Fig. 126.1(b) that the quartz:GDP contact interface has finite temporal width at 4.5 ns, owing to the glue layer and VISAR temporal resolution of 40 or 90 ps. (The same is true for the quartz:Ge-GDP interface, not shown.) Consequently, shock velocities are not measured at the “true” contact interface between reference and sample, but at an earlier and later time, respectively. This is accounted for by linearly fitting the velocity profile over ~300 ps and extrapolating to the time where the true contact interface would be, here defined to be the equidistant (temporal) location between the quartz and sample boundary, shown as t' in Fig. 126.1(c). This methodology also accounts for any deceleration observed in the measurements, such that the IM conditions are still matched despite shock-wave decay. Figure 126.1(c) shows the shock-velocity histories

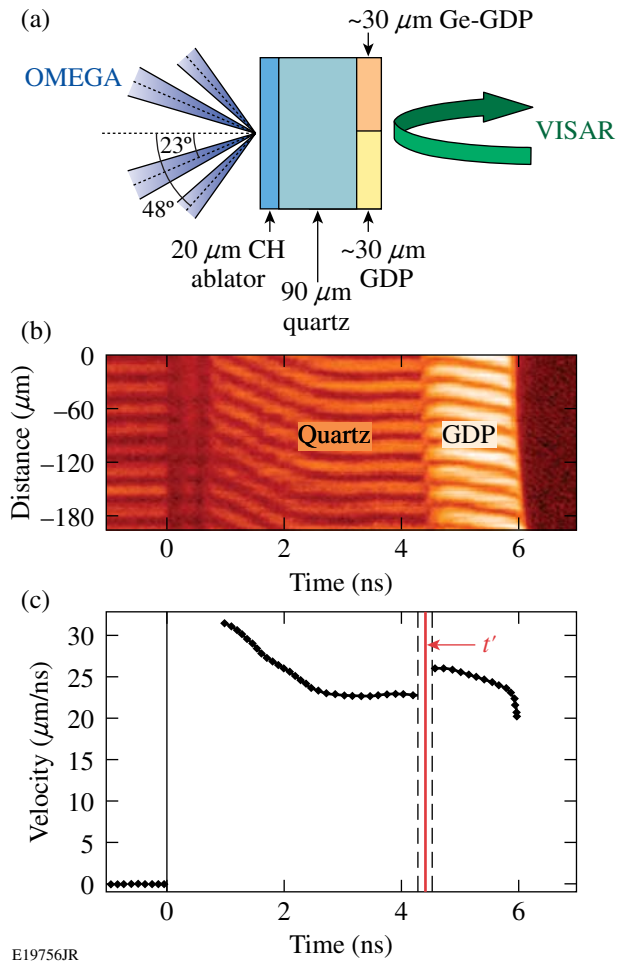


Figure 126.1

(a) Schematic of two material targets used in the experiments. Here the OMEGA beams irradiate the target at 23° and 48° to target normal, with VISAR aligned and focused to the rear surface of the target. Multilayer planar targets were composed of a CH ablator, quartz standard, and two different samples (GDP and Ge-GDP) to be tested. (b) VISAR streak image corresponding to the bottom half of the target, containing data for GDP, shows continuous tracking of the shock front within the standard and material being tested. (c) Final shock-velocity measurements in quartz and GDP after data extraction and analysis. For the IM analysis, shock velocities are evaluated at t' .

for quartz and GDP from the streak image data shown in Fig. 126.1(b), after applying the FFT and matching velocity solutions from both interferometers.

Results and Discussion

1. Glow-Discharge Polymer

Single-shock principal Hugoniot measurements for GDP were obtained from ~1 to 12 Mbar. Experimental observables and resulting kinematic properties for GDP are listed in Table 126.II. Results display a linear U_s-U_p relation, given by $U_s = (24.56 \pm 0.07) + (1.29 \pm 0.01)(U_p - 16.76)$. This fit was

obtained through a least-squares fit using an orthogonal polynomial basis, resulting in fitting parameters that are independent of each other, i.e., including higher-order terms does not affect the value of lower-order coefficients.²⁴ Because of this independence, the errors associated with such fitting parameters are independent. The initial density, compositional stoichiometry, and index of refraction of the samples varied between fabrication batches (Table 126.I); these variations were included in the analysis. Alterations of the high-pressure behavior caused by variations in initial parameters were not evident in the U_s - U_p plane; therefore, no distinction was made among the batches for the linear fit in this plane.

Recently an LEOS was developed for GDP (LEOS 5310). Current LEOS models are developed based on the quotidian equation of state (QEOS)²⁵-type construct, where an additive approach is taken to describe the Helmholtz free energy. The included components account for ion/nuclear and electron contributions, as well as semi-empirical bonding corrections, needed to obtain reasonable results for cold matter at or near solid density, or quantum or exchange corrections. Typically the electron contribution is calculated via a Thomas–Fermi model and the ion contribution via the Cowan EOS^{25,26} (an analytical model), combining ideal gas, fluid scaling laws, the Debye lattice theory, Grüneisen EOS, and the Lindenmann melt law.

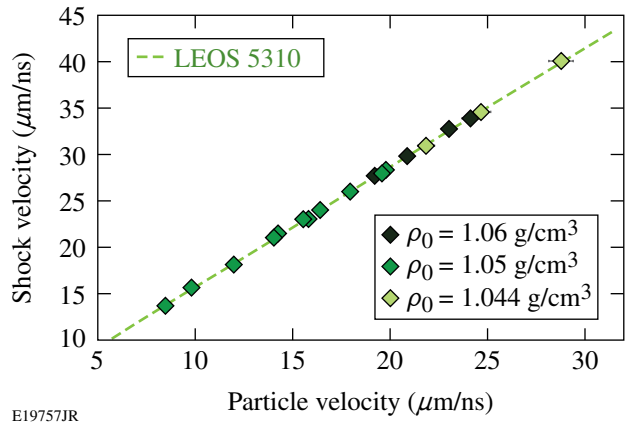
Table 126.II: Principal Hugoniot results for glow-discharge polymer (GDP) using the IM technique with quartz reference. Measured shock velocity with error is given for both quartz ($U_{s,Q}$) and GDP ($U_{s,GDP}$). The resulting particle velocity ($U_{p,GDP}$), pressure (P_{GDP}), and density (ρ_{GDP}) of shocked GDP are listed, with given random and systematic uncertainties. Random uncertainties enter the IM analysis through errors in shock-velocity measurements and initial density variations, while systematic errors stem from uncertainties in quartz's principal Hugoniot and release states.

| Shot | $U_{s,Q}$ ($\mu\text{m/ns}$) | $U_{s,GDP}$ ($\mu\text{m/ns}$) | $U_{p,GDP}$ (ran,sys) ($\mu\text{m/ns}$) | P_{GDP} (ran,sys) (Mbar) | ρ_{GDP} (ran,sys) (g/cm^3) |
|-------|-----------------------------------|-------------------------------------|---|-------------------------------|---|
| 55782 | 13.12±0.09 | 13.77±0.10 | 8.47(0.14,0.21) | 1.22(0.02,0.03) | 2.73(0.08,0.11) |
| 55783 | 14.42±0.11 | 15.72±0.10 | 9.81(0.16,0.22) | 1.62(0.03,0.03) | 2.79(0.08,0.12) |
| 55781 | 16.44±0.11 | 18.20±0.10 | 11.97(0.19,0.1) | 2.29(0.04,0.02) | 3.07(0.1,0.05) |
| 55780 | 18.64±0.10 | 21.08±0.10 | 14.03(0.2,0.13) | 3.11(0.04,0.03) | 3.14(0.09,0.06) |
| 55785 | 18.90±0.10 | 21.55±0.10 | 14.25(0.2,0.13) | 3.22(0.05,0.03) | 3.10(0.09,0.05) |
| 55779 | 20.24±0.10 | 23.09±0.10 | 15.53(0.21,0.15) | 3.77(0.05,0.04) | 3.21(0.1,0.07) |
| 55784 | 20.46±0.13 | 23.07±0.10 | 15.79(0.24,0.16) | 3.82(0.06,0.04) | 3.33(0.11,0.07) |
| 55778 | 21.12±0.09 | 24.06±0.10 | 16.39(0.22,0.17) | 4.14(0.06,0.04) | 3.29(0.1,0.07) |
| 55777 | 22.76±0.10 | 26.05±0.10 | 17.93(0.24,0.21) | 4.90(0.07,0.06) | 3.37(0.11,0.09) |
| 52635 | 24.14±0.10 | 27.77±0.10 | 19.20(0.15,0.24) | 5.65(0.05,0.07) | 3.44(0.07,0.1) |
| 55774 | 24.45±0.10 | 28.03±0.23 | 19.56(0.25,0.25) | 5.76(0.08,0.07) | 3.47(0.13,0.1) |
| 55775 | 24.68±0.11 | 28.38±0.11 | 19.76(0.26,0.26) | 5.89(0.08,0.08) | 3.46(0.11,0.1) |
| 54127 | 24.65±0.20 | 28.44±0.20 | 19.67(0.25,0.26) | 5.93(0.08,0.08) | 3.44(0.12,0.1) |
| 54187 | 25.90±0.11 | 29.87±0.15 | 20.87(0.16,0.29) | 6.61(0.06,0.09) | 3.52(0.08,0.11) |
| 57164 | 26.84±0.11 | 30.99±0.10 | 21.85(0.28,0.32) | 7.07(0.09,0.1) | 3.54(0.11,0.12) |
| 54126 | 28.19±0.12 | 32.79±0.16 | 23.01(0.18,0.35) | 8.00(0.07,0.12) | 3.55(0.08,0.13) |
| 54185 | 29.31±0.11 | 33.94±0.16 | 24.11(0.17,0.38) | 8.67(0.07,0.14) | 3.66(0.08,0.14) |
| 57162 | 29.80±0.10 | 34.63±0.10 | 24.66(0.31,0.40) | 8.91(0.11,0.14) | 3.63(0.12,0.15) |
| 57163 | 34.15±0.10 | 40.10±0.10 | 28.77(0.35,0.52) | 12.04(0.15,0.22) | 3.69(0.12,0.17) |

These equations are parameterized such that limiting values (at solid density, as ρ approaches ∞ , etc.) yield reasonable results and available experimental data are recovered.²⁵ The LEOS models improve on this construct by providing alternate treatments for the ionic thermal contribution and melt matching to ensure positive heat capacities, break points for cold-curve modification, a differentiable density-dependent Grüneisen parameter, and a more adequate treatment for low-density states via a soft-sphere model.²⁷ Because experimental EOS measurements for GDP were unavailable at the time LEOS 5310 was constructed, this model was benchmarked¹ using precision EOS measurements for CH⁷ in the high-pressure regime and previous CH gas-gun data at lower pressures,²⁸ where density scaling based on the equilibrium densities of CH and GDP was used where applicable.²⁷ Modeled GDP behavior was further constrained by generating data from CHEETAH, a thermochemical model.²⁷ LEOS 5310 does not include dissociation. The assumed initial density and stoichiometry for LEOS 5310 are listed in Table 126.III.

The H-to-C ratio and initial density of LEOS 5310 were slightly different than the GDP samples used in these experiments; differences varied by $\sim 1\%$, on average, for both parameters. Oxygen levels measured in the GDP films were quite small (O-to-C ratios of 0.01 and 0.02) and had no detectable effect on the material's high-pressure behavior since batches with different oxygen levels compared well in both the U_s-U_p and $P-\rho$ planes (see Figs. 126.2 and 126.3). The oxygen doping in the LEOS 5310 model is comparable to that found in the films.

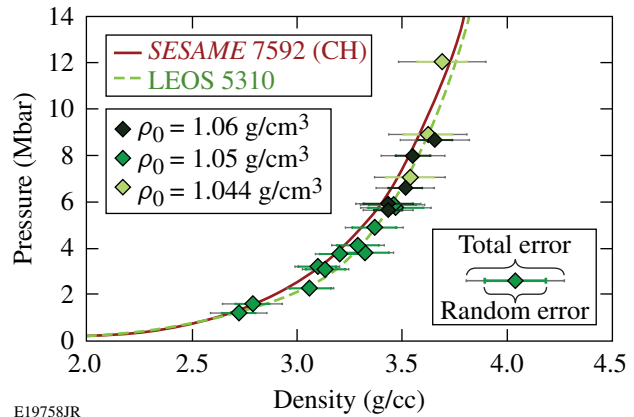
Figure 126.3 shows GDP results in the $P-\rho$ plane. Here, green (smaller) and gray (larger) error bars represent random and total errors, respectively. Material initial densities are distinguished by color shades as $\rho_0 = 1.06 \text{ g/cm}^3$, (dark green diamonds), 1.05 g/cm^3 (medium green diamonds), and 1.044 g/cm^3 (light green diamonds). Here the LEOS 5310 model was evaluated with initial density $\rho_0 = 1.05 \text{ g/cm}^3$, the average initial density between the GDP batches, for compari-



E19757JR

Figure 126.2

Principal Hugoniot measurements and models for GDP in the U_s-U_p plane. Data were obtained through the IM construct with quartz reference on GDP films with initial density $\rho_0 = 1.06$ (dark green diamonds), 1.05 (medium green diamonds), and 1.044 (light green diamonds) g/cm^3 .



E19758JR

Figure 126.3

Principal Hugoniot data and models for GDP in the $P-\rho$ plane, with GDP film's initial densities as previously described. Data are compared with CH SESAME 7592 (Ref. 30) and the LEOS 5310 model, evaluated at initial density $\rho_0 = 1.05 \text{ g/cm}^3$. Random uncertainties are shown as green (smaller) error bars and total uncertainties (quadrature of random and systematic uncertainties) as the black (larger) error bars.

Table 126.III: Initial density and stoichiometry for available LEOS models for GDP and Ge-GDP.

| Model | ρ_0 (g/cm^3) | Carbon (at. %) | Hydrogen (at. %) | Oxygen (at. %) | Germanium (at. %) |
|-----------|---------------------------------|-------------------|---------------------|-------------------|----------------------|
| LEOS 5310 | 1.04 | 42.34 | 57.15 | 0.51 | 0 |
| LEOS 5312 | 1.053 | 42.25 | 57.04 | 0.51 | 0.2 |
| LEOS 5315 | 1.073 | 42.12 | 56.87 | 0.505 | 0.5 |

son. *SESAME 7592* (Ref. 29), the CH *SESAME* model that best fit the precision polystyrene data, is shown as a reference. Data are in close agreement with LEOS 5310 model predictions and are only slightly softer than *SESAME 7592*, showing that GDP behaves quite similarly to CH in the high-pressure fluid regime. In this plane, it is also evident that data precision is degraded in comparison to previous precision EOS studies, yielding 3.4% to 5.6% precision in density. This is due to the inclusion of initial density uncertainties, which accounted for anywhere between 5.2% to 44% of the total density error.

2. Germanium-Doped GDP

Germanium-doped GDP (Ge-GDP) was studied in the ~1- to 12-Mbar pressure range. Table 126.IV presents shock-velocity measurements and kinematic properties obtained through the IM technique using quartz standard. With the exception of one batch, the initial density and index of refraction of the Ge-GDP films were consistent (Table 126.I), although levels of Ge doping varied from 0.5% to 0.7%. The equation of state of Ge-GDP in the U_s-U_p plane (shown in Fig. 126.4) displays a linear relation given by $U_s = (23.39 \pm 0.07) + (1.31 \pm 0.01)(U_p - 15.92)$. Here

Table 126.IV: Principal Hugoniot results for germanium-doped glow-discharge polymer (Ge-GDP) using the IM technique with quartz reference. Measured shock velocities in quartz ($U_{s,Q}$) and GDP ($U_{s,Ge-GDP}$) are given with measured error. The resulting particle velocity ($U_{p,Ge-GDP}$), pressure (P_{Ge-GDP}), and density (ρ_{Ge-GDP}) of shocked Ge-GDP are listed with random and systematic uncertainties associated with each measurement. Random uncertainties enter the IM analysis through errors in shock-velocity measurements and initial density variations; systematic errors stem from uncertainties in quartz's principal Hugoniot and release states.

| Shot | $U_{s,Q}$ ($\mu\text{m/ns}$) | $U_{s,Ge-GDP}$ ($\mu\text{m/ns}$) | $U_{p,Ge-GDP}$ (ran,sys) ($\mu\text{m/ns}$) | P_{Ge-GDP} (ran,sys) (Mbar) | ρ_{Ge-GDP} (ran,sys) (g/cm^3) |
|-------|-----------------------------------|--|--|----------------------------------|--|
| 55782 | 12.98±0.11 | 13.56±0.09 | 8.20(0.15,0.21) | 1.26(0.02,0.03) | 2.86(0.09,0.11) |
| 55783 | 14.50±0.09 | 15.21±0.11 | 9.83(0.14,0.22) | 1.69(0.03,0.04) | 3.20(0.1,0.14) |
| 55781 | 15.97±0.10 | 17.28±0.12 | 11.37(0.17,0.11) | 2.22(0.04,0.02) | 3.3(0.11,0.06) |
| 55780 | 18.64±0.10 | 20.76±0.11 | 13.83(0.19,0.12) | 3.25(0.05,0.03) | 3.38(0.1,0.06) |
| 55785 | 18.84±0.10 | 20.87±0.27 | 14.04(0.19,0.12) | 3.31(0.05,0.03) | 3.45(0.15,0.06) |
| 56118 | 19.24±0.11 | 21.18±0.09 | 14.44(0.2,0.13) | 3.46(0.05,0.03) | 3.55(0.11,0.07) |
| 55779 | 20.29±0.10 | 22.5±0.11 | 15.41(0.2,0.15) | 3.92(0.05,0.04) | 3.59(0.11,0.08) |
| 55784 | 20.44±0.12 | 22.81±0.10 | 15.53(0.22,0.15) | 4.00(0.06,0.04) | 3.54(0.11,0.07) |
| 55778 | 20.91±0.10 | 23.53±0.19 | 15.94(0.21,0.16) | 4.24(0.06,0.04) | 3.5(0.12,0.07) |
| 55777 | 22.66±0.10 | 25.53±0.16 | 17.59(0.23,0.2) | 5.08(0.07,0.06) | 3.64(0.12,0.09) |
| 56117 | 23.37±0.09 | 26.53±0.11 | 18.23(0.23,0.21) | 5.46(0.07,0.06) | 3.61(0.11,0.09) |
| 52630 | 24.18±0.10 | 27.35±0.10 | 19.02(0.24,0.24) | 5.88(0.07,0.07) | 3.71(0.11,0.10) |
| 55774 | 24.34±0.10 | 27.87±0.11 | 19.11(0.24,0.24) | 6.02(0.08,0.07) | 3.59(0.11,0.10) |
| 55775 | 24.5±0.12 | 27.76±0.12 | 19.31(0.25,0.24) | 6.06(0.08,0.08) | 3.71(0.12,0.11) |
| 54127 | 24.7±0.10 | 28.02±0.18 | 19.49(0.24,0.25) | 6.17(0.08,0.08) | 3.71(0.13,0.11) |
| 57164 | 27.04±0.10 | 31.14±0.11 | 21.78(0.27,0.31) | 7.45(0.09,0.11) | 3.65(0.11,0.12) |
| 56116 | 26.82±0.10 | 30.75±0.20 | 21.45(0.26,0.30) | 7.45(0.1,0.10) | 3.73(0.12,0.12) |
| 54185 | 29.22±0.09 | 33.72±0.09 | 23.67(0.28,0.36) | 9.02(0.11,0.14) | 3.79(0.11,0.14) |
| 57162 | 29.90±0.10 | 34.57±0.15 | 24.47(0.29,0.39) | 9.29(0.12,0.15) | 3.76(0.12,0.15) |
| 56115 | 31.80±0.10 | 36.65±0.10 | 26.12(0.31,0.44) | 10.82(0.13,0.18) | 3.93(0.12,0.16) |
| 57163 | 33.89±0.10 | 39.64±0.14 | 28.20(0.33,0.50) | 12.27(0.15,0.22) | 3.80(0.12,0.17) |

a least-squares fitting with an orthonormal basis was used. In this figure Ge-GDP data are compared to available models for Ge-doped GDP, LEOS 5312, and LEOS 5315 with assumed 0.2% and 0.5% Ge doping. These models display a similar behavior in this plane and are in agreement with measured data. LEOS 5312 and 5315 models for Ge-GDP were developed in a similar fashion as previously described for LEOS 5310. Because CHEETAH was not equipped to model Ge at the time, Si was used instead. LEOS 5315 and 5312 were developed independently; therefore the fit to the CHEETAH model is different for these models (LEOS 5310 and 5315 share the same fit). This is evident in the P - ρ plane (Fig. 126.5), where

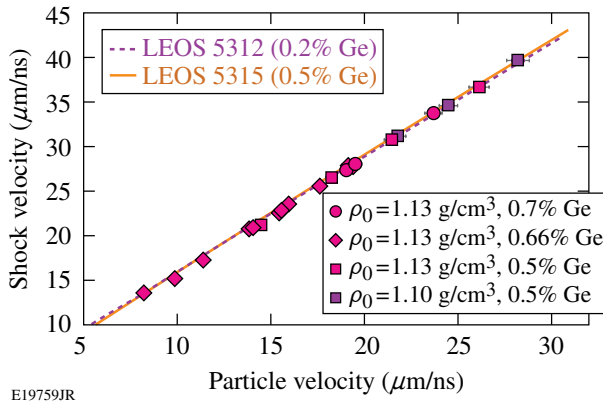


Figure 126.4
Principal Hugoniot measurements and models for Ge-GDP in the U_s-U_p plane. Data were obtained through the IM construct with quartz reference on Ge-GDP films with initial density $\rho_0 = 1.13 \text{ g/cm}^3$ (magenta circles, squares, and diamonds) and 1.10 g/cm^3 (purple squares), where circles, diamonds, and squares represent 0.7%, 0.66%, and 0.5% Ge doping.

the models cross at $\sim 2 \text{ Mbar}$. Like LEOS 5310, LEOS 5312 and 5315 do not include a dissociation model.²⁷ Development of LEOS models for GDP and Ge-GDP is an ongoing effort. Much of the difficulty in developing models that accurately describe material behavior over a wide range of states, in this case, is a lack of experimentally measured properties, which need to be inferred through codes such as CHEETAH or approximated using measured quantities of similar materials. Future LEOS table series, sharing the same fit to CHEETAH results, will include a dissociation model, have more stringent constraints to release states, and include new material response measurements as they become available, including this work. Material properties assumed by LEOS 5312 and 5315, such as initial density and compositional stoichiometry, are listed in Table 126.III.

The total uncertainty in density was between 3.5% and 5.4%, of which 7.2% to 40% was due to the Ge-GDP initial density error contribution, varying as a function of pressure. Figure 126.5 shows Ge-GDP EOS results in the P - ρ plane. Here samples with initial density of 1.13 g/cm^3 are shown as magenta circles (Ge at 0.7%), diamonds (Ge at 0.7%), and squares (Ge at 0.5%), while data taken on samples with initial density of 1.10 g/cm^3 are shown as purple squares (Ge at 0.5%). Random errors are shown as the colored error bars, which included shock velocity (in Ge-GDP and quartz) and initial density uncertainties. Total errors, representing the quadrature sum of random and systematic uncertainties, are shown as gray error bars. Data are compared with LEOS 5312 and LEOS 5315, both evaluated at an initial density of 1.13 g/cm^3 . LEOS 5310, evaluated at $\rho_0 = 1.05 \text{ g/cm}^3$, and *SESAME 7592* are plotted on this figure as a reference. On average, the percent differ-

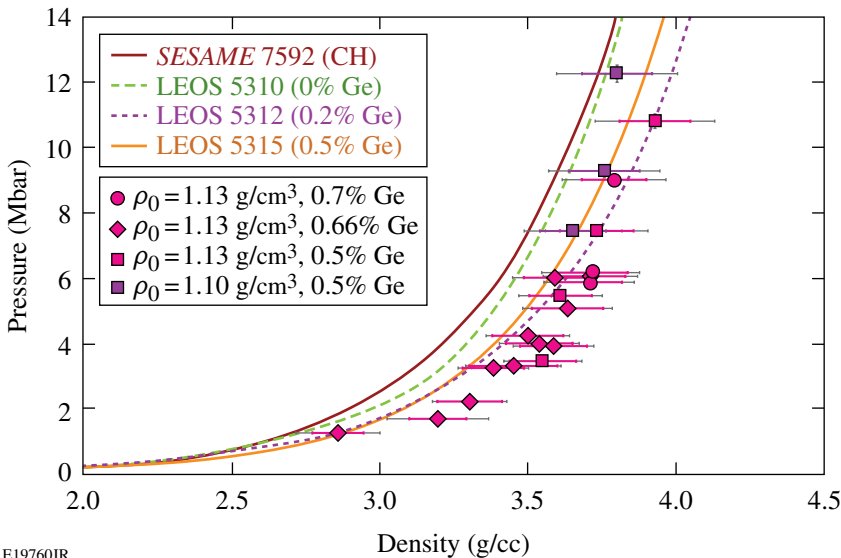


Figure 126.5
Principal Hugoniot data and models for Ge-GDP in the P - ρ plane, with Ge-GDP film initial densities and Ge doping as previously described. Data are compared with Ge-GDP available LEOS models, evaluated at an initial density $\rho_0 = 1.13 \text{ g/cm}^3$. Models used to compare with GDP data are included as reference. Random uncertainties are shown as the colored (shorter) error bars and total uncertainties (quadrature of random and systematic uncertainties) as the gray (longer) error bars.

ence between the model and sample H-to-C ratio was ~3.5%, although it varied up to 5.6%, and oxygen levels assumed in the models were smaller than those measured. Despite these differences, Fig. 126.5 shows that the data follow similar trends and agree with model predictions within experimental error. Between 2 and 4 Mbar, a slight softening of the data compared to model predictions is observed. Above these pressures, the Ge-GDP data begin to stiffen (becoming less compressible), approaching closer agreement with theoretical models. Although differences among models are amplified in the P - ρ plane, the data presented here are not able to discriminate between models because of random uncertainties.

Plotting the Ge-GDP results in the pressure-compression (P - ρ/ρ_0) plane (see Fig. 126.6) shows a smooth trend in close agreement with LEOS models for all pressures, i.e., no stiffening as observed in the P - ρ plane. The apparent stiffness at higher pressures observed in the P - ρ plane results from initial density variations. Ge-GDP was observed to undergo compression between $2.5\times$ and $3.4\times$, comparable to those reached by GDP, as shown in Fig. 126.7 (the composite results from both materials). Even with the fairly high precision of these measurements, the errors in the data make it difficult to favor any model behavior in this plane, even at the highest pressures, where models differ most.

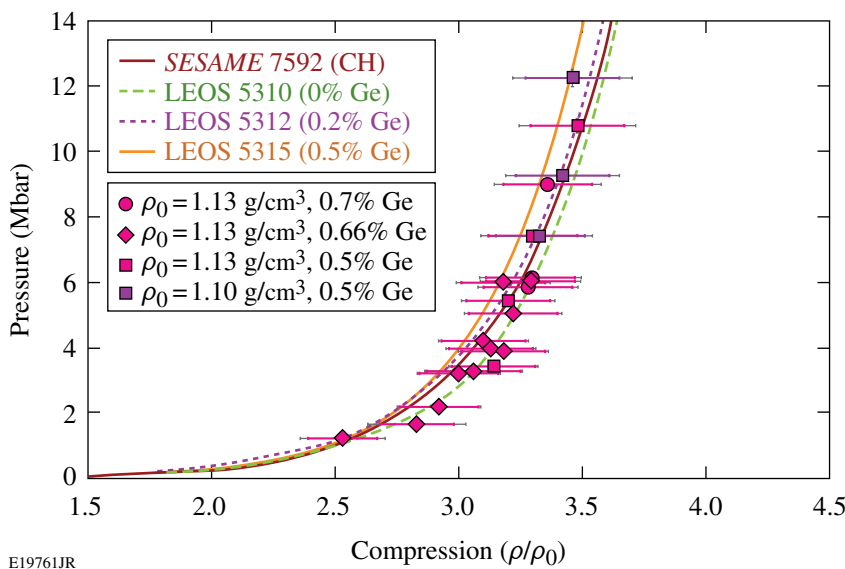


Figure 126.6
Ge-GDP results in the pressure-compression plane, with models and data as described in previous figures, showing structure observed in the P - ρ plane is likely due to initial density variations.

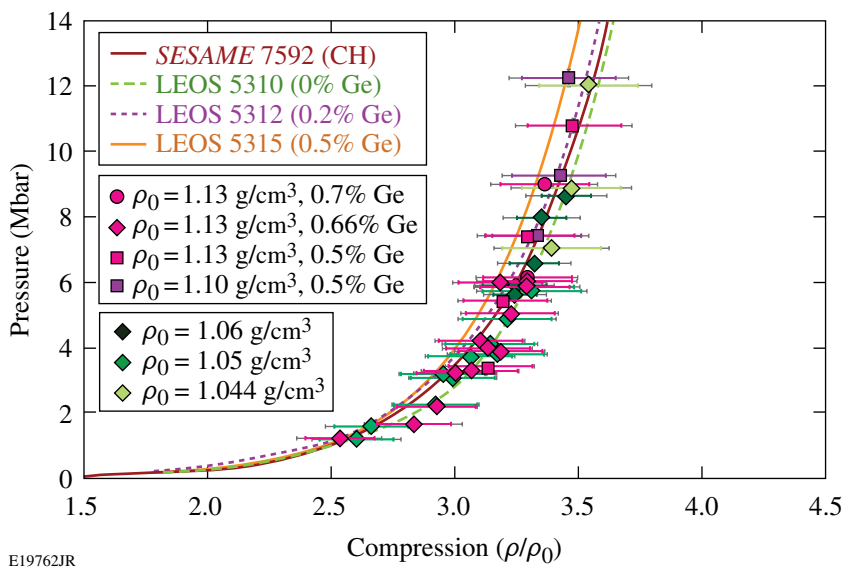


Figure 126.7
Results in the pressure-compression plane show that Ge-GDP and GDP reach similar compression states.

Conclusions

The high-pressure behavior of GDP and Ge-GDP was measured at shock pressures of ~ 1 to 12 Mbar. The use of quartz as the IM standard along with a time-resolved VISAR diagnostic facilitated the measurement of shock velocities to $\sim 1\%$ precision in transparent materials. This reduced the uncertainties in the initial shock state of quartz, in turn minimizing measurement errors in the GDP and Ge-GDP EOS results. Using quartz's experimentally derived principal Hugoniot and a Mie–Grüneisen EOS, systematic uncertainties inherent in the IM technique were accounted for in the analysis. Density uncertainties of 3.4% to 5.6% (GDP) and 3.5% to 5.4% (Ge-GDP) incorporate initial density variations in the samples. The initial density error contribution varies as a function of pressure and estimated error value, contributing up to 40% of the total error in the GDP and Ge-GDP density measurements.

GDP results are in close agreement with the LEOS 5310 model in both the U_s-U_p and $P-\rho$ planes, despite differences in stoichiometry of $\sim 1\%$. Likewise, data indicate that GDP behaves similarly to CH when shocked to greater than ~ 1 Mbar, displaying only a slight softness at higher pressures in comparison to this material. The effect of germanium doping on GDP samples is predicted reasonably well by available LEOS models, which are in agreement with measured Ge-GDP results, despite differences in assumed material. The compressibility of Ge-GDP on the Hugoniot is well predicted by both LEOS 5312 and LEOS 5315, although data are not able to discriminate between the two models.

ACKNOWLEDGMENT

The authors would like to thank the Omega Laser Facility personnel for their professionalism and outstanding work that enabled us to perform these experiments. This work was supported by the U.S. Department of Energy Office of Inertial Confinement Fusion under Cooperative Agreement No. DE-FC52-08NA28302, the University of Rochester, and the New York State Energy Research and Development Authority. The support of DOE does not constitute an endorsement by DOE of the views expressed in this article.

Appendix A: Influence of Quartz as a Standard

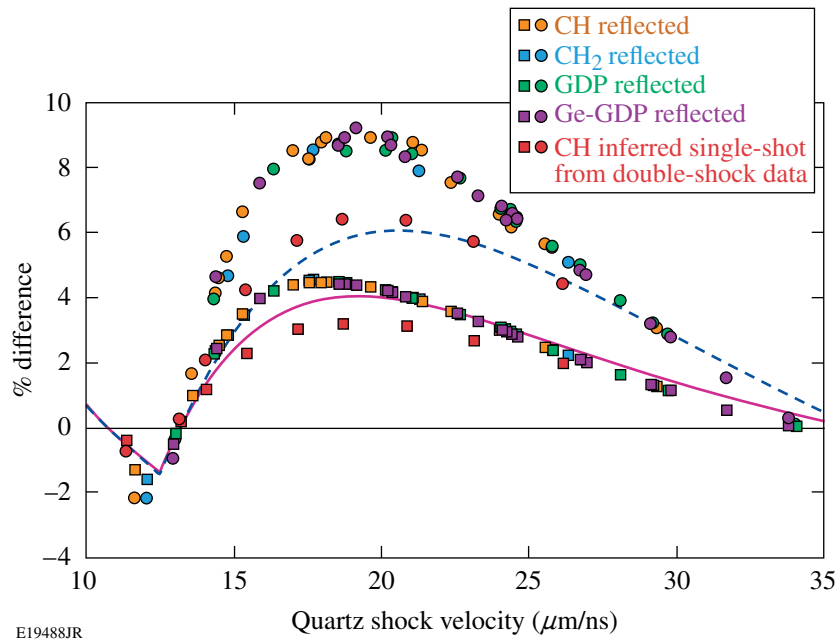
An uncertainty exists in the measured behavior of GDP and Ge-GDP as a result of discrepancies in the measured quartz EOS. Recent experiments performed on the Sandia Z Machine by Knudson *et al.*¹⁸ observed noticeable curvature in its $U_s(U_p)$ relation, previously observed to be linear in laser experiments.⁸ Since IM results are relative to the reference material, we present here an assessment of the effects of a different quartz EOS, were the Knudson result to be accurate.

The EOS of quartz enters the IM analysis through the principal Hugoniot and the off-Hugoniot (release) states. The

analysis presented in this study approximates release states using a Mie–Grüneisen EOS; this assumes Γ is independent of density such that Γ/V is constant. A curvature in the U_s-U_p plane could imply a non-constant Γ , having consequences in the methods used to calculate releases for IM calculations. Γ could also remain independent of density but would likely have a different value than that used in this study.

To compare both fits on an equal basis, the reflected-Hugoniot approximation was used to arrive at IM results for both cases, using measured quantities from CH, CH₂, GDP, and Ge-GDP experiments. Although the reflected Hugoniot is not a highly accurate approximation, for the pressures and material properties under consideration, the interest herein is in the *differences* among IM results, as a consequence of applying each quartz model. The percent differences in the CH, CH₂, GDP, and Ge-GDP density and pressure are shown in Fig. 126.8. Here a positive percent difference indicates the quartz fit obtained through laser data leads to larger pressure or density values, in comparison to the Z-machine quartz fit. The dashed blue and magenta curves represent the percent differences in density and pressure between the two quartz fits, peaking at $\sim 4\%$ and 6% in pressure and density. The orange, light blue, green, and purple circles and squares represent the percent differences in density and pressure for CH, CH₂, GDP, and Ge-GDP, respectively. This analysis groups together deviations in quartz's initial shock state and deviations between estimated release curves. Because these materials have similar impedances, the percent differences follow similar trends as a function of pressure (shock velocity), peaking at comparable quartz shock velocities. For these materials, maximum deviations in pressure and density were found to be $\sim 4.4\%$ and 8.8% at quartz shock velocities of 18 to 19 $\mu\text{m/ns}$, corresponding to hydrocarbon pressures of ~ 3.5 Mbar. On the other hand, percent differences in density and pressure were as low as 0.04% and 0.02%, respectively, and did not exceed more than 2% in both density and pressure (differences here arise from lowest and highest pressures accessed for each material). Considering precision EOS measurements presented have density precision between $\sim 3.5\%$ and 5.6%, Fig. 126.8 shows IM EOS states in hydrocarbons resulting from quartz states with $U_{s,Q}$ between 15 and 25 $\mu\text{m/ns}$, showing percent differences larger than 5.6%, would be most compromised.

Systematics between the two quartz fits can also be compared through inferred single-shock states from double-shock measurements. This inversion method was previously described by Hicks *et al.*³⁰ and was applied to double-shock measurements made on CH, yielding inferred single-shock states in



E19488JR

Figure 126.8

Percent differences between quartz model predictions in density and pressure, as a function of quartz shock velocity, are shown as the dashed blue and solid magenta curves. Circles and squares represent percent differences in density and pressure between IM results, assuming a reflected Hugoniot to calculate release states in quartz (orange, light blue, green, and purple circles and squares) and from inferred single-shock states using double-shock measurements (red circles and squares). Here a positive number means that a higher value is predicted using laser quartz fit in comparison to the Z-machine fit.

agreement with single-shock measurements.⁷ This method uses a model-averaged effective gamma to calculate off-Hugoniot states (in this case the CH re-shock), using the quartz fit only to establish the double-shock particle velocity and pressure. Percent differences resulting from using a different quartz model are shown in Fig. 126.8 as the red circles (density) and squares (pressure). This method yields more optimistic results, with percent differences in density and pressure peaking at 6.3% and 3.2%. In this case IM EOS states in hydrocarbons resulting from quartz shock states corresponding to $U_{s,Q}$ from 17.5 to 23 $\mu\text{m/ns}$ (with percent difference larger than 5.6%) would be most compromised. This corresponds to a smaller range than that predicted by the reflected Hugoniot analysis. Here quartz's influence enters only through the double-shocked pressure and particle velocity in CH.

The use of quartz as a standard in the IM technique has greatly improved the precision of EOS measurements, demonstrating the ability to provide EOS data that are able to more tightly constrain the high-pressure behavior of materials.^{7,9} A new equation of state of quartz could generate differences in the final EOS results but would not compromise the precision of these data.

REFERENCES

1. D. S. Clark *et al.*, *Phys. Plasmas* **17**, 052703 (2010).
2. G. H. Miller, E. I. Moses, and C. R. Wuest, *Nucl. Fusion* **44**, S228 (2004).
3. S. W. Haan *et al.*, *Phys. Plasmas* **2**, 2480 (1995).
4. T. R. Dittrich *et al.*, *Phys. Plasmas* **6**, 2164 (1999).
5. S. W. Haan *et al.*, *Phys. Plasmas* **12**, 056316 (2005).
6. B. A. Hammel *et al.*, *High Energy Density Phys.* **6**, 171 (2010).
7. M. A. Barrios, D. G. Hicks, T. R. Boehly, D. E. Fratanduono, J. H. Eggert, P. M. Celliers, G. W. Collins, and D. D. Meyerhofer, *Phys. Plasmas* **17**, 056307 (2010).
8. D. G. Hicks, T. R. Boehly, P. M. Celliers, J. H. Eggert, E. Vianello, D. D. Meyerhofer, and G. W. Collins, *Phys. Plasmas* **12**, 082702 (2005).
9. D. G. Hicks, T. R. Boehly, P. M. Celliers, D. K. Bradley, J. H. Eggert, R. S. McWilliams, R. Jeanloz, and G. W. Collins, *Phys. Rev. B* **78**, 174102 (2008).
10. N. Ozaki *et al.*, *Phys. Plasmas* **16**, 062702 (2009).
11. P. M. Celliers, D. K. Bradley, G. W. Collins, D. G. Hicks, T. R. Boehly, and W. J. Armstrong, *Rev. Sci. Instrum.* **75**, 4916 (2004).

12. Ya. B. Zel'dovich and Yu. P. Raizer, in *Physics of Shock Waves and High-Temperature Hydrodynamic Phenomena*, edited by W. D. Hayes and R. F. Probstein (Dover Publications, Mineola, NY, 2002), Vol. II, Chap. XI, pp. 685–784.
13. P. M. Celliers *et al.*, *J. Appl. Phys.* **98**, 113529 (2005).
14. D. G. Hicks S. Brygoo, P. Loubeyre, J. Eggert, R. S. McWilliams, P. M. Celliers, T. R. Boehly, and G. W. Collins (unpublished).
15. R. G. McQueen, Los Alamos National Laboratory, Los Alamos, NM, LA-UR-90-1996 (1989).
16. R. F. Trunin, *Shock Compression of Condensed Materials* (Cambridge University Press, Cambridge, England, 1998).
17. R. F. Trunin, *Phys.-Usp.* **37**, 1123 (1994).
18. M. D. Knudson and M. P. Desjarlais, *Phys. Rev. Lett.* **103**, 225501 (2009).
19. T. R. Boehly, R. S. Craxton, T. H. Hinterman, J. H. Kelly, T. J. Kessler, S. A. Kumpan, S. A. Letzring, R. L. McCrory, S. F. B. Morse, W. Seka, S. Skupsky, J. M. Soures, and C. P. Verdon, *Rev. Sci. Instrum.* **66**, 508 (1995).
20. Y. Lin, T. J. Kessler, and G. N. Lawrence, *Opt. Lett.* **20**, 764 (1995).
21. Project Staff, General Atomics, San Diego, CA, General Atomics Report GA-A26403 (2009).
22. Cargille Laboratories, Inc., Cedar Grove, NJ 07009 (<http://www.cargille.com/refractivestandards.shtml>).
23. M. Takeda, H. Ina, and S. Kobayashi, *J. Opt. Soc. Am.* **72**, 156 (1982).
24. P. R. Bevington and D. K. Robinson, *Data Reduction and Error Analysis for the Physical Sciences*, 3rd ed. (McGraw-Hill, Boston, 2003).
25. R. M. More *et al.*, *Phys. Fluids* **31**, 3059 (1988).
26. G. I. Kerley, Sandia National Laboratory, Albuquerque, NM, Report SAND-88-2291, NTIS Order No. DE91017717 (1991).
27. P. Sterne, Lawrence Livermore National Laboratory, private communication (2011).
28. S. P. Marsh, ed. *LASL Shock Hugoniot Data*, Los Alamos Series on Dynamic Material Properties (University of California Press, Berkeley, CA, 1980).
29. S. P. Lyon and J. D. Johnson, Los Alamos National Laboratory, Los Alamos, NM, Report LA-UR-92-3407, NTIS Order No. DE85014241 (1992).
30. D. G. Hicks, T. R. Boehly, P. M. Celliers, J. H. Eggert, S. J. Moon, D. D. Meyerhofer, and G. W. Collins, *Phys. Rev. B* **79**, 014112 (2009).

Refractive Index of Lithium Fluoride Ramp Compressed to 800 GPa

Introduction

The transition of an insulator to a metal (metallization) at high compression is generally the result of pressure-induced closure of the band gap.^{1–4} Lithium fluoride's (LiF's) large-band-gap and ionic crystalline structure produces its uniquely high ultraviolet transmissivity. Two rare-gas solids, He and Ne, have anomalously high metallization pressures because of the predicted intershell band overlap, which is unique among monatomic materials.⁵ LiF holds a rare position among binary compounds in that Li⁺ and F⁻ are isoelectronic with He and Ne, respectively. Therefore, LiF is expected to have a uniquely high metallization pressure among large-band-gap solid insulators.

Under strong shock compression, the insulating/conducting transition is enhanced by the thermal promotion of electrons across the band gap.⁶ This is a result of high temperatures produced by high-pressure (>100-GPa*) shock waves. A variety of materials has been shocked into conductive matter that is highly reflective at the shock front.^{6–10} LiF has been previously observed to be transparent when shocked to ~115 GPa (Refs. 8 and 11) and becomes reflective for shock pressures >500 GPa (Ref. 6).

Recently, ramp compression has been used to compress materials to pressures above 100 GPa, while keeping the temperature low compared to that of a shock wave.¹² This work shows that LiF remains transparent when ramp compressed to 800 GPa—the highest pressure under which a transparent insulator has ever been observed. We use a new technique to measure its refractive index at pressures of 30 to 800 GPa. Early dynamic-compression experiments have shown the refractive index of various insulators to increase linearly with density at low pressure (~100 GPa). The results presented here indicate that the linearity of the LiF refractive index increase over a larger density range than previously shown. This is expected since the electronic polarizabilities of large-band-gap insulators typically increase with compression. The results presented here are the highest-pressure refractive-index measurements to date.

Ramp-compressed LiF remains transparent at higher pressures than in shock compression because thermal excitation is insufficient to produce conduction electrons. As a result, at these high compressions we expect that only the effects of density are important and use this to infer the pressure-induced band-gap closure of LiF using a single-oscillator model.¹³ Extrapolation of those results, although crude, indicates that ramp-compressed LiF may remain transparent to greater than 4000 GPa, well above the Goldhammer–Herzfeld criterion for metallization (~2800 GPa) (Refs. 14–16). LiF will therefore continue to have technical utility as a diagnostic window for experiments at extreme pressures, and the predicted band-gap closure provides important estimates for band-structure calculations.

In the present work, the refractive index of LiF was measured using ramp compression to 800 GPa. Diamond pistons were ramp compressed using the OMEGA laser.¹⁷ Diamond targets consisted of two sections: a free surface and a LiF window mounted on half of the rear surface. VISAR measurements were made at both sections to determine the refractive index. The subsequent sections discuss the relevant theory regarding the measurement technique, followed by a discussion of the experimental method and the experimental results. In the final section, an effective-oscillator model is used to interpret the results, providing an estimation of the band-gap closure.

Theory

In many high-pressure experiments, the motion of a reflecting interface behind an optical window is detected by measuring Doppler shifts with a velocity interferometry system for any reflector (VISAR).¹⁸ The reflected probe beam passes through the compression wave in the window, so the observed Doppler shift depends on the refractive index of the compressed window material. LiF is frequently used as an optical window because its transparency at high pressure allows one to make *in-situ* measurements of samples confined by that window.^{8,11} Hayes¹⁹ showed that for unsteady compression waves in windows, the *true* (U_t) and *apparent* (U_a) interface velocities (viewed through the compressed window) are directly related to the density-dependent refractive index of the window as

*100 GPa = 1 Mbar

$$\left. \frac{dU_a}{dU_t} \right|_{U_t} = \left(n - \rho \frac{dn}{d\rho} \right) \bigg|_{U_t} = f(\rho), \quad (1)$$

where the density (ρ) and refractive index (n) are evaluated as functions of U_t . One can show that this gives $n(\rho)$ explicitly as

$$n(\rho) = \rho \left[\frac{n_0}{\rho_0} - \int_{\rho_0}^{\rho} \frac{f(\rho')}{\rho'^2} d\rho' \right]. \quad (2)$$

In this work, $U_a(U_t)$ was measured using diamond as an impedance-matching standard and the refractive index as a function of density was determined by solving Eq. (2).

Experimental Method

The targets consisted of a planar diamond piston with two sections: half a free surface and an LiF window attached to the second half [see inset of Fig. 126.9(a)]. Planar compression waves, driven by direct laser ablation, produced identical compression waves across the two sections (bare and LiF) of the piston. The free-surface (bare diamond) velocity (U_{fs}) and the *apparent* interface (diamond–LiF) velocity (U_a) were measured simultaneously using VISAR.¹⁸ The response of the free surface was used to infer the *true* velocity of the piston/window interface.

The method of characteristics²⁰ was used to determine the drive-pressure history applied to the target by propagating U_{fs} backward to the loading surface. The free-surface wave profile, shown in the inset of Fig. 126.9(a), displays a distinct plateau at 2 $\mu\text{m}/\text{ns}$ caused by the drop from the longitudinal to the bulk sound speed as the elastic limit of diamond was exceeded. In this experiment, as in previous experiments,¹² the plateau showed a very constant velocity and the elastic limit was treated as a straightforward drop in the sound speed. Using that assumption, the calculated drive pressure was determined and then forward propagated to the diamond/LiF boundary, where pressures were impedance matched, thereby determining U_t . The diamond-ramp wave response measured by Bradley *et al.*,¹² which includes diamond strength, and the *SESAME* Table 7271 (Ref. 21) for LiF were used. The LiF *SESAME* Table 7271 accounts for hydrostatic deformations while neglecting plastic deformations. The inclusion of a Steinberg–Guinan^{22,23} strength model in the LiF equation of state (EOS) influenced the calculated interface pressure by $\ll 1\%$ prior to peak compression. As Ao *et al.*²² have shown, plastic effects in the interface velocity are of consequence only after peak compression. Analysis is terminated when interface yielding or “pullback” is observed, corresponding to ~ 5.5 ns for the inset of Fig. 126.9(b). LiF strength effects were neglected since the error contribution was significantly less than other sources.

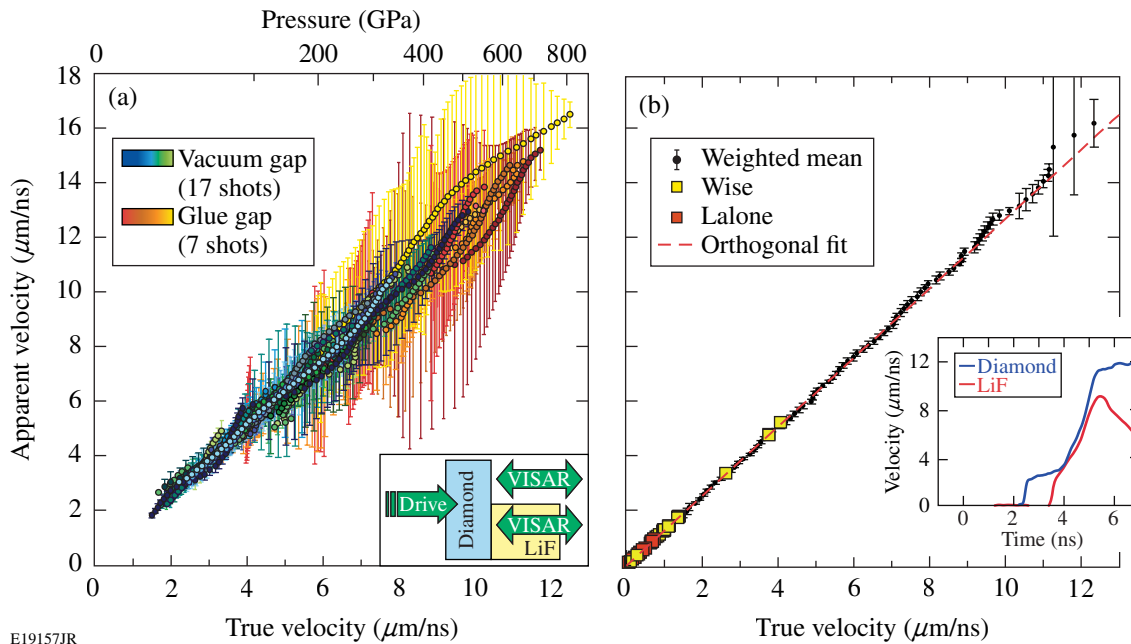


Figure 126.9

(a) *Apparent* and *true* velocity measurements for all experiments. Vacuum-gap and glue-gap experiments are distinguished by their corresponding colors. Inset shows the target diagram. (b) Weighted average of all shots. Orthogonal regression and previous shock data are included.^{8,11} Inset shows the VISAR measurements from a single experiment.

The experiments were performed on the OMEGA Laser System.¹⁷ The ablation pressure was controlled by temporal shaping the drive laser pulse to produce compressions in LiF from 30 to 800 GPa. These drive pulses compressed the targets without creating shock waves in either the chemical-vapor-deposition (CVD) diamond pusher or LiF samples over the duration of the experiment.

Laser intensity scaled as $\sim t^3$ for pulse-shape durations of 4 to 7 ns. The diamond thickness for those experiments was 46 μm ($\pm 1 \mu\text{m}$) and 100 μm ($\pm 3 \mu\text{m}$), respectively. A 500- μm -thick, high-purity LiF window was mounted over half of the rear of these diamond targets oriented with the $\langle 100 \rangle$ axis along the pressure-loading direction. Samples were glued at the edges such that the compressed diamond released directly into the LiF where there was no glue. A 1000- \AA titanium coating was applied to the diamond/LiF interface to increase the reflectivity for interferometer measurements. Three targets were constructed with gold layers (3 to 5 μm thick) placed 10 to 15 μm from the ablation surface to act as an x-ray shield to ensure there was no effect from high-energy x rays passing through the target. No difference was observed in the results from targets with and without these shields.

Experimental Result

1. Wave Profile Analysis

A total of 17 shots was performed to determine the *true* and *apparent* velocities as described above. Each of the 17 continuous measurements is shown as an ensemble of like-colored points in Fig. 126.9(a). The measured *apparent* velocities were observed to monotonically increase with pressure with no observed discontinuities, indicating a single phase of LiF existed to 800 GPa. This is consistent with recent *ab-initio* calculations performed by Smirnov.²⁴ The pressures corresponding to these velocities were determined from the LiF *SESAME* EOS²¹ as shown on the top axis. In those experiments, a weak shock was initiated in the LiF window; this was treated as an initial characteristic whose parameters were determined from impedance matching with the Hugoniot. The effect of shock formation in the LiF window is examined in **LASNEX Simulations** (p. 63).

Seven additional targets employed $\sim 2 \mu\text{m}$ of glue to fill the gap between the diamond and the LiF. At low pressures, the compressibility of the glue (and reverberations within it) caused the data to deviate from the targets with no glue between the LiF window and diamond. Once the glue “rang up” to higher pressure, the data followed the trend of targets with no glue-filled gap. Simulations indicated that after the glue rang up, corrections for the presence of $\sim 2\text{-}\mu\text{m}$ gaps caused a shift of the

true particle-velocity profiles after gap closure by ~ 3 ps, much less than the timing accuracy of these experiments.

The dominant errors in these calculations resulted from the precision of fringe-shift measurements (2.5% of a fringe) and uncertainty in the diamond isentrope cited by Bradley *et al.*¹² Measurements published by Hicks *et al.*,⁶ which were later re-examined by Celliers *et al.*,²⁵ are the only high-pressure measurements for LiF above 500 GPa published to date. Comparison of measurements made by Hicks *et al.*⁶ at ~ 1400 GPa with the *SESAME* Table 7271 indicates an $\sim 7\%$ error in pressure; therefore, a 10% error in pressure is assumed for the LiF isentrope.²² The errors in the timing correlation between U_a and U_t was of the order of 47 ps and 93 ps for cameras 1 and 2, respectively,¹⁸ corresponding to uncertainties added in quadrature of the etalon delay (37 ps and 78 ps) and nonuniformity in the drive planarity (5 pixels at sweep rates of 6 ps/pixel and 10 ps/pixel). Systematic uncertainties are attributed to camera shear (6 and 10 ps), gap correction ~ 1 ps (33% of the calculated temporal shift), and the neglect of LiF material strength ($\ll 1\%$ change in peak interface pressure). Systematic uncertainties are estimated to be 5% of the total uncertainty and therefore neglected. Random errors were propagated through the method of characteristics using a Monte Carlo procedure that propagates uncertainties randomly chosen from a normal distribution.²⁶

Steep gradients in the measured velocity profiles account for the large errors observed for single shots in Fig. 126.9(a). These were reduced by using a ramp compression that rose more gradually, albeit to lower pressures. Streaked optical pyrometer²⁷ measurements of LiF were dominated by thermal emission from the diamond anvil observed through the LiF. Comparison of the self-emission from the diamond-free surface and the diamond/LiF interface suggests that the LiF window temperature remained below 1000 K for all cases.

Figure 126.9(b) shows the weighted mean (black points) of the data from Fig. 126.9(a) using the associated errors discussed above. The large errors between 700 to 800 GPa occur because only a single experiment reached those pressures. The dashed line is the linear portion of a fit performed to that weighted mean (see below). Shock-wave data taken from Wise and Chhabildas⁸ and LaLone *et al.*¹¹ are shown up to 115 GPa as yellow and red squares, respectively.

A second-order orthogonal polynomial regression^{25,26} was to fit the U_t [km/s] and U_a [km/s] particle velocities: $U_a(U_t) = a_0 + a_1(U_t - \beta) + a_2(U_t - \gamma_1)(U_t - \gamma_2)$, where $\beta = 2.41$ km/s, $\gamma_1 = 0.713$ km/s, and $\gamma_2 = 9.53$ km/s were determined by the distribu-

tion of U_1 in the data being fit. Since these parameters depend on the independent variable, errors were not assigned. Coefficients (a_0 , a_1 , and a_2) were determined from a weighted χ^2 minimization. In the orthogonal fit, the value of each coefficient is independent of higher-order terms, diagonalizing the co-variance. U_1 is considered the independent variable and U_a the dependent one with a standard deviation $\sigma_{U_a}^2 = (\delta U_a)^2 + (1.28 \delta U_1)^2$. δU_a is the error associated with the measured interface velocity and δU_1 is the error determined by Monte Carlo simulations, which is weighted by 1.28 to account for the estimated slope. Errors determined in the orthogonal fitting coefficients underestimate deviations observed within the data. This was observed when shots were removed at random and orthogonal fitting was performed. Coefficient errors were determined by standard deviations calculated from 100 discrete shot groupings of the 24 experiments: $a_0 = 3.0634$ [km/s], $a_1 = 1.2751 \pm 0.0082$, and $a_2 = 0.0008 \pm 0.0015$ [s/km]. Errors were not assigned to a_0 since it represents the centroid of the data. The slope (a_1) dominates the determination of the refractive index [Eq. (1)], and contributions from the curvature (a_2) are assumed negligible because of their relative size and the bounding of zero.

Equation (2) was used to calculate $n(\rho)$ (Fig. 126.10) using the weighted mean (black line). The refractive index and density under standard conditions (1.3935 and 2.6380 g/cc) were used as the boundary. The refractive index determined from the orthogonal fitting parameters is

$$n = 1.275(\pm 0.008) + 0.045(\pm 0.003)\rho, \quad (3)$$

where the second-order term (a_2) has been neglected. The results obtained are in agreement with high-precision shock results up to 20 GPa (Ref. 11)

$$n = 1.277(\pm 0.002) + 0.0443(\pm 0.008)\rho, \quad (4)$$

and diamond-anvil experiments²⁸

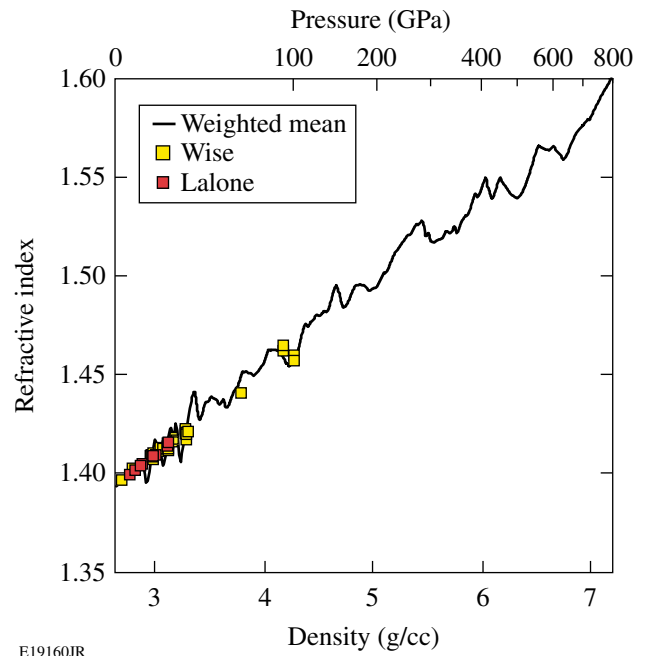
$$n = 1.25(\pm 0.03) + 0.05(\pm 0.01)\rho. \quad (5)$$

The effective polarizability (α) of LiF is calculated using the Clausius–Mossotti relation

$$\frac{1}{\rho} \frac{\varepsilon - 1}{\varepsilon + 2} = \frac{4\pi N_A}{3} \alpha, \quad (6)$$

where ε is the dielectric function and N_A is Avogadro's number. For these experiments, the LiF absorption was negligible, indicating that the imaginary part of the refractive index was small or $\varepsilon \approx n^2$. Using Eq. (6) and this approximation, the

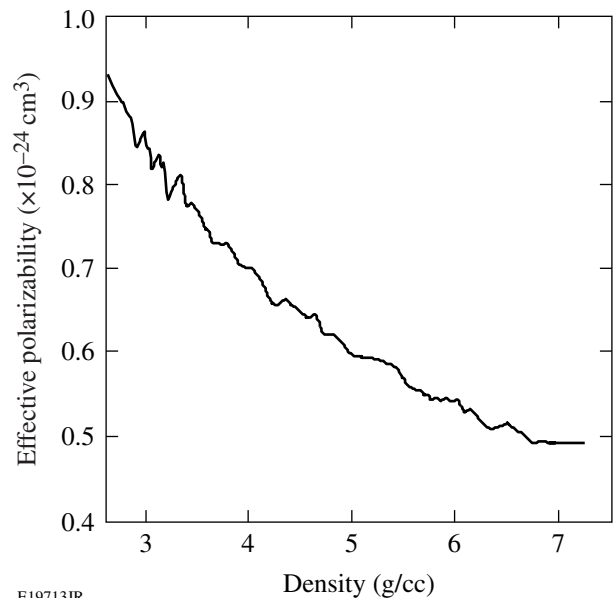
effective polarizability is calculated and plotted as a function of compression in Fig. 126.11. The effective polarizability is observed to decrease with increasing pressure.



E19160JR

Figure 126.10

Refractive index as a function of density determined using the weighted average and linear orthogonal fit. Previous data shock is included.^{8,11}



E19713JR

Figure 126.11

The effective polarizability determined from the Lorentz–Lorenz relation plotted as a function of density.

2. LASNEX Simulations

LASNEX²⁹ simulations were performed to address concerns regarding shock formation in the LiF window and LiF material strength. The arrival of the diamond elastic limit (EL) in the LiF window generates a weak shock. Compression waves in the LiF window may reflect off the shock front, and the arrival of those waves at the LiF would violate the conditions required in the derivation of Eq. (1) (Ref. 19). Since the method of characteristics does not account for the potential of shock formation, LASNEX simulations were performed to verify the characteristic calculations. LASNEX calculations used a diamond EOS with a Steinberg–Guinan–strength model to recover the EL²³ and LiF *SESAME* Table 7271 (Ref. 21). The pressure drive was applied 10 μm inside the front surface to account for the material ablated by the laser driver. This applied pressure is estimated to best match the measured diamond free-surface velocity.

LASNEX simulations were performed on shot 56113, and the results are shown in Figs. 126.12(a) and 126.12(b). Figure 126.12(a) contains a plot of the diamond free-surface velocity measured using VISAR (blue) and the estimated velocity determined from LASNEX (black) for an approximate applied laser intensity. Figure 126.12(a) shows that the LASNEX free-surface velocity correlates well with the measured free-surface velocity. The applied pressure drive that determines the free-surface velocity is then used to simulate the *true* interface velocity. The noticeable discrepancies between the LASNEX simulation and measure free-surface velocity at 3.9 ns and 4.2 ns is due to the limitations of Steinberg–Guinan–strength model. That model predicts a higher EL than observed in this study generating the noticeable two-wave structure. As observed by McWilliams *et al.* the diamond EL varies and these variations are the cause of the observed discrepancy.³⁰

Figure 126.12(b) compares interface velocities calculated using both methods. The LASNEX-predicted *true* interface velocity (black) and the *true* interface velocity calculated using the method of characteristics (red) infer nearly identical velocities prior to peak compression. The excellent agreement indicates that either (a) shock formation does not occur in the LiF window or (b) the effects of shock formation under these conditions do not significantly perturb the interface velocity prior to peak compression. This indicates that the requirements on Eq. (1) are met and Eq. (1) remains valid for these experiments. Furthermore, simulations performed with and without a Steinberg–Guinan–strength model differ $\ll 1\%$ in pressure.

Discussion

The temperatures achieved in this study are significantly lower than temperatures for identical pressures along the principal Hugoniot. *SESAME* Table 7271 predicts the principal isentrope temperature at 400 GPa and 800 GPa to be ~ 700 k and ~ 800 k, respectively. The temperature along the principal Hugoniot for those pressures are significantly higher (12,500 k and 31,500 k). Molecular dynamic simulations³¹ suggest that the Hugoniot approaches the melt line at ~ 150 GPa at ~ 3500 k. Quantum molecular dynamics simulations predict as LiF melts, it transitions from a large gap insulator into a reflective material and during this transition develops a nonlinear refractive index.³² The low temperatures achieved in this study prevent LiF from approaching melt, inhibiting the development of a nonlinear refractive index.

An effective-oscillator model¹³ was used to interpret the observed linear dependence of refractive index on density. The effective-oscillator model describes optical properties as a weighted average over the visible spectrum. It is a simplistic dielectric model that predicts the magnitude and dispersion of

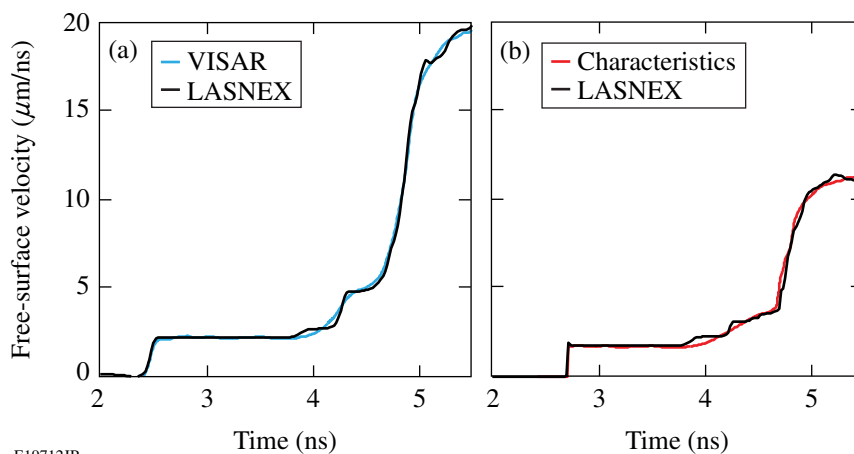


Figure 126.12

Comparison of hydrocode simulations and the method of characteristics for shot 56113. (a) LASNEX ablation pressure is determined by matching the LASNEX free-surface velocity (black) with VISAR measurement (blue). (b) The ablation pressure calculated using LASNEX is then used to determine the *true* interface velocity. Comparison of the LASNEX results (black) and the method of characteristics (red) is shown.

E19712JR

ionic and covalent substances. The refractive index is defined by two “average” parameters: the dispersion energy (E_d) and single-oscillator energy (E_0). E_0 is empirically related¹³ to the lowest direct optical transition E_t defined as the excitonic or band gap. The single-oscillator energy represents an average energy gap where the direct and indirect gaps may be smaller or exceed that energy.³³

Wemple and DiDomenico¹³ have shown that frequency-dependent refractive index for covalent and ionic materials can be fit to

$$n^2 - 1 = \frac{E_d E_0}{E_0^2 - \hbar^2 \omega^2}, \quad (7)$$

where E_d is the dispersion energy, E_0 is the single-oscillator energy, and $\hbar\omega$ is the photon energy. In a survey of over 100 solid and liquid insulators at ambient conditions, this model fits the frequency-dependent refractive index well.¹³

This model was applied to the pressure-induced closure of the H_2 band gap over a large density range^{34–36} and successfully predicted the emergence of excitonic absorption in the visible spectrum.⁴ Those studies show the H_2 exciton shifts from 14.5 eV to 2 eV with a slightly sublinear dependence on density over nearly 15-fold compression. The effective-oscillator model has been applied to H_2O ice, demonstrating a linear reduction in the band gap over 2.3-fold compression.³³ In that study, the dispersion was measured from 569 to 741 nm at pressures ranging from 0 to 120 GPa. At discrete pressures, the effective-oscillator parameters (E_d and E_0) were determined. Zha *et al.*³³ found that E_d was independent of density (remained constant) and that the effective gap closed monotonically with density. Wemple and DiDomenico¹³ have shown that the ratio of the band-gap energy to the lowest direct optical transition E_0/E_t is constant for constant dispersion energy (E_d).

The effective-oscillator model was applied to the data presented here, where the ambient values of E_d and E_0 were determined by fitting the refractive index to measured values in the range of 332 nm $< \lambda <$ 732 nm, i.e., the wavelength region near the probe laser.¹⁶ Fixing E_d to its ambient value, E_0 is calculated as a function of density using Eq. (7), as shown in Fig. 126.13. For the alkali halides of NaCl structure, the average ratio of single-oscillator energy to direct band gap is $E_0/E_t = 1.36$. This effective band gap begins at the intense exciton observed at ambient pressure³⁷ and then decreases with rising pressure.

Extrapolation of these results (a crude approximation) indicates that the band gap may close above >4000 GPa. This suggests that LiF will remain transparent well above the Goldhammer–Hertzfeld (G–H) criterion (~ 2800 GPa) (Refs. 14–16). This difference is consistent with the observed behavior of He and Ne, which exhibited abnormally high metallization at pressures $10\times$ greater than predicted by the G–H criterion.^{5,38}

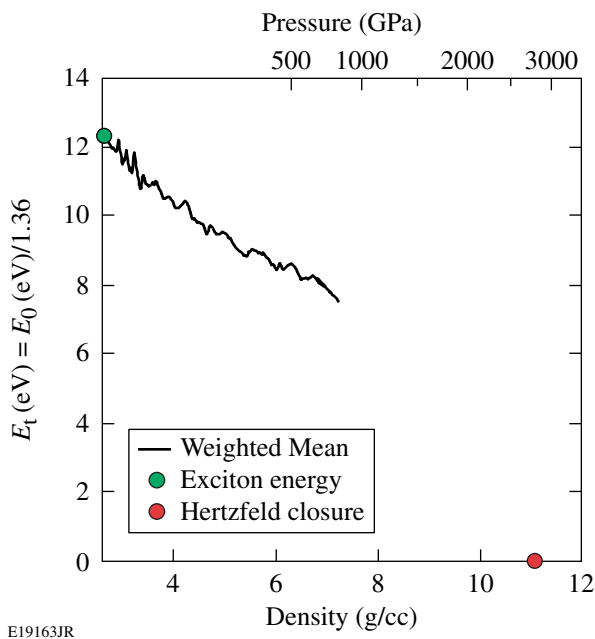


Figure 126.13 Density dependence of the single-oscillator model (E_t). Extrapolation suggests that LiF may remain transparent to pressure above 4000 GPa.

Conclusion

Direct laser ablation was used to ramp compress LiF from 30 to 800 GPa. LiF was observed to remain transparent over this pressure range; this is the highest-pressure insulator ever observed. The apparent and true particle velocities were measured over this range and were used to calculate the refractive index of compressed LiF, which was found to depend linearly on density. These are the highest pressure measurements of refractive index to date and are used to infer the pressure-induced band-gap closure of compressed LiF using an effective-oscillator model. These measurements provide a VISAR correction factor up to 800 GPa. Extrapolation of these results suggests that LiF remains transparent to pressures >4000 GPa as long as the temperature remains sufficiently low. If true, LiF will prove to be a valuable window for extremely high pressure ramp-compression experiments.

ACKNOWLEDGMENT

This work was supported by the U.S. Department of Energy Office of Inertial Confinement Fusion under Cooperative Agreement No. DE-FC52-08NA28302, the University of Rochester, and the New York State Energy Research and Development Authority.

REFERENCES

1. R. Reichlin *et al.*, Phys. Rev. Lett. **56**, 2858 (1986).
2. K. A. Goettel *et al.*, Phys. Rev. Lett. **62**, 665 (1989).
3. R. Reichlin *et al.*, Phys. Rev. Lett. **62**, 669 (1989).
4. P. Loubeyre, F. Occelli, and R. LeToullec, Nature **416**, 613 (2002).
5. J. C. Boettger, Phys. Rev. B **33**, 6788 (1986).
6. D. G. Hicks *et al.*, Phys. Rev. Lett. **91**, 035502 (2003).
7. S. B. Korner, Sov. Phys.-Usp. **11**, 229 (1968).
8. J. L. Wise and L. C. Chhabildas, Sandia National Laboratory, Albuquerque, NM, Report SAND-85-0310C, NTIS Order No. DE85015505 (1985).
9. D. K. Bradley *et al.*, Phys. Rev. Lett. **93**, 195506 (2004).
10. J. Eggert, S. Brygoo, P. Loubeyre, R. S. McWilliams, P. M. Celliers, D. G. Hicks, T. R. Boehly, R. Jeanloz, and G. W. Collins, Phys. Rev. Lett. **100**, 124503 (2008).
11. B. M. LaLone *et al.*, J. Appl. Phys. **103**, 093505 (2008).
12. D. K. Bradley *et al.*, Phys. Rev. Lett. **102**, 075503 (2009).
13. S. H. Wemple and M. DiDomenico, Jr., Phys. Rev. B **3**, 1338 (1971).
14. A. Goldhammer, in *Monatshefte für Mathematik* (Teubner, Leipzig, Berlin, 1913), Vol. 27.
15. K. F. Herzfeld, Phys. Rev. **29**, 701 (1927).
16. E. M. Bass, ed. *Handbook of Optics*, 2nd ed., Volume II: Devices, Measurements, and Properties (McGraw-Hill, New York, 1994).
17. T. R. Boehly, D. L. Brown, R. S. Craxton, R. L. Keck, J. P. Knauer, J. H. Kelly, T. J. Kessler, S. A. Kumpan, S. J. Loucks, S. A. Letzring, F. J. Marshall, R. L. McCrory, S. F. B. Morse, W. Seka, J. M. Soures, and C. P. Verdon, Opt. Commun. **133**, 495 (1997).
18. L. M. Barker and R. E. Hollenbach, J. Appl. Phys. **43**, 4669 (1972).
19. D. Hayes, J. Appl. Phys. **89**, 6484 (2001).
20. J. R. Maw, AIP Conf. Proc. **706**, 1217 (2004).
21. S. Crockett and S. Rudin, Los Alamos National Laboratory, Los Alamos, NM, LA-UR-06-8401 (2006).
22. T. Ao *et al.*, J. Appl. Phys. **106**, 103507 (2009).
23. D. J. Steinberg, S. G. Cochran, and M. W. Guinan, J. Appl. Phys. **51**, 1498 (1980).
24. A. Smirnov, Phys. Rev. B **83**, 014109 (2011).
25. P. M. Celliers *et al.*, J. Appl. Phys. **98**, 113529 (2005).
26. P. R. Bevington and D. K. Robinson, *Data Reduction and Error Analysis for the Physical Sciences*, 3rd ed. (McGraw-Hill, Boston, 2003).
27. J. E. Miller, T. R. Boehly, A. Melchior, D. D. Meyerhofer, P. M. Celliers, J. H. Eggert, D. G. Hicks, C. M. Sorce, J. A. Oertel, and P. M. Emmel, Rev. Sci. Instrum. **78**, 034903 (2007).
28. N. M. Balzaretti and J. A. H. Da Jornada, J. Phys. Chem. Solids **57**, 179 (1996).
29. G. B. Zimmerman and W. L. Kruer, Comments Plasma Phys. Control. Fusion **2**, 51 (1975).
30. R. S. McWilliams, J. H. Eggert, D. G. Hicks, D. K. Bradley, P. M. Celliers, D. K. Spaulding, T. R. Boehly, G. W. Collins, and R. Jeanloz, Phys. Rev. B **81**, 014111 (2010).
31. R. Boehler, M. Ross, and D. B. Boercker, Phys. Rev. Lett. **78**, 4589 (1997).
32. J. Clérouin *et al.*, Phys. Rev. B **72**, 155122 (2005).
33. C.-S. Zha *et al.*, J. Chem. Phys. **126**, 074506 (2007).
34. J. van Straaten and I. F. Silvera, Phys. Rev. B **37**, 6478 (1988).
35. A. García *et al.*, Phys. Rev. B **45**, 9709 (1992).
36. R. J. Hemley, M. Hanfland, and H. K. Mao, Nature **350**, 488 (1991).
37. D. J. Mickish, A. B. Kunz, and T. C. Collins, Phys. Rev. B **9**, 4461 (1974).
38. S. A. Kairallah and B. Militzer, Phys. Rev. Lett. **101**, 106407 (2008).

Hot-Electron Heating Caused by Two-Plasmon-Decay Instability

Introduction

High-energy electrons are detrimental to laser fusion because they can preheat the fuel, preventing the high compression necessary for central hot-spot ignition and high gain.¹ The direct-drive approach is particularly vulnerable as a result of the long scale length of plasma that exists at the quarter-critical density of the target, although it can also occur in indirect-drive geometry.²

Direct-drive-implosion experiments on OMEGA have observed hard x rays (a signature of hot electrons) that are coincident with the emission of half-integer harmonics and the predicted two-plasmon-decay (TPD) threshold.³ Four-channel x-ray spectroscopy ranging in energies from 20 to 500 keV indicates hot-electron temperatures of $T_{\text{hot}} \lesssim 100$ keV for irradiation intensities of $I_0 \sim 10^{15}$ W/cm² at $\lambda_0 = 351$ nm (Ref. 4). Since electrons in excess of 100 keV are inferred experimentally via the hard x rays that they produce, it is apparent that the possibility of preheating exists. This will lead to an increased fuel adiabat and diminished fuel compressibility. Estimates of target preheat based on measured x rays are difficult, but likely fall in the range of 40 to 50 J, where the impact on target performance might be measurable on OMEGA (Delettrez *et al.* estimate a 40% reduction in areal density for a worst-case scenario on the basis of one-dimensional hydrodynamic calculations⁵).

Definitive evidence of preheat-impaired performance [e.g., in reduced areal density (ρR)] on OMEGA is currently lacking,^{6,7} which complicates any extrapolation of preheat to ignition-scale designs. For example, in implosion experiments, close to 80% of maximum predicted areal density above 200 mg/cm² has been achieved using 10- μ m-thick deuterated plastic (CD) ablaters.⁸ The TPD instability is only weakly excited in these targets. It can be more strongly excited by using thinner shells since the TPD threshold is more easily attained in hydrogenic plasma. While a significant degradation of ρR is observed for thinner CD ablaters, it is not currently possible to rule out other competing mechanisms such as shock mistiming, hydrodynamic instability, radiation preheat, and preheat by nonlocal thermal electrons.

The need for a physical model of target preheat clearly exists. The self-consistent modeling, however, of hot-electron generation and the resulting preheating of the target is a very challenging problem. The purpose of this article is to present a model that represents an attempt in this direction. It includes aspects of the experimental conditions that are thought to be important. Namely, it assumes that all preheat is associated with TPD instability and the plasma inhomogeneities (density gradient) play an important role. The model contains nonlinearities that have been shown by detailed particle-in-cell calculations to play a dominant role in saturation.^{9,10} The possibility of multiple acceleration stages for hot electrons as they periodically pass through the quarter-critical surface is also investigated. It takes the trajectory of the heated electrons that lies outside of the simulation boundaries into account. It is shown that, for the parameters of current OMEGA direct-drive cryogenic implosions, recirculation (or reheating) of electrons is an important effect.

While several simplifications are made, we attempt to show how, in future work, these simplifications may be systematically relaxed. The most important of these is the development of a self-consistent quasilinear model for the evolution of the electron distribution function¹¹ that would replace the current test-particle treatment.

The sections that follow describe the model for electron heating, with subsections describing the extended Zakharov model for the saturated electric field spectrum and outlining the test-particle method; present the results of electron-heating calculations; and, finally, present a summary and conclusions.

Description of a Model for Hot-Electron Production

Based on experimental observations, there are reasons to believe that TPD is the sole instability active in producing hot electrons in current OMEGA experiments. Half-integer harmonic signatures of TPD are strongly correlated with hard x-ray production, with x-ray energies of the order of $E_{\text{x ray}} \sim 100$ keV (Refs. 3 and 4). The onset of TPD signatures is also well predicted by the simple linear threshold for the absolute TPD

instability of a plane electromagnetic wave in a density gradient when the intensity of the plane wave is equated with the average overlapped-beam intensity on OMEGA. Thresholds for TPD in a linear gradient have been computed by a number of authors.^{12–21} The “above-threshold parameter” $\eta = I_{14} L_{\mu\text{m}} / (320 T_{\text{keV}})$, which is based on the expression for absolute instability computed by Simon *et al.*,¹³ $(v_{\text{osc}}/v_e)^2 k_0 L > 4.134$ (i.e., the large β limit), has proven itself to be a very useful empirical tool for interpreting OMEGA experiments.^{3,5,8} While the onset is well predicted by the η parameter, which signals absolute instability, the measured spectrum of plasma waves is generally not consistent with the absolutely unstable eigenmode.³ Above threshold, the absolutely unstable wave corresponds to a forward-going plasmon of wave number close to k_0 , where k_0 is the laser vacuum wave number, and a plasmon with small perpendicular wave number given by

$$k_{\perp}/k_0 = 0.02 I_{14}^{1/4} (\lambda_0/0.351 \mu\text{m}) \times (T_e/2 \text{ keV})^{-1} (L/150 \mu\text{m})^{-1/2},$$

while experimentally, most Langmuir wave (LW) intensity is found to be located close to the Landau cutoff ($k \sim 0.25 k_{\text{De}}$, where k_{De} is the Debye wave number).³ This is not too surprising because convective growth can become important at similar intensities and can dominate the nonlinear state^{9,22} because it is not as easily saturated as the absolute mode (see **Zakharov Model for the Saturated LW Spectrum**, below).

Raman backscattering is neglected in the model because of the absence of an experimentally observed Raman backscattering signature. This is consistent with linear gain estimates: Raman scattering is expected to be convectively unstable below quarter-critical, with the Rosenbluth gain²³ $A_{\text{Ros}} = \pi \gamma_0^2 / |V_1 V_2 \kappa'|$ being negligible for the relevant experimental parameters

$$A_{\text{Ros}} \sim 0.04 I_{14} (1 - n_e/n_c)^{-1/2} (L_{\mu\text{m}}/150 \mu\text{m}).$$

The envelope approximation, upon which the previous expression relies, is not valid near the quarter-critical density. Drake *et al.* have demonstrated the potential for absolute instability of stimulated Raman scattering (SRS) near the quarter-critical density²⁴ with the threshold condition

$$v_{\text{osc}}/c > (1/2)(k_0 L)^{-2/3}.$$

The ratio of the TPD threshold to the above expression for absolute SRS is given approximately by

$$I_{\nabla}^{2\text{P}}/I_{\nabla}^{\text{R}} = 0.9 (T_{e,\text{keV}}/2 \text{ keV}) \times (0.351 \mu\text{m}/\lambda_0)(L/150 \mu\text{m})^{1/3}.$$

It appears that the effects of absolute Raman scattering near the quarter-critical density should be taken into account. The model currently omits this possibility (and achieves a worthwhile simplification by ignoring the equation for the envelope of the scattered transverse wave). This is based on the observations of the dominance of convective TPD over absolute TPD (see **Zakharov Model for the Saturated LW Spectrum**, below) and, by association, absolute Raman or high-frequency hybrid instability.^{18,19} The neglect of these terms also appears consistent with results reported for explicit particle-in-cell (PIC) calculations.⁹

The spectrum of LW's driven by TPD instability is assumed to be saturated by nonlinearities that are contained within the extended Zakharov approximation.^{25,26} Recent comparisons between the Zakharov model and reduced PIC calculations of TPD in homogeneous plasma indicate this to be a reasonable approximation.¹⁰ The model takes into account the density gradients and flow velocities at quarter-critical that are predicted to occur experimentally on the basis of 1-D radiation–hydrodynamic calculations using the *LILAC* code.²⁷

Electron heating in response to this spectrum of electrostatic waves is computed in a test-particle approximation, i.e., the electron distribution is heated by the LW's, but the modified electron-distribution function does not act back on the LW's, i.e., there is no kinetic modification of the LW dispersion relation. This is done in order to make contact with experimental observations, as well as to investigate the effects of recirculating electron trajectories, which have for a long time been thought to be important.^{11,28}

The test-particle approach to electron heating also allows for a systematic investigation of the validity of a self-consistent quasilinear model for TPD¹¹ along the lines of Sanbonmatsu *et al.*^{29,30} by explicitly computing the diffusion of electron velocities, $\langle (\Delta \vec{v})^2 / \Delta t \rangle$ (Refs. 31–33). This will be the subject of a future publication.

1. Zakharov Model for the Saturated LW Spectrum

The LW fields near the quarter-critical surface are modeled in the extended Zakharov approximation in two spatial dimensions taking into account a prescribed density gradient, as has been described previously,^{25,26} and now extended here to include a prescribed flow velocity

$$\begin{aligned}
& \nabla \cdot [2i\omega_{p0}(\partial_t + \vec{v}_0 \cdot \nabla + \nu_e^\circ) \\
& + 3v_e^2 \nabla^2 - \omega_{p0}^2(\delta n + \delta N)]\vec{E} \\
& = (e/4m_e) \nabla \cdot [\nabla(\vec{E}_0 \cdot \vec{E}^*) - \vec{E}_0 \nabla \cdot \vec{E}^*] + S_E. \quad (1)
\end{aligned}$$

In the above equation, \vec{E} is the slowly varying complex envelope of the longitudinal electric field $\vec{E}_l = 1/2\vec{E}\exp(i\omega_{p0}t) + \text{c.c.}$ (i.e., the electric field is decomposed into longitudinal and transverse components $\vec{E} = \vec{E}_l + \vec{E}_t$). The quantity \vec{E}_0 is the slowly varying (in time) complex envelope of the transverse, electromagnetic (EM) field,

$$\vec{E}_t = \sum_{j=1}^{N_j} \vec{E}_{0,j} \exp[i\vec{k}_{0,j} \cdot \vec{x} - i(\omega_0 - 2\omega_{p0})t + i\phi_j],$$

which consists of N_j beams of amplitude $\vec{E}_{0,j}$ and of wave number $\vec{k}_{0,j}$ that differs only in direction ($|\vec{k}_{0,i}| = |\vec{k}_{0,j}|$) and phase ϕ_j . The reference electron-plasma frequency is

$$\omega_{p0} = (4\pi n_0 e^2 / m_e)^{1/2},$$

and $v_e = (T_e / m_e)^{1/2}$ is the electron thermal velocity. For the slow density variation, $\delta n + \delta N$ represents the departure from the reference density $n_0 = 0.23 n_c$, where $n_c = m_e \omega_0^2 / (4\pi e^2)$ is the laser critical density. The static, i.e., non-evolving, component of the electron density corresponds to a linearly increasing density profile,

$$N(x) \equiv n_0 + \delta N = [0.23 + 0.04(2x/l_x - 1)]n_c,$$

which varies from $0.19 n_c$ to $0.27 n_c$ over the simulation length l_x , where $x \in [0, l_x]$ and has a density scale length of $L_n^{-1} \equiv d[\log N(x)]/dx = (8/23)l_x^{-1}$. The value of L_n is assumed to be constant in time during the integration period of the Zakharov model. The evolving component $\delta n(\vec{x}, t)$, a real quantity, satisfies the second Zakharov equation

$$\begin{aligned}
& [(\partial_t + \vec{v}_0 \cdot \nabla)^2 + 2\nu_i^\circ (\partial_t + \vec{v}_0 \cdot \nabla) - c_s^2 \nabla^2] \delta n \\
& = \frac{\nabla^2}{16\pi m_i} \left[|\vec{E}|^2 + \frac{1}{4} \left| \sum_j \vec{E}_{0,j} \exp i(\vec{k}_{0,j} \cdot \vec{x} + \phi_j) \right|^2 \right] \\
& \quad + S_{\delta n}, \quad (2)
\end{aligned}$$

which takes into account the ponderomotive force of the light waves, each having the phase ϕ_j . The low-frequency (LF) fluctuations are also driven by the ponderomotive pressure of the LW's, which is quadratic in \vec{E} . The damping operators ν_e°

and ν_i° are local in k-space and contain the contribution of collisional and Landau-damping terms corresponding to a fixed Maxwellian ion- and electron-velocity distribution function of temperatures T_i and T_e , respectively. The terms S_E and $S_{\delta n}$ are noise terms that support a thermal level of LW and ion-acoustic-wave (IAW) fluctuations in the absence of other sources.²⁵

The numerical domain $\Omega = [0, l_x] \times [0, l_y]$ on which the extended Zakharov model is solved is typically arranged so that the linear electron-density profile spans the range $0.19 < n_e/n_c < 0.27$. This ensures that the electric field associated with the LW's vanishes on the longitudinal boundaries. The electrostatic waves are damped at low density (large $k_{\lambda D e}$) and reflected (turn) before encountering the boundary at the high-density side. Based on predicted scale lengths on OMEGA of $L_n \sim 150 \mu\text{m}$, this translates into a spatial dimension l_x of approximately $l_x \sim 50 \mu\text{m}$. The transverse dimensions are usually a few tens of microns. The transverse dimension should be as small as possible for computational efficiency, but no shorter than the correlation length for the LW fields. Typically, the transverse length l_y , where $y \in [0, l_y]$, is chosen to be $l_y \gtrsim 12.0 \mu\text{m}$.

a. Zakharov predictions for the saturated LW spectrum.

The nonlinear saturation of TPD based on the model presented in **Zakharov Model for Saturated LW Spectrum** (p. 67) is seen to involve a process of density-profile modification,^{25,34} the generation of ion-acoustic-wave turbulence as a result of the ponderomotive response to primary TPD LW's,^{9,25} LW cavitation and collapse, and Langmuir decay instability.²⁵ The development is quite similar to that observed in homogeneous reduced particle-in-cell calculations made recently by Vu *et al.*¹⁰ and is broadly consistent with earlier observations that saturation occurs as a result of ion-wave fluctuations³⁵ or profile steepening.^{34,36}

A series of two-dimensional calculations solving Eqs. (1) and (2) have been carried out with parameters motivated by conditions either currently or soon-to-be accessible on the OMEGA Laser System: the laser wavelength $\lambda_0 = 0.351 \mu\text{m}$, the electron temperature $T_e = 2.0 \text{ keV}$, the ion temperature $T_i = 1.0 \text{ keV}$, ion charge $Z = 3.5$ (effective charge state corresponding to CH plasma), IAW damping of $\nu_{i0} \equiv \nu_i/kc_s = 0.1$, and density-gradient scale lengths in the range $L_n = (100 \text{ to } 350) \mu\text{m}$. The simulation domain was chosen so as to include densities from $n_e = (0.19 \text{ to } 0.27) n_c$. In the case of $L_n = 150 \mu\text{m}$ (which we define as the ‘‘canonical’’ scale length on OMEGA), $l_x = 45.0 \mu\text{m}$, and $l_y = 12.0 \mu\text{m}$ (other cases were adjusted appropriately). The simulations were made with either a single-plane

electromagnetic (EM) wave ($N_j = 1$), normally incident along the direction of the density gradient ($\vec{k}_{0,1} \cdot \hat{e}_x/k_{0,1} = 1$), or with two overlapping plane waves ($N_j = 2$), each incident at an angle of $\theta_j = \cos^{-1}(\vec{k}_{0,j} \cdot \hat{e}_x/k_{0,j}) = \pm 0.23^\circ$ to the direction of the density gradient (the calculations with two crossed beams allow for the sharing of a common plasma wave¹⁰ that is thought to be an important experimental process on OMEGA.³⁷) The plane of simulation is chosen to be coincident with the plane of polarization, which also assumes that all N_j beams are similarly polarized. The laser intensities I_L (incoherent overlapped “intensity” $I_L \equiv c/(8\pi) \sum_{i=1}^{N_j} |\vec{E}_{0,i}|^2$ in the case of multiple beams) were varied in the range $I_L = (5 \times 10^{14} - 2 \times 10^{15}) \text{ W/cm}^2$. The combination of laser intensity and density scale length was chosen to put the absolute TPD instability in either the weakly unstable ($\eta \sim 1.5$) or moderately unstable regime ($\eta \sim 2$ to 3) with respect to the threshold criterion as defined by Simon *et al.*¹³ Although there are differences between the single-beam and crossed-beam calculations, which will be described in a separate publication, the generic results described below are illustrative of both cases.

The calculations develop from the initial onset of absolute instability, which corresponds very well with the calculations of Simon *et al.*¹³ with regard to both the threshold intensity and unstable wave number (eigenmode), toward a broad spectrum of plasmons as shown in Fig. 126.14(a). [The onset of absolute

instability and the resulting growth rate were determined accurately by removing the nonlinear coupling between the Eqs. (1) and (2). The threshold intensity was therefore observed to coincide with the Simon *et al.* prediction to within 10% for the normally incident single-beam case].

The absolutely growing mode eventually reaches a sufficient amplitude where nonlinearities become important. The time required for strong nonlinearity to become important for canonical OMEGA parameters based on an initial noise level of $\langle |E|^2 \rangle / (8\pi n_0 T_e) = 6 \times 10^{-6}$ and a laser intensity of $I_L = 10^{15} \text{ W/cm}^2$ was found to be $\sim 1.2 \text{ ps}$. Density-profile modification³⁴ was the saturating mechanism of the absolute modes in these calculations. This was determined by performing an estimate of the local steepening of the density gradient by taking a transverse (y direction) average of the density $\tilde{N}(x) \equiv \langle N(x) + \delta n(x, y) \rangle_y$ (as shown in Fig. 126.15) and estimating the modified gradient scale length in the neighborhood of the quarter-critical density $L_{\mu m}$. The observed scale length, when substituted into the threshold expression, was found to lead to marginal stability $\eta = I_{14} \tilde{L}_{\mu m} / (230 T_{\text{keV}}) \sim 1$. This situation was found to hold for all calculations that were performed. The collapse in growth of the initially unstable eigenmode is followed by an expanding region of large LW excitation at lower densities (corresponding to larger k_\perp LW’s in the single-beam case). This is seen in the Fourier spectrum

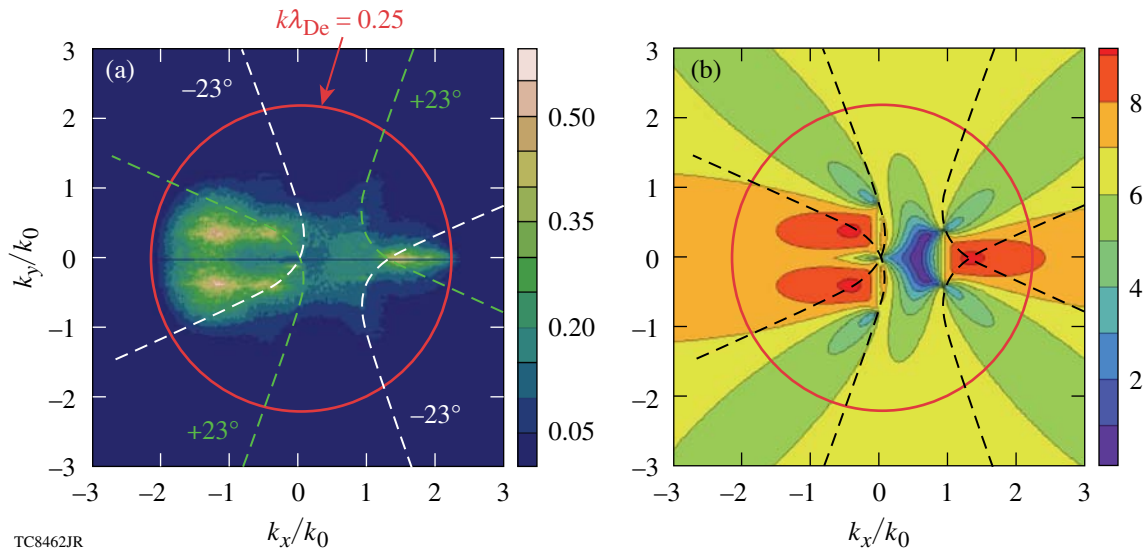
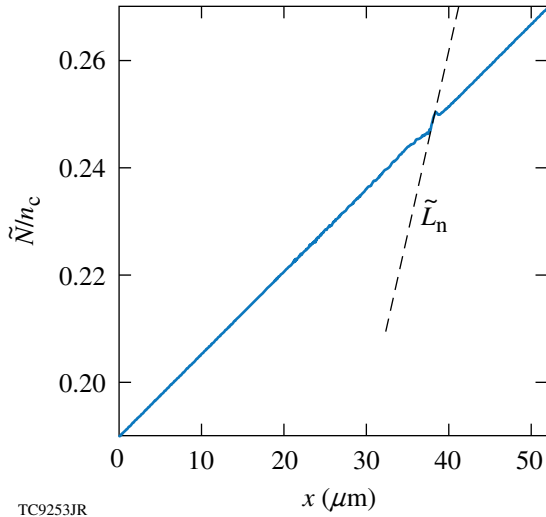


Figure 126.14

(a) The saturated Langmuir wave spectrum in Fourier space $|\vec{E}_k|^2$ corresponding to a crossed-beam irradiation geometry with an overlapped intensity of $I_L = 1 \times 10^{15} \text{ W/cm}^2$ (canonical OMEGA parameters). Two EM waves are incident at angles of $\pm 23^\circ$. For each beam, the single-beam maximum-growth-rate curves for TPD¹⁰ are shown as dashed lines, while the solid red line defines the Landau cutoff. (b) The TPD growth rate in arbitrary units from the theory of Short³⁷ for the same parameters as in (a).



TC9253JR

Figure 126.15

The solid line shows the modified 1-D density profile $\tilde{N}(x) \equiv \langle N(x) + \delta n(x,y) \rangle_y$ normalized to the critical density n_c , taken at the time of saturation of the absolutely unstable eigenmode ($t = 1.2$ ps) for the simulations described in **Zakharov Predictions for the Saturated LW Spectrum** (p. 68). The dashed line approximates the slope in the neighborhood of quarter critical and is used to define the modified density scale length \tilde{L}_n .

of the longitudinal electric-field intensity [Fig. 126.14(a)], where the active region of LW's extends as far as the Landau cutoff at wave numbers $k \sim 0.25 k_{De}$ (solid red line). These unstable modes, which are convective in nature, come to dominate the saturated LW spectrum at later times. The broad spectrum in Fig. 126.14(a), which corresponds to irradiation by two crossed beams, is dominated by the common LW and its associated daughter waves. This can be seen by comparing the spectral features in Fig. 126.14(a) with the expected growth rate based on a multiple-beam theory for identical parameters³⁷ [Fig. 126.14(b)]. The predicted maximum growth rate occurs at the intersection of the single-beam maximum growth rate curves (shown by the dashed lines) in Fig. 126.14. The growth rate has quite a broad peak, extending beyond the Landau cutoff (solid circle) for positive wave numbers—although the crossed-beam theory ignores wave damping. The absolute mode would appear to be relatively unimportant in the saturated state.

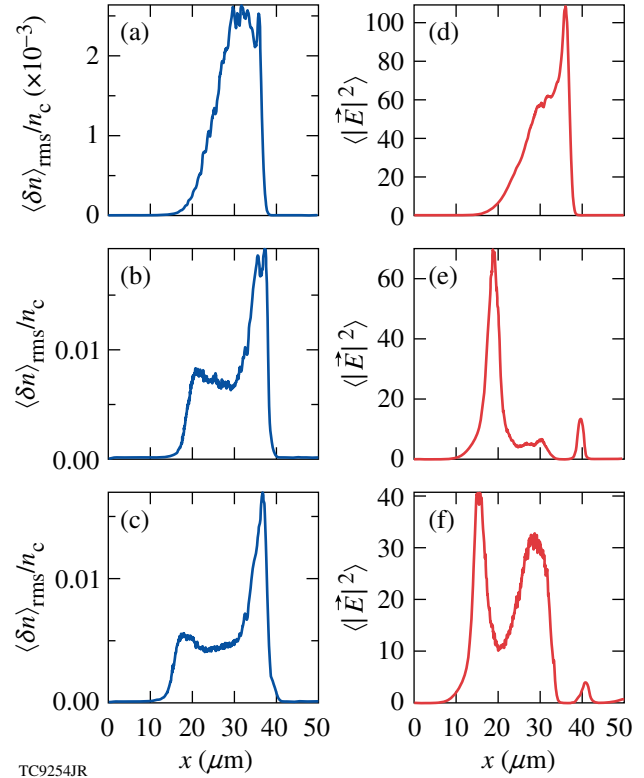
Yan *et al.*^{9,22} demonstrated that the convective Rosenbluth gain in amplitude [$g_R \sim \exp(\pi\Lambda)$] for the large k_\perp TPD modes can be simply written in terms of the Simon *et al.* threshold parameter for absolute instability

$$\pi\Lambda = 2.5 \left(1 - 0.0088 T_{\text{keV}} - 0.0047 T_{\text{keV}} \tilde{k}_\perp^2 \right) \eta,$$

where $\tilde{k} \equiv ck/\omega_0$. Convective gain in intensity is therefore several times larger than the threshold parameter and very weakly

dependent upon the transverse wave number for the parameters of current interest. Close to threshold, all transverse modes up to the Landau cutoff can saturate convectively without the need for nonlinear processes. As laser intensity increases, these convective modes are observed to saturate as a result of the excitation of large-amplitude ion-acoustic perturbations with relative-density perturbations on the few-percent level.

Features of the growth and nonlinear saturation of Fourier modes that come to dominate the spectrum at times $t \gtrsim 1.2$ ps in the case of single-beam illumination are illustrated in Fig. 126.16. The left-hand column [Figs. 126.16(a)–126.16(c)] shows a series of snapshots of the low-frequency density perturbations $\langle \delta n \rangle_{\text{rms}}(x)/n_c$ taken at different times (see figure caption). Note that the reference n_0 and linearly varying part of the density $\delta N(x)$ have been extracted and that a one-dimensional lineout has been obtained by taking the root-mean-square (rms) average over the transverse (y) coordinate,



TC9254JR

Figure 126.16

The left-hand column [(a)–(c)] shows a series of snapshots of the 1-D density perturbation $\langle \delta n \rangle_{\text{rms}}/n_c$, while the right-hand column [(d)–(f)] shows the transverse average of the LW excitation level $\langle |\vec{E}|^2 \rangle$, both plotted against the longitudinal coordinate x (in microns). From top to bottom, the rows correspond to times $t = 1.2$, $t = 2.0$, and $t = 2.4$ ps. The figure illustrates the correlation between LW amplitude and the region over which $\langle \delta n \rangle_{\text{rms}}/n_c \gtrsim 0.5\%$.

$$\langle \delta n \rangle_{\text{rms}}(x_i) \equiv \left[\left(1/n_y \right) \sum_{j=1}^{n_y} \delta n(x_i, x_j) \right]^2 \Bigg]^{1/2},$$

where n_y is the number of transverse grid points. The right-hand column [Figs. 126.16(d)–126.16(f)] shows the normalized LW excitation level $\langle |\tilde{E}|^2 \rangle$ averaged over the transverse direction.

Figure 126.16(a) shows the situation at $t = 1.2$ ps, where the convective LW growth is well described by the linear evolution. The excitation of the LF density perturbations is due to the nonlinear ponderomotive force [first term on the left side of Eq. (2)] of the unstable LW's and has a negligible effect on LW growth given by Eq. (1) (its contribution is negligible compared to the damping rate, for example). In Fig. 126.16(d), the LW's appear to grow more rapidly at higher density for reasons that are not fully understood. As time progresses [Fig. 126.16(b)], the density perturbation $\langle \delta n \rangle_{\text{rms}}(x)$ level has grown significantly and is at the few-percent level. A two-dimensional Fourier analysis of the density perturbations (not shown) reveals these perturbations to be IAW's driven in response to the ponderomotive beating of primary TPD LW's, a feature previously identified in the reduced PIC calculations of Vu *et al.*¹⁰ The absolute mode has saturated as described above. Notice that the maximum in the LW excitation level $\max \left[\langle |E|^2 \rangle(x) \right]$ occurs at roughly $x = 19 \mu\text{m}$, which is the point where $\langle \delta n \rangle_{\text{rms}}(x)/n_c$ falls below 0.5%. This peak in LW excitation moved to this location continuously from near $n_e = 0.25 n_c$, following the boundary of density excitations. For larger values of x , there is evidence of saturation of the LW amplitude. The saturation leads to a lower level of LW amplitudes and a weakening of the ponderomotive excitation of δn .

The onset of a new type of behavior is shown in Figs. 126.16(c)–126.16(f). The LF density perturbations have decreased to a value of $\langle \delta n \rangle_{\text{rms}}/n_c \lesssim 0.5\%$. This appears to permit some renewed growth of the LW's (i.e., at $x = 30 \mu\text{m}$) and leads to a new peak in LW excitation located close to the minimum in $\langle \delta n \rangle_{\text{rms}}/n_c$. This close correlation between the evolution of $|E|^2$ and δn is given as evidence of the detuning effect of LF density perturbations on the convective growth of TPD modes. We recall that this is the same mechanism proposed as the saturation mechanism for TPD in the *OSIRIS* PIC calculations of Yan *et al.*⁹ It would appear that density perturbations need to exceed the level $\langle \delta n \rangle_{\text{rms}}/n_c \approx 0.5\%$ in order to be effective. An alternate description of nonlinear saturation will be given in a paper by Vu *et al.*,³⁸ where evidence is presented from RPIC and Zakharov simulations that Langmuir collapse is the essential dissipative saturation mechanism in these relatively weakly driven regimes, with the Langmuir decay instability (LDI) playing a minor role.

In general, the evolution of the LW spectrum to a steady state is observed to take several tens of picoseconds. While oscillations of the kind described above persist, the spectrum becomes “steady” only after roughly one acoustic transit time across the density range Δn spanning from the Landau cutoff to quarter-critical. For canonical parameters, this time is $t_{\text{sat}} \sim \Delta x/c_s = (\Delta n/n_0) L_n \times 1/c_s \approx 100$ ps. This steady LW spectrum is used below to investigate the generation of hot electrons.

b. Estimate of the maximum energy gain for an electron in transit through the interaction region. The late-time (saturated) LW spectrum obtained from the Zakharov calculations on p. 68, although broad, is dominated by a shared common wave and the corresponding daughter waves whenever the irradiation consists of symmetrically arranged, overlapping plane waves (Fig. 126.14) (an effect that may explain the experimentally observed scaling of preheat on overlapped-beam intensities⁴). Since this is the usual experimental configuration on OMEGA, consider the simple case where the action on the plasma electrons is due to a single coherent LW wave. In this case, an estimate for the expected scale of electron heating can be obtained (although it should be noted that similar numbers can be obtained without invoking the common wave). Taking the wave numbers of the LW's at their point of origin to be $k\lambda_{\text{De}} = 0.16$ and 0.07 , respectively (see Fig. 126.14) (the common wave is only resonant at a particular density;¹⁰ here the density is $n_e/n_c = 0.241$), then the trapping width can be estimated from the formula

$$v_{\text{tr}} = 2(e\mathcal{E}_l/m_e k)^{1/2} = 2(v_{\text{osc}} v_{\phi})^{1/2},$$

where $v_{\text{osc}} = e\mathcal{E}_l/(m_e \omega)$ is the oscillatory velocity of an untrapped electron and $v_{\phi}/v_{\text{Te}} = 1/k\lambda_{\text{De}}(1 + 3k^2\lambda_{\text{De}}^2)^{1/2}$ is the LW phase velocity for a wave satisfying the Bohm–Gross dispersion relation $\omega^2 = \omega_p^2(1 + 3k^2\lambda_{\text{De}}^2)$. In practical units the trapping width becomes

$$\begin{aligned} \frac{v_{\text{tr}}}{v_{\text{Te}}} &= 0.37 \left(\frac{1}{k\lambda_{\text{De}}} \right)^{1/2} \left(\frac{\lambda_0}{0.351 \mu\text{m}} \right)^{1/2} \\ &\times \left(\frac{I_{14}}{T_{e,\text{keV}}} \right)^{1/4} \left(\frac{\mathcal{E}_l}{\mathcal{E}_i} \right)^{1/2}. \end{aligned} \quad (4)$$

Substituting the wave numbers for the common and daughter waves gives the values

$$v_{\text{tr}} = 1.38 v_{\text{Te}} (\mathcal{E}_l/\mathcal{E}_i)^{1/2}$$

and $2.1 v_{\text{Te}} (\mathcal{E}_l/\mathcal{E}_i)^{1/2}$, respectively. In both cases the trapping width is insufficient to trap thermal electrons because of the

high phase velocity of the waves ($v_\phi/v_{Te} = 6.49$ and 14.40 for the common and daughter LW's, respectively). As a result, wave breaking will not easily occur.³⁹

The presence of the density gradient modifies the propagation of the TPD-produced LW's from their point of origin. Theoretical treatments of wave-particle interaction that lead to particle trapping and acceleration most often consider unbounded homogeneous plasma.^{40,41} The present situation involves both a spatially localized region of LW excitation (excitation is restricted to densities in the range $0.2 \leq n_e/n_c \leq 0.25$) and plasma inhomogeneity. Of most importance is the inhomogeneity in the plasma density. For example, the common wave, which is blue shifted with respect to $\omega_0/2$, propagates up the density gradient. For a freely propagating LW of fixed frequency ω , the wave number will decrease in order to preserve the dispersion relation as the local density (and plasma frequency) increases. The phase velocity will likewise increase $v_\phi = v_{Te} \left\{ 3\omega^2 / [\omega^2 - \omega_p(x)^2] \right\}^{1/2}$, at some point becoming superluminal (the group velocity has the opposite dependence, $V_g = 3v_{Te}/v_\phi$). The density at which the LW will turn depends on its frequency. The daughter wave (red-shifted plasmon) propagates down the gradient. Its phase velocity decreases until it becomes a few times the thermal velocity and the wave is damped (the Landau cutoff).

The density gradient creates the potential for electron acceleration to higher energies than can be obtained in homogeneous plasma since the phase-velocity increase can keep pace with the electron as it is accelerated up the gradient.⁴² Given an arbitrary LW amplitude, it might be possible to accelerate electrons to arbitrarily high energies, but, practically, there will come a point at which the maximum acceleration in the LW field will be insufficient to match the acceleration of the LW phase velocity. Following Brooks *et al.*⁴² (with a trivial generalization to include relativistic velocities), the magnitude of the largest-attainable acceleration may be simply obtained from the relativistic momentum equation for electrons $|v'|_{\max} = e\mathcal{E}_l/(\gamma^3 m_e)$ by assuming the electron maintains constant phase with respect to the LW. In practical units the maximum-attainable acceleration is

$$|v'_{\text{ph}}|_{\max} = 1.5 \times 10^{24} I_{15}^{1/2} \gamma^{-3} (\mathcal{E}_l/\mathcal{E}_i) \text{ cm/s}^2,$$

where the prime denotes the time derivative. Equating this with the acceleration of the LW phase velocity up the density gradient $v'_\phi(x) = v_\phi^2(x) \omega_p(x)^2 [\omega^2 - \omega_p^2(x)]^{-1} / (2L_n)$ enables one to calculate the location x and phase velocity at which the electron can no longer remain in phase $(v_\phi)_{\max}$ —the above is solved iteratively since the relativistic gamma factor is dependent on the phase velocity $\gamma(v_\phi) = (1 - v_\phi^2/c^2)^{-1/2}$.

The energy gain is given by $\Delta E/(m_e c^2) = \gamma [(v_\phi)_{\max}] - \gamma [(v_\phi)_0]$, where $(v_\phi)_0$ is the initial (phase) velocity of the electron (LW). Substituting in values $I_{15} = 1$, $\mathcal{E}_l = \mathcal{E}_i$, and $(v_\phi)_0 = 6.49 v_{Te}$ from the Zakharov calculations presented in **Zakharov Predictions for the Saturated LW Spectrum** (p. 68) gives an estimate for the energy gain of $\Delta E \sim 110$ keV (or $\Delta E \sim 177$ keV for $\mathcal{E}_l = 2 \mathcal{E}_i$).

The actual situation does not involve a single coherent wave, but rather there are many waves whose resonances are expected to have significant overlap, leading to orbits that become diffusive. It might be possible to approximate the stochastic acceleration of electrons in the predicted LW fields with a self-consistent Fokker-Planck⁴³ or quasilinear model.^{11,29,30} To estimate the heating effect more accurately and to investigate the importance of reheating, test electron trajectories are directly integrated in the LW fields predicted by the Zakharov model of **Zakharov Predictions for the Saturated LW Spectrum** (p. 68). This will also form the basis for future work that will examine the applicability of quasilinear diffusion³²⁻⁴⁴ for the two-plasmon-decay instability.

2. Test-Particle Equations of Motion

Test-particle motion is governed by the relativistic Newton-Lorentz equations. For the i^{th} electron test particle, these are

$$\frac{d\vec{x}_i}{dt} = \vec{v}_i, \quad (5)$$

$$\frac{d\vec{p}_i}{dt} = -e \left[\vec{\mathcal{E}}_l(\vec{x}_i, t) + \vec{\mathcal{E}}_l(\vec{x}_i, t) + \vec{v}_i/c \times \vec{\mathcal{B}}(\vec{x}_i, t) \right], \quad (6)$$

where $\vec{p}_i = \gamma_i m_0 \vec{v}_i$ is the electron momentum. The longitudinal electric field $\vec{\mathcal{E}}_l$ is associated with the LW's resulting from the TPD instability and is obtained from the Zakharov field \vec{E} by restoring the carrier frequency ω_{p0} (which was explicitly removed in the Zakharov approximation)

$$\vec{\mathcal{E}}_l(\vec{x}, t) = 1/2 \vec{E}(\vec{x}, t) \exp(-i\omega_{p0}t) + \text{c.c.} \quad (7)$$

The transverse fields $\vec{\mathcal{E}}_t$ and $\vec{\mathcal{B}}$ are associated with the incident laser light and are currently ignored when computing test-particle trajectories (they are prescribed fields in the current extended Zakharov model). Although the transverse electric-field strength is quite large,

$$\mathcal{E}_t \sim 8.7 \times 10^8 \left(I_0 / 1 \times 10^{15} \text{ W/cm}^2 \right)^{1/2} \text{ V/cm},$$

it is not effective in accelerating electrons at nonrelativistic laser intensities ($I_0 \lesssim 10^{18} \text{ W/cm}^2$). The transverse fields result merely in a "quiver" imposed on the unperturbed motion. The

quantity $\vec{\mathcal{E}}_i$ is defined only at discrete spatial locations that are determined by the discretization (grid points) used in the numerical solution of Eqs. (1) and (2) and is interpolated onto the i^{th} test electron position \vec{x}_i using bilinear interpolation. The test-particle equations [Eqs. (5) and (6)] are integrated numerically using a fourth-order Runge–Kutta scheme.

Ensemble averages of test-particle quantities are obtained by averaging over test-particle initial conditions $\vec{x}_i(t=0)$ and $\vec{p}_i(t=0)$ since averaging over realizations of the electric-field spectrum is impractical. The initial position of a test particle $\vec{x}_0 \equiv \vec{x}(t=0)$ is a random variable defined on $\Omega = [0, l_x] \times [0, l_y]$ with a uniform probability distribution $f(\vec{x}_0)d\vec{x}_0 = d\vec{x}_0/(l_x l_y)$. The initial momentum $\vec{p}_0 \equiv \vec{p}(t=0)$ is given by

$$\vec{p}_0 = p_0 [\hat{e}_x \sin(\phi) + \hat{e}_y \cos(\phi)],$$

where the magnitude of the momentum p_0 is fixed according to a given kinetic energy

$$p_0 = m_0 c \left[\left(T_0 / m_0 c^2 + 1 \right)^2 - 1 \right]^{1/2},$$

while the angle ϕ is a uniform random variable on $[0, 2\pi]$ with the probability distribution $f(\phi)d\phi = d\phi/(2\pi)$. The effect of the finite boundary on the particle trajectories is addressed in the following section, while the boundary conditions on the longitudinal fields are periodic in the transverse direction $\vec{\mathcal{E}}_i(x, y + l_y) = \vec{\mathcal{E}}_i(x, y)$ and vanish at the longitudinal boundaries $\vec{\mathcal{E}}_i(x=0, y) = \vec{\mathcal{E}}_i(x=l_x, y) = 0$ (see Fig. 126.17).

3. Estimation of Global Particle Trajectories

For the numerical simulation of Eqs. (5) and (6), any potential for electrons to re-enter the TPD active region after their transit through the simulation domain must be manifested

through the boundary conditions because of limitations placed on the maximum size of the region over which Eqs. (5) and (6) can be realistically integrated. In general, the problem of boundary conditions in kinetic^{29,30} or PIC calculations⁹ is usually addressed by assuming that transverse boundaries are periodic, while longitudinal boundaries are thermalizing. The thermal boundary conditions have the effect of driving the electron-distribution function to a Maxwellian,³⁰ which may or may not be physically reasonable. It is clear that the choice of boundary condition has a significant impact on the properties of the hot-electron spectrum.^{11,28} Such a “thermalizing” scheme is easily implemented for test particles in Eqs. (5) and (6) above. Inspection of the target areal densities relevant to OMEGA implosions at the time of TPD instability ($\rho R \sim 10^{-2}$ g/cm²) shows, however, that they are unlikely to be completely stopped [the range $r_0 = 6.65 \times 10^{-2}$ g/cm² for an electron of energy of 100 keV in hydrogen in the continuous-slowing-down approximation—energies corresponding to those estimated in **Estimate of the Maximum Energy Gain for an Electron in Transit Through the Interaction Region** (p. 71) and observed experimentally^{41,45}]. As a result, an estimate of the effect of electron recirculation is needed.

The spherical nature of the quarter-critical surface means that hot electrons can pass through the center of the target and re-encounter it once more on the opposite side (as long as they are sufficiently energetic so as not to range out; i.e., trajectories of type A, shown in Fig. 126.18). Less obvious is the fact that electrons on outward-bound trajectories (heading away from the target) may also be reflected back by the presence of sheath fields^{11,46,47} (trajectory of type B, shown in Fig. 126.18). The possibility therefore exists for complex orbits where electrons can be accelerated multiple times by the TPD active region near the quarter-critical surface.

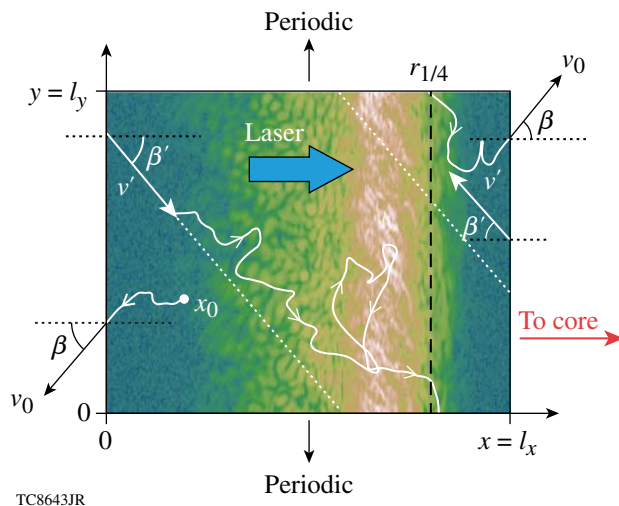


Figure 126.17

An illustration of how the boundary conditions for electron test particles are implemented. The region $\Omega = [0, l_x] \times [0, l_y]$ over which the LW fields are calculated is shown, where the colors correspond to the magnitude $|\vec{\mathcal{E}}(x, y)|^2$ from a particular run. Periodicity is assumed for trajectories crossing the transverse boundaries ($y=0$ or $y=l_y$), while a test particle reaching a longitudinal boundary ($x=0$ or $x=l_x$) at time t with angle β and energy E_0 is re-injected at the same boundary at the later time $t' = t + \Delta t$ with a reduced energy $E' = E_0 - \Delta E$. The position along the boundary at reinjection is randomized, while its angle is given by $\beta' = \beta$. The white curve illustrates this process for an imaginary trajectory.

TC8643JR

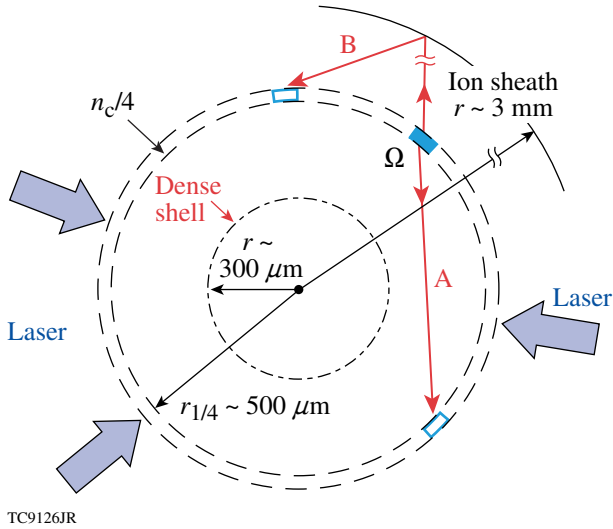


Figure 126.18

A schematic drawing showing a two-dimensional plane passing through the origin of a spherical implosion and containing the plane region Ω over which the extended Zakharov equations are simulated. The region Ω is illustrated by the blue shaded rectangle spanning the radius of the quarter-critical density surface, $r_{1/4}$. Periodicity (modulo l_y) is assumed in the tangential direction so that the whole annular region bounded by the dashed concentric circles is assumed to be modeled (mapped onto) Ω . Because of the spherical geometry, electrons that leave the region Ω in the direction of the origin (trajectory of type A as indicated) can re-intersect the quarter-critical surface and re-enter Ω . Outgoing trajectories (type B) can also return because of reflection from the ion sheath. Dimensions characteristic of OMEGA implosions are indicated.

The global radiation hydrodynamics of an imploding target at any given time during an implosion is calculated with the one-dimensional radiation–hydrodynamics code *LILAC*²⁷ without consideration of the effects of TPD (i.e., no increased absorption or effects of preheat). The parameters are taken to be those of current cryogenic implosion experiments on OMEGA at the time of peak TPD instability. These parameters place the quarter-critical surface at a radius of $r_{1/4} \sim 500 \mu\text{m}$, while the dense shell is at a radius of approximately $300 \mu\text{m}$ (see Fig. 126.18). The energy loss and time of flight associated with the electron trajectories beyond the quarter-critical surface are approximated below by “unperturbed” trajectories. That is, the energy loss and time of flight between an electron leaving the critical surface and returning (either by passing through the core or by reflection by sheath fields far out in the corona⁴⁶) are estimated assuming a straight-line trajectory with angle and energy given by the values on leaving the quarter-critical surface. The time of return will be delayed by an amount that is dependent on the particular boundary that has been crossed and the details of the trajectory. Periodicity in the transverse (y) direction is motivated by the fact that the radius of curvature of the quarter-critical surface is much larger (typically ten times

larger) than the lateral extent l_y of the simulation volume (and therefore the correlation length for \vec{E}).

a. Practical implementation of delay-type boundary conditions on test particles. At the boundary of the Zakharov calculation located at $x = l_x$ (see Fig. 126.17), which looks toward the target core, electrons crossing at time t with angle $\beta = \cos^{-1}(\vec{p} \cdot \hat{n}/p)$ with respect to the outward normal \hat{n} of the simulation volume ($\hat{n} = \hat{e}_x$) cut a chord of length $s_{\text{max}} = 2 r_{1/4} \cos(\beta)$ across the circle that describes the intersection of the quarter-critical surface with the plane defined by the laser polarization vector and the radius vector defined with respect to target origin (Fig. 126.18). Note that this angle (β) is, to an excellent approximation, the same as the angle between the negative radius vector and the electron momentum vector ($\hat{n} \approx -\hat{e}_r$). The radius $r(s)$ along this chord as a function of path length s is given by $r^2 = r_{1/4}^2 + s^2 - 2(r_{1/4}s)\cos(\beta)$, and inverting this function allows one to specify the hydrodynamic variables $n_e(r)$, $T_e(r)$ from the hydrocode *LILAC* along the trajectory, $n_e(s)$, $T_e(s)$. The time of flight for an electron to transit the path is estimated by

$$\Delta\tau = \frac{1}{c} \int_0^{s_{\text{max}}} \frac{ds}{\beta_e(s)}, \quad (8)$$

where the particle velocity is computed in terms of its energy $E(s)$ according to

$$\beta_e(s) = \left\{ \frac{2E(s)/m_e c^2 + [E(s)/m_e c^2]^2}{[1 + E(s)/m_e c^2]^2} \right\}^{1/2} \quad (9)$$

with

$$E(s) = E_0 - \int_0^s \left| \frac{dE}{ds} \right| ds \quad (10)$$

being the kinetic energy of the electron as a function of distance s along the path. The total energy loss along the path is simply $\Delta E = E_0 - E(s_{\text{max}})$. The stopping power $-dE/ds$ is given by $-dE/ds = e^2 \omega_p^2 / (c^2 \beta_e^2) \log[\beta_e^2 m_e c^2 / (\hbar \omega_p)]$. With the above assumptions, the energy loss ΔE and time delay Δt may be computed as a function of energy E_0 and angle β .

As mentioned previously, there is also a possibility that electrons leaving the outer simulation boundary ($x = 0$) (see Fig. 126.17) will return. This time, the effect is not geometrical but is instead related to the formation of a plasma sheath far out in the corona^{46,47} (see Fig. 126.18). In principle the structure and dynamics of the sheath formation are complicated and coupled to the hot-electron–generation mechanism itself, which

requires a level of knowledge that is currently unavailable. Here we take a practical approach and adopt a greatly simplified model that has been previously used by Delettrez *et al.*⁵ This has the advantage of facilitating comparisons between the current work and the phenomenological model of Delettrez *et al.* The model specularly reflects electrons when they reach the radius of the last Lagrangian cell of the *LILAC* calculation. The total path length is therefore given by $s_{\max} = 2 l_{\text{exc}}$, where $l_{\text{exc}} = r_{\text{sh}} \cos(\Theta) - r_{1/4} \cos(\beta)$ is the distance to the last Lagrangian cell of the *LILAC* calculation, r_{sh} is its radius, and $\Theta = \sin^{-1} [r_{1/4} / r_{\text{sh}} \sin(\beta)]$. The radius is now given in terms of the path length according to $r^2 + s^2 + r_{1/4}^2 + 2(r_{1/4}s) \cos(\beta)$ for $s \leq l_{\text{exc}}$, and by $r^2 = (2l_{\text{exc}} - s)^2 + r_{1/4}^2 + 2r_{1/4}(2l_{\text{exc}} - s) \cos \beta$ for $s > l_{\text{exc}}$.

The energy losses and time delays as a function of electron momentum (energy and angle) are precomputed and stored in look-up tables, one for each longitudinal boundary. Figures 126.19 and 126.20 show examples of look-up tables for the boundary at $x = l_x$ corresponding to a cryogenic implosion on OMEGA (shot 45009) at the time of experimental onset of two-plasmon-decay signatures (roughly 2.5 ns from the start

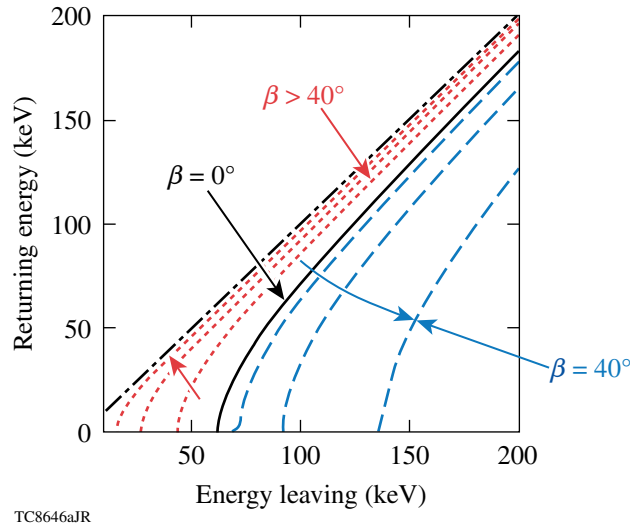


Figure 126.19

Look-up tables for energy loss at the $x = l_x$ boundary (i.e., type-A trajectories in Fig. 126.18) corresponding to OMEGA shot 45009 at time $t = 2.5$ ns. Angle β is the angle between the outward normal of the boundary ($\approx -\hat{e}_r$) and the direction of the electron-velocity vector (see Fig. 126.17). As β increases from 0° [radially inward trajectory (black solid curve)] to $\beta \leq 40^\circ$, the energy loss increases (i.e., the blue dashed curves move as indicated by the arrow). The effect is due to the increased path length in the dense compressed shell (see Fig. 126.18). Maximum energy loss occurs at $\beta \approx 40^\circ$. For angles greater than 40° (red dotted curves) the energy loss falls dramatically and vanishes at $\beta = 90^\circ$ since the trajectories no longer intersect the dense shell and the path length vanishes.

of the pulse). Test particles, upon reaching the boundary, are re-injected at the same boundary at a later time $t + \Delta t$ with the modified angle $\beta' = -\beta$ and energy $E_0 - \Delta E$. The transverse coordinate of the returning electron is randomized, taking the new position to be a uniform random variable on $[0, l_y]$. This is illustrated in Fig. 126.17. If a particular energy loss results in a re-injected energy of the electron falling below a threshold value (typically $E_{\text{cut}} = 200$ eV), the trajectory is terminated.

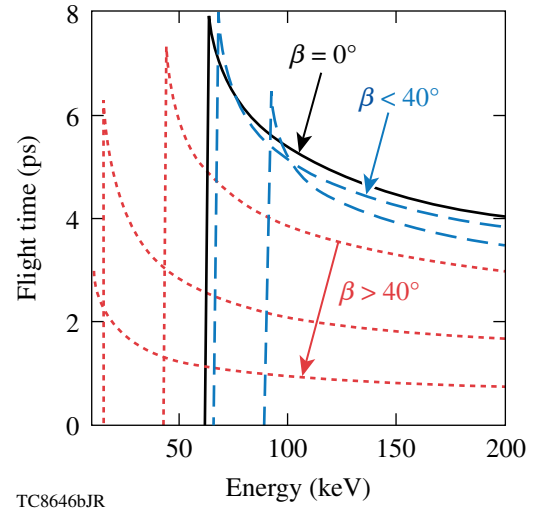


Figure 126.20

An example of the boundary look-up tables for time delay Δt at the $x = l_x$ simulation boundary corresponding to OMEGA shot 45009 at time $t = 2.5$ ps. The delay reaches a maximum value of $\Delta t \sim 8$ ps for trajectories that are nearly radial (inward) ($\beta \approx 0^\circ$), and it vanishes for tangential trajectories $\beta = 90^\circ$. The curves types/colors are the same as described in Fig. 126.19.

Results of Test-Particle Calculations

To quantify the contributions from separate processes, the effect of heating is first calculated with absorbing/thermal boundary conditions in the longitudinal direction, while periodicity is assumed in the transverse direction. This corresponds either to a massive target in which all hot electrons range out or alternatively to the usual boundary conditions that are applied in the kinetic modeling of TPD using PIC codes.^{9,10} The density scale length is varied within the range $L_n = (100 \text{ to } 350) \mu\text{m}$, while holding the electron temperature fixed at $T_e = 2$ keV. This addresses the range currently accessible on OMEGA and, for the longer scale lengths, the range accessible in the near future on OMEGA EP. The laser intensities are chosen to be between $I_L = (0.1 \text{ to } 2.0) \times 10^{15} \text{ W/cm}^2$. With this choice, the absolute TPD instability is found to be slightly above threshold to approximately three times above threshold [$\beta = (1.15 \text{ to } 3.1)$] according to the formula of Simon *et al.*¹³ Finally, the impact of reheating is addressed by taking as an example the hydro-

dynamic conditions of a cryogenic implosion that has been fielded on OMEGA (shot 45009) and computing the effects of reheating on the hot-electron temperature as the laser intensity is increased (within the above quoted range).

Figure 126.21 shows the energy distribution of test electrons as a function of electron energy for a typical case. The initial energies were chosen from a Maxwellian distribution of temperature $T_e = 2$ keV, chosen to be consistent with the electron temperature used in the Zakharov calculation. Note that the deviation from the initial Maxwellian occurs at an electron kinetic energy of roughly 20 keV. This is consistent with the smallest phase-velocity waves (largest wave number) observed in the LW spectrum (Fig. 126.14). The tail is well fit by an exponential, the slope of which is used to define an effective hot-electron temperature T_{hot} .

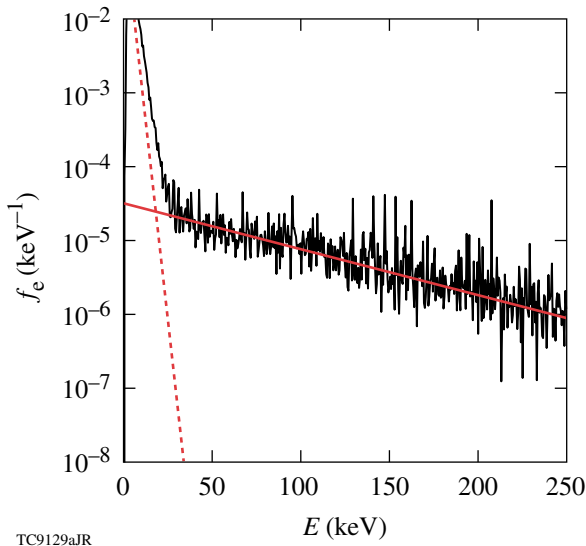


Figure 126.21

The electron test-particle distribution function $f_e(E)$ as a function of electron energy E constructed from an ensemble of 10^6 trajectories. The slope of the distribution function for energies $E \lesssim 30$ keV is close to the temperature of the sample distribution ($T_e = 2$ keV) as indicated by the steep dashed red line. For energies $E \gtrsim 30$ keV, a hot tail is observed. The slope of the hot tail is well fit by an exponential (solid red line), which is used to define an exponential slope temperature T_{hot} .

Figure 126.22 shows the hot-electron temperature T_{hot} inferred from a series of simulations, with the parameters as defined above, plotted against the threshold parameter η . Recall that density scale length and laser intensity are being varied, and while there is a small scatter in the inferred temperature for different combination of L_n and I giving the same η , the hot temperature is well predicted by the value of η alone. A hot component is generated once η has slightly exceeded unity

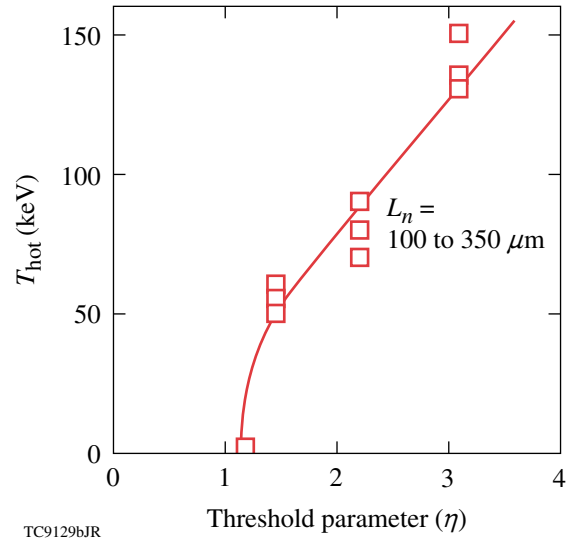


Figure 126.22

The hot-electron temperature T_{hot} as determined by the electron test-particle distribution function for a series of extended Zakharov realizations plotted against the threshold parameter $\eta [= I_{14} L_{\mu\text{m}} / (230 \text{ keV})]$. For a given η , the open squares show the effect of varying the density scale length in the range $L_n = (100 \text{ to } 350) \mu\text{m}$ while holding the initial electron temperature T_e fixed (intensities were adjusted appropriately). The red (solid) line indicates the general trend.

(which is also an experimental observation³) and increases from $T_{\text{hot}} \sim 50$ keV at $\eta = 2$ to a value of ~ 140 keV at $\eta = 3.0$.

The insensitivity of the hot-electron temperature to density scale length for a fixed value of the threshold parameter η is shown in Fig. 126.23. Once again, as the density scale length is increased, the laser intensity is decreased in order to keep the value of η constant. Solid lines connect simulation points having constant η , while the filled markers correspond to a laser intensity of $I_L = 4.8 \times 10^{14} \text{ W/cm}^2$. From the filled markers, the rapid increase in hot-electron temperature with density scale length can be visualized. The reason for this insensitivity can be determined upon an examination of the Zakharov predictions for the nonlinearly saturated LW spectrum in each case. Figure 126.24 shows the rms electric field taken over each Zakharov simulation volume (adjusted with L_n to span the density range of $0.19 < n_e/n_c < 0.27$). While the value of $\langle E \rangle_{\text{rms}}$ depends on the value of the threshold parameter for a given scale length and is of the order of $\langle E \rangle_{\text{rms}} = 10^6$ statvolts/cm for fixed η , it decreases with density scale length. It is therefore the laser intensity that determines the level of LW excitation. The acceleration of hot electrons, very crudely speaking, is given by the characteristic electric field multiplied by the acceleration length. In this way, the increasing acceleration length is offset by the reduction in electric field.

The above results have ignored the possibility of multiple transits of the hot electrons through the quarter-critical region

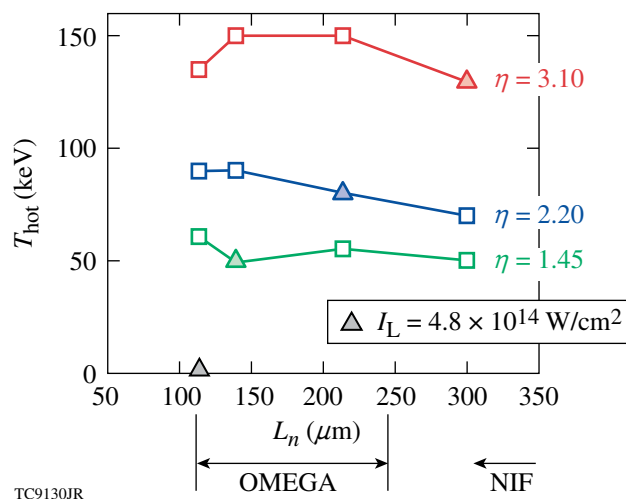


Figure 126.23

The hot-electron temperature T_{hot} in keV as determined by the electron test-particle distribution function for a series of extended Zakharov realizations plotted against density scale length L_n in microns. The upper (red), middle (blue), and lower (green) curves correspond to values of the threshold parameter of $\eta = 3.10, 2.20,$ and $1.45,$ respectively. The filled triangles correspond to a laser intensity of $I_L = 4.8 \times 10^{14} \text{ W/cm}^2$. In all cases the initial electron temperature was $T_e = 2.0 \text{ keV}$.

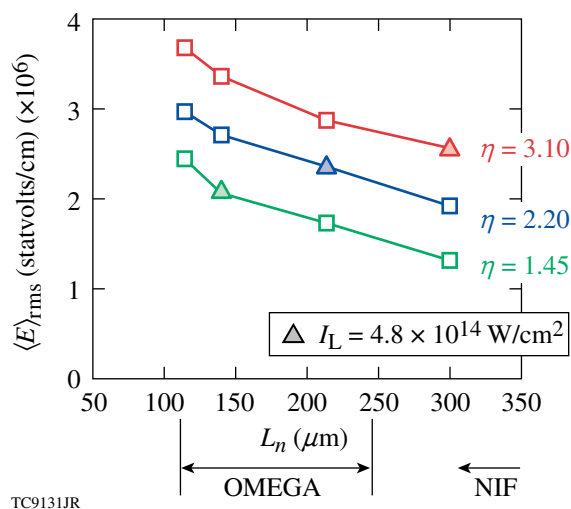


Figure 126.24

The root-mean-square electric field at saturation obtained from a series of extended Zakharov runs with an electron temperature $T_e = 2 \text{ keV}$ plotted against density scale length L_n in microns. The upper (red), middle (blue), and lower (green) curves correspond to values of the threshold parameter of $\eta = 3.10, 2.20,$ and $1.45,$ respectively. It is evident that for a given value of η and for a fixed electron temperature, the rms electric field decreases with an increase (decrease) in density scale length L_n (laser intensity I_L). The filled markers correspond to a laser intensity of $I_L = 4.8 \times 10^{14} \text{ W/cm}^2$.

and therefore multiple stages of acceleration. The size of this effect has been demonstrated by implementing the boundary conditions exactly as described in **Practical Implementation of Delay-Type Boundary Conditions on Test Particles** (p. 74) (see Fig. 126.25). Look-up tables corresponding to shot 45009 at a time near the peak drive, when $\rho R \approx 1 \times 10^{-2} \text{ g/cm}^2$, have been used (Figs. 126.19 and 126.20). In Fig. 126.25 the square symbols show the hot-electron temperature as a function of the threshold parameter η with absorbing boundaries, while the circles show the hot-electron temperature when the “physical” boundary conditions are adopted. It can be seen that there is a significant effect; corresponding to an ($\sim 3\times$) increase in the hot-electron temperature. This demonstrates the futility of studying an isolated region of the target near the quarter-critical density when attempting to compute hot-electron temperature and, by extension, the expected hot-electron preheat. This is an extremely unfortunate result since the mixing of spatial scales is severe. On one hand, the LW wavelength must be resolved (which is submicron), while on the other, electron trajectories must be traced over millimeters. A similar mixing (four orders of magnitude) also holds for the temporal scale.

The size of the effect obviously increases in importance with higher one-pass temperatures since more-energetic electrons can more freely pass through the core. So as to not overstate

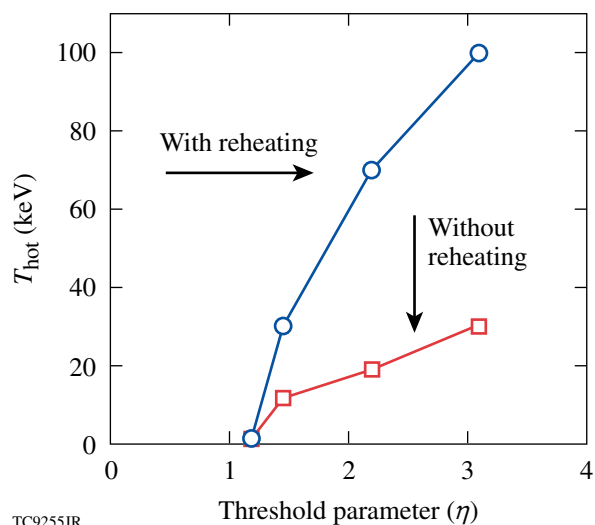


Figure 126.25

The hot-electron temperature T_{hot} in keV as a function of the threshold parameter η . The hot temperature was determined from the electron test-particle energy distribution for test-particle trajectories employing thermal boundary conditions (red curve) and delay-type boundary conditions as described on p. 74 (blue curve). The density scale length L_n and electron temperature T_e were held constant at $150 \mu\text{m}$ and 2 keV , respectively, while the intensity was varied.

the size of the effect, the one-pass temperatures were actually reduced from the pure Zakharov predictions in making these calculations (e.g., comparison of Fig. 126.25 with Fig. 126.22 shows a smaller one-pass temperature). In fact, when computing test-particle heating for Fig. 126.25, the predicted electric field \vec{E} has been reduced artificially (“renormalized”) in magnitude [only where it appears in Eq. (6)] so that the resulting hot-electron temperature, in the case of thermal boundaries, is computed to be no larger than the best current estimate based on reduced description particle-in-cell modeling.²⁸ It might be expected that the non-self-consistent test particle model would lead to exaggerated hot-electron temperatures because of the absence of any modification to the linear dispersion (damping) caused by the hot tail. It is hoped that a self-consistent treatment using a quasilinear model will remove the need for such renormalization.

Summary and Discussion

An extended Zakharov model of two-plasmon-decay instability has been presented and used to predict the saturated LW spectrum in the absence of electron kinetic effects (heating). The parameters were motivated by current OMEGA experiments, and the assumed electron temperature and density profiles were defined by 1-D radiation hydrodynamic (*LILAC*) calculations for a given time corresponding to peak TPD instability.

The LW spectrum has been observed to evolve as a consequence of the interaction between the unstable LW’s and LF density fluctuations. It was argued that convectively unstable modes come to dominate the late-time spectrum, while the absolute TPD model is relatively unimportant after initial saturation by profile modification. The convective modes are either linearly saturated close to threshold or by ponderomotively driven ion-acoustic turbulence once threshold is exceeded significantly. It was noted that several tens of picoseconds are required for the LW spectrum to approach a statistical steady state.

Hot-electron production was first calculated by a non-self-consistent test particle approach using the Zakharov predictions for the electric fields at saturation and with the assumption of thermal boundary conditions. An exponential hot-electron tail was observed once the absolute threshold was exceeded ($\eta > 1$), and the characteristic temperature of this tail increased from approximately $T_{\text{hot}} = 50$ keV for $\eta \approx 1.5$ to a value of $T_{\text{hot}} = 140$ keV when $\eta = 3$. These temperatures were shown to be reasonable based on estimates of the maximum-allowable energy gain over the interaction region, and they are also broadly consistent with experimental measurements and RPIC simulations.

It was noted that electron heating also depends on the global details of the implosion because of the long-range nature of the hot electrons and the possibility of reheating [as has been described in **Practical Implementation of Delay-Type Boundary Conditions on Test Particles** (p. 74)]. This effect has been captured by using a particular form of boundary condition on the test-particle trajectories. A prescription for such boundary conditions has been constructed and described. Adoption of these boundary conditions was shown to lead to an increase in the computed hot-electron temperature by a factor of $\sim 3\times$. It was noted that any attempt to model the hot-electron temperature or preheat in such targets must account for this physical effect.

The model allows for systematic refinement. Future plans in this regard include the inclusion of a propagating scattered transverse EM envelope at a frequency $\omega_0/2$ so that absolute Raman and high-frequency hybrid instability¹⁸ may be included. The test-particle method developed here, together with reduced particle-in-cell calculations,¹⁰ will be used to guide the development of a self-consistent quasilinear model of electron heating. This will require the inclusion of the delay-type boundary conditions and an investigation into the effects of density inhomogeneity. The delay-type boundary condition model can also be improved. In particular, a self-consistent model for the sheath potential will be developed, and the effect of angular scattering will also be taken into account when computing electron trajectories.

Finally, diagnostics such as preheat, half-harmonic emission, and bremsstrahlung spectra^{26,48} will be added to the model to facilitate comparison with experiment.

ACKNOWLEDGMENT

This work was supported by the U.S. Department of Energy Office of Inertial Confinement Fusion under Cooperative Agreement No. DE-FC52-08NA28302 and by the National Nuclear Security Agency through its High-Energy Density Laboratory Plasmas Grant No. DE-FG52-09NA29545.

REFERENCES

1. J. D. Lindl *et al.*, *Phys. Plasmas* **11**, 339 (2004).
2. S. P. Regan, N. B. Meezan, L. J. Suter, D. J. Strozzi, W. L. Kruer, D. Meeker, S. H. Glenzer, W. Seka, C. Stoeckl, V. Yu. Glebov, T. C. Sangster, D. D. Meyerhofer, R. L. McCrory, E. A. Williams, O. S. Jones, D. A. Callahan, M. D. Rosen, O. L. Landen, C. Sorce, and B. J. MacGowan, *Phys. Plasmas* **17**, 020703 (2010).
3. W. Seka, D. H. Edgell, J. F. Myatt, A. V. Maximov, R. W. Short, V. N. Goncharov, and H. A. Baldis, *Phys. Plasmas* **16**, 052701 (2009).
4. C. Stoeckl, R. E. Bahr, B. Yaakobi, W. Seka, S. P. Regan, R. S. Craxton, J. A. Delettrez, R. W. Short, J. Myatt, A. V. Maximov, and H. Baldis, *Phys. Rev. Lett.* **90**, 235002 (2003).

5. J. A. Delettrez, V. N. Goncharov, P. B. Radha, C. Stoeckl, A. V. Maximov, T. C. Sangster, J. A. Frenje, and D. Shvarts, *Bull. Am. Phys. Soc.* **52**, 143 (2007).
6. D. Shvarts, V. A. Smalyuk, R. Betti, J. A. Delettrez, D. H. Edgell, V. Yu. Glebov, V. N. Goncharov, R. L. McCrory, P. W. McKenty, D. D. Meyerhofer, F. J. Marshall, P. B. Radha, T. C. Sangster, W. Seka, S. Skupsky, C. Stoeckl, B. Yaakobi, J. A. Frenje, C. K. Li, R. D. Petrasso, and F. H. Séguin, presented at the 37th Anomalous Absorption Conference, Maui, HI, 27–31 August 2007.
7. V. A. Smalyuk, D. Shvarts, R. Betti, J. A. Delettrez, D. H. Edgell, V. Yu. Glebov, S. X. Hu, F. J. Marshall, R. L. McCrory, P. W. McKenty, D. D. Meyerhofer, P. B. Radha, T. C. Sangster, W. Seka, S. Skupsky, C. Stoeckl, B. Yaakobi, J. A. Frenje, C. K. Li, R. D. Petrasso, and F. H. Séguin, presented at the 37th Anomalous Absorption Conference, Maui, HI, 27–31 August 2007.
8. V. N. Goncharov, T. C. Sangster, P. B. Radha, R. Betti, T. R. Boehly, T. J. B. Collins, R. S. Craxton, J. A. Delettrez, R. Epstein, V. Yu. Glebov, S. X. Hu, I. V. Igumenshchev, J. P. Knauer, S. J. Loucks, J. A. Marozas, F. J. Marshall, R. L. McCrory, P. W. McKenty, D. D. Meyerhofer, S. P. Regan, W. Seka, S. Skupsky, V. A. Smalyuk, J. M. Soures, C. Stoeckl, D. Shvarts, J. A. Frenje, R. D. Petrasso, C. K. Li, F. Séguin, W. Manheimer, and D. G. Colombant, *Phys. Plasmas* **15**, 056310 (2008).
9. R. Yan, A. V. Maximov, C. Ren, and F. S. Tsung, *Phys. Rev. Lett.* **103**, 175002 (2009).
10. H. X. Vu, D. F. DuBois, D. A. Russell, and J. F. Myatt, *Phys. Plasmas* **17**, 072701 (2010).
11. D. A. Russell, presented at the Workshop on Laser Plasma Instabilities, sponsored by Lawrence Livermore National Laboratory and the University of Rochester's Laboratory for Laser Energetics, Livermore, CA, 3–5 April 2002.
12. Y. C. Lee and P. K. Kaw, *Phys. Rev. Lett.* **32**, 135 (1974).
13. A. Simon, R. W. Short, E. A. Williams, and T. Dewandre, *Phys. Fluids* **26**, 3107 (1983).
14. L. V. Powers and R. L. Berger, *Phys. Fluids* **27**, 242 (1984).
15. L. V. Powers and R. L. Berger, *Phys. Fluids* **28**, 2419 (1985).
16. L. V. Powers and R. L. Berger, *Plasma Phys. Control. Fusion* **28**, 1575 (1986).
17. B. K. Sinha and G. P. Gupta, *Plasma Phys. Control. Fusion* **35**, 281 (1993).
18. B. B. Afeyan and E. A. Williams, *Phys. Rev. Lett.* **75**, 4218 (1995).
19. B. B. Afeyan and E. A. Williams, *Phys. Plasmas* **4**, 3845 (1997).
20. A. C. Machacek and J. S. Wark, *Phys. Plasmas* **8**, 4357 (2001).
21. A. C. Machacek and J. S. Wark, *Phys. Plasmas* **8**, 704 (2001).
22. R. Yan, A. V. Maximov, and C. Ren, *Phys. Plasmas* **17**, 052701 (2010).
23. M. N. Rosenbluth, *Phys. Rev. Lett.* **29**, 565 (1972).
24. J. F. Drake and Y. C. Lee, *Phys. Rev. Lett.* **31**, 1197 (1973).
25. D. A. Russell and D. F. DuBois, *Phys. Rev. Lett.* **86**, 428 (2001).
26. D. F. DuBois, D. A. Russell, and H. A. Rose, *Phys. Rev. Lett.* **74**, 3983 (1995).
27. J. Delettrez, R. Epstein, M. C. Richardson, P. A. Jaanimagi, and B. L. Henke, *Phys. Rev. A* **36**, 3926 (1987).
28. D. F. DuBois and H. X. Vu, Los Alamos National Laboratory and University of California—San Diego, private communication (2010).
29. K. Y. Sanbonmatsu *et al.*, *Phys. Rev. Lett.* **82**, 932 (1999).
30. K. Y. Sanbonmatsu *et al.*, *Phys. Plasmas* **7**, 2824 (2000).
31. J. J. Thomson, R. J. Faehl, and W. L. Kruer, *Phys. Rev. Lett.* **31**, 918 (1973).
32. J. I. Katz *et al.*, *Phys. Fluids* **16**, 1519 (1973).
33. K. Y. Sanbonmatsu *et al.*, *Geophys. Res. Lett.* **24**, 807 (1997).
34. A. B. Langdon, B. F. Lasinski, and W. L. Kruer, *Phys. Rev. Lett.* **43**, 133 (1979).
35. C. Ren, University of Rochester, private communication (2010).
36. H. A. Baldis and C. J. Walsh, *Phys. Fluids* **26**, 1364 (1983).
37. R. W. Short, *Bull. Am. Phys. Soc.* **55**, 115 (2010).
38. H. X. Vu, D. F. DuBois, J. F. Myatt, and D. A. Russell, “Langmuir Waves Collapse and Associated Suprathermal Electron Production by the Two-Plasmon Decay Instability in Inhomogeneous Plasmas,” submitted to *Physical Review Letters*.
39. W. L. Kruer, *The Physics of Laser-Plasma Interactions, Frontiers in Physics*, Vol. 73, edited by D. Pines (Addison-Wesley, Redwood City, CA, 1988).
40. Y. Elskens and D. Escande, *Microscopic Dynamics of Plasmas and Chaos*, Series in Plasma Physics (Institute of Physics Publishing, Bristol, England, 2003).
41. W. Rozmus and P. P. Goldstein, *Phys. Rev. A* **38**, 5745 (1988).
42. R. D. Brooks and Z. A. Pietrzyk, *Phys. Fluids* **30**, 3600 (1987).
43. D. Pesme, *Phys. Scr.* **T50**, 7 (1994).
44. J. J. Thomson *et al.*, *Phys. Fluids* **17**, 973 (1974).
45. H. O. Wyckoff, *ICRU Report*, International Commission on Radiation Units and Measurements, Inc., Bethesda, MD (1984).
46. J. S. Pearlman and G. H. Dahlbacka, *Appl. Phys. Lett.* **31**, 414 (1977).
47. D. M. Villeneuve, R. L. Keck, B. B. Afeyan, W. Seka, and E. A. Williams, *Phys. Fluids* **27**, 721 (1984).
48. J. Meyer and Y. Zhu, *Phys. Rev. Lett.* **71**, 2915 (1993).

Fusion Yield Enhancement in Laser-Driven Magnetized Implosions

Plasma confinement and the suppression of energy transport are fundamental to achieving the high-energy-density conditions necessary for fusion applications. In the magnetic fusion energy concept,¹ this is accomplished by applying strong magnetic fields of the order of ~ 0.1 MG, such that the magnetic pressure exceeds the total plasma energy density, i.e., $\beta = 2\mu_0 p/B^2 \ll 1$, with p being the total plasma pressure. Following the formalism developed by Braginskii,² the electron heat transport is governed by the magnetization parameter $\omega_{ce}\tau_e$, where ω_{ce} is the electron gyrofrequency and τ_e is the electron collision time. Electron confinement and suppression of electron heat conduction are achieved for $\omega_{ce}\tau_e > 1$. Heat-flux suppression is also the basis of magnetized target fusion, where a preformed magnetized plasma is compressed via a cylindrical liner implosion.³

Magnetizing the hot spot in an inertial confinement fusion (ICF) implosion can reduce conductive energy transport. This increases the plasma temperature and allows for more fuel to be compressed at lower implosion velocities while still reaching ignition conditions, leading to an improved energy gain.⁴ To achieve $\omega_{ce}\tau_e \sim 1$ in the hot spot of a typical direct-drive deuterium–tritium (DT) ignition target,⁵ fields of the order of tens of megagauss are required. Confining α particles generated in the nuclear burn stage, to further reduce energy losses from the hot spot, necessitates fields as high as hundreds of megagauss.⁶ Such strong fields are challenging to generate. Magnetic-flux compression, in which an initially lower B field is embedded into a conductor and then compressed, has been shown to be a viable path to tens of megagauss via implosions driven with high explosives and pulsed-power sources.⁷

Recently, laser-driven magnetic-flux compression has been demonstrated under ICF-relevant conditions, with an amplification factor (final field divided by seed field) of $\sim 10^3$, significantly exceeding that of “conventional” compression methods.^{6,8} In an ICF target, the shell does not, by itself, trap the enclosed magnetic flux. Instead, upon laser irradiation of the target, the ablation pressure drives a shock wave through the shell, which breaks out into the gas fill inside, therefore raising the gas temperature and fully ionizing it. The gas becomes a

conductor and traps the magnetic field. Provided that the field diffusion time is longer than the compression time scale, the laser-driven capsule compresses the embedded magnetic flux. For conditions relevant to ICF implosions, the diffusion time has been estimated to be ~ 200 ns, while the implosion time is ~ 4 ns, providing an efficient trapping of the magnetic field.⁸ Through simple flux conservation arguments, and taking into account that the diffusion of flux into the plasma shell is a result of the finite hot-spot resistivity, the compressed field strength can be expressed as $B_{\max} = B_0(R_0/R)^{2(1-1/R_m)}$. Here R is the hot-spot radius, $R_m \sim 50$ is the time-averaged magnetic Reynolds number, and B_0 and R_0 are the initial seed field and gas-fill radius, respectively.⁸

In previous laser-driven flux compression experiments using the OMEGA laser,⁹ a seed magnetic field of 50 kG was trapped and compressed to more than 30 MG in a cylindrical capsule filled with D_2 gas.^{6,8} Despite the hot-spot electrons being magnetized under these conditions, no evidence of fusion performance enhancement was observed compared to nonmagnetized implosions. In cylindrical implosions, the hot-spot density increases as $\rho \propto 1/R^2$ (as opposed to $1/R^3$ in spherical implosions), which limits the achievable plasma densities. Consequently, the hot ions most likely to undergo fusion reactions have a mean free path comparable to the hot-spot radius and undergo only a few collisions before leaving the hot spot. Additionally, large shot-to-shot fluctuations caused by target parameter variations (gas pressure, alignment) precluded an accurate assessment of the B-field effects on the target performance.^{6,8}

This article presents experimental results using spherical, magnetized targets that provide a higher hot-spot density and significantly improved shot-to-shot reproducibility. The field compression scales roughly as $1/R^2$, irrespective of a spherical or cylindrical implosion. The experimental results discussed represent the first observation of an enhancement in the ICF performance as a direct result of hot-spot magnetization. Because of the open field-line configuration, the hot-spot thermal losses are suppressed by only $\sim 50\%$. Despite the modest

improvement in thermal energy confinement, the enhancements in fusion yields and ion temperatures are clearly detectable. Future experiments will explore closed field-line configurations that are expected to greatly reduce the heat losses.

Figure 126.26 shows the setup at the center of the OMEGA target chamber. To assess the impact of a magnetized hot spot on an ICF capsule performance, a spherical implosion target was positioned in the center of a single Cu coil. The coil was attached to the MIFEDS device (magnetized inertial fusion energy delivery system),¹⁰ used to drive a 45-kA current with an ~ 350 -ns half-period. It had an inner radius of 3 mm and generated a seed field perpendicular to the coil plane in the \hat{z} direction of $B_0 = 80 \pm 10$ kG across the capsule. This was timed to coincide with the OMEGA laser beams compressing the target. In contrast to previous experiments using a Helmholtz-like coil assembly, the single-coil setup provides stronger magnetic seed fields and minimizes coil interference with laser beam paths. The capsules were CH shells with an outer radius of $430 \mu\text{m}$ filled with 10 atm of D_2 gas. The CH wall thickness, an important parameter for assessing the fuel assembly's performance,¹¹ varied between 23.1 and $24.5 \mu\text{m}$. The coil was in the equatorial plane of the OMEGA target chamber, blocking 20 OMEGA laser beams from illuminating the target. The remaining 40 beams were repointed using a platform developed for polar-drive (PD) applications.¹² This ensured a target implosion with a high degree of spherical symmetry, even with a nonspherical irradiation pattern.¹³ The target was

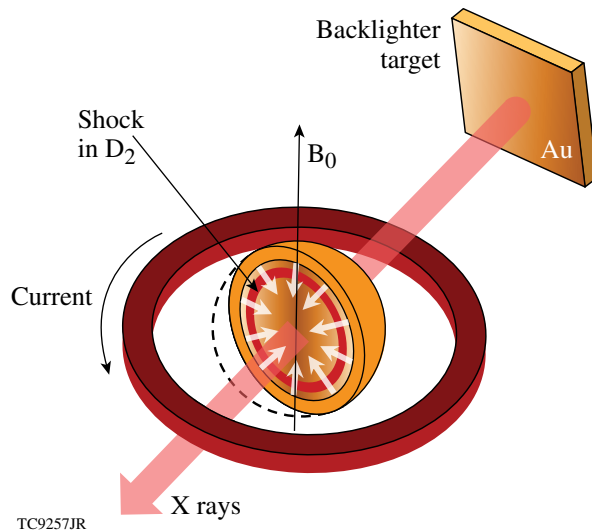


Figure 126.26

A spherical ICF target is placed inside a coil generating an 80-kG magnetic field. The target is imploded by the OMEGA laser, trapping and compressing the field inside. X-ray radiography is used to assess the implosion uniformity.

illuminated with 1-ns square laser pulses and a total on-target energy of 18 kJ with an average intensity of $\sim 7 \times 10^{14} \text{ W/cm}^2$. X-ray radiography assessed the implosion uniformity.¹⁴ The x rays were generated by illuminating a $25\text{-}\mu\text{m}$ Au foil mounted 5 mm away from the target at 52.6° off the equatorial plane (see Fig. 126.26) using four of the remaining OMEGA laser beams. The resulting x rays in the range of 2.5 to 4.5 keV were imaged onto a fast framing camera¹⁵ after passing through the imploding target. This technique has previously been applied successfully in polar-drive experiments, such as Ref. 13. To assess the target performance, the total neutron yield and the ion temperature were measured using a neutron time-of-flight (nTOF) diagnostic,¹⁶ situated 3 m from the target.

The 1-D hydrodynamic code *LILAC* was extended to solve the resistive magnetohydrodynamic (MHD) equations (*LILAC* MHD)^{17,18} to predict the compressed magnetic field and estimate its effect on the fuel assembly. Applying a 1-D simulation to the 3-D problem of a magnetic field in a spherically compressed target does not fully capture the nature of the experiment, and extending these calculations to the 3-D case will be the subject of future work. Nevertheless, it is possible to investigate characteristics of the B-field compression in a 1-D simulation by making the assumptions outlined below. The implosion can be treated as being spherically symmetric since the plasma pressure always exceeds the magnetic contribution ($\beta \gg 1$). Furthermore, the \hat{z} component of the B field was calculated at the target's equatorial plane via the induction equation and then extended over the entire target as a straight solenoidal field. The electron heat conduction is suppressed only perpendicular to the magnetic-field lines. In cylindrical geometry, this limitation was alleviated since the target length in the direction of the field significantly exceeded the target diameter, i.e., the field-normal heat loss suppression dominated the uninhibited lateral heat flow. In spherical geometry, the unmodified losses along the field lines must be included to treat the problem correctly. To do this, the total electron thermal conductivity κ_{tot} was treated as a superposition of the parallel and perpendicular contributions, κ_{\parallel} and κ_{\perp} , as $\kappa_{\text{tot}} = \kappa_{\parallel} A_{\parallel} / A_{\text{tot}} + \kappa_{\perp} A_{\perp} / A_{\text{tot}}$. A_{\parallel} and A_{\perp} are the parallel and perpendicular projections of the total hot-spot area A_{tot} . For a spherical hot spot, $A_{\parallel} / A_{\text{tot}} \approx 0.5$, such that even if all perpendicular heat losses are suppressed ($\kappa_{\perp} = 0$), the remaining total loss is reduced by 50% with respect to the unmagnetized case.

Simulation profiles for a spherical implosion using the experimental target and laser parameters and applying the approximations above are shown in Fig. 126.27. The compressed magnetic-field profile from a $B_0 = 80\text{-kG}$ seed field

(black), the ion temperature using the same seed (solid gray) and without an applied magnetic field (dashed gray) is shown. At this time, the hot-spot radius is $26 \mu\text{m}$ and the field has been amplified to $B_{\text{max}} \approx 80 \text{ MG}$, or a flux-averaged field across the hot spot of $B_{\text{avg}} = 15 \text{ MG}$. This compression is consistent with flux conservation and $R_m = 21$, with the theoretical limit in the case of no diffusion ($R_m \rightarrow \infty$) corresponding to a flux-averaged hot-spot field of $B_{\text{avg}} = 19.6 \text{ MG}$. The results in Fig. 126.27 are not at peak compression; therefore, the field is lower than the experimentally measured field in the cylindrical experiments.⁶ Based on these calculations, the expected experimental increase in ion temperature at the target center as a result of a magnetized hot spot is 8%, corresponding to a fusion yield enhancement of 13%. This calculated improvement of the target performance can be attributed solely to the magnetization of the hot spot and does not result from a change of the laser-coupling characteristics (e.g., via modification of the

heat transport at the ablation layer). This was confirmed by artificially removing any field effects in the simulation until after the laser had turned off. As expected, no discernable difference was observed compared to calculations with the B-field effects on for the full simulation interval. If the parallel heat losses are suppressed, e.g., by closing the magnetic-field lines, the simulations predict an increase of 42% in the ion temperature and a 73% neutron-yield enhancement. In this case, the target performance is primarily limited by radiative energy losses.

An experimental x-ray backlighter measurement is displayed in Fig. 126.28, showing an imploded target with and without an applied seed field and plotted using the same scale and color map. The MIFEDS coil was present around the target in both cases. The data were taken at $\sim 2 \text{ ns}$, a few 100 ps before peak compression. The bright area in the center is the location of the hot spot; the surrounding dark region results from x rays being absorbed in the dense shell and the coronal plasma. The center appears brighter than the background since the self-emission from the compressed core starts to become brighter than the backlighter emission at this time. The implosion is very uniform, despite using only 40 beams. This confirms the successful application of the PD platform to the magnetic-field compression experiments. No discernable difference is observed between the field and no-field cases, confirming that the magnetic field has no impact on implosion uniformity.

As shown in Ref. 11, the yield of an ICF implosion target decreases with increasing wall thickness. Figure 126.29 shows the measured neutron yield and ion temperatures from shots with an applied seed field of 80 kG (black dots) and without magnetic fields (blue squares) as a function of the target wall thickness. The magnetized target performance is visibly enhanced. To separate the effect of the magnetic field and the wall thickness on the neutron yield Y_n and the ion temperature

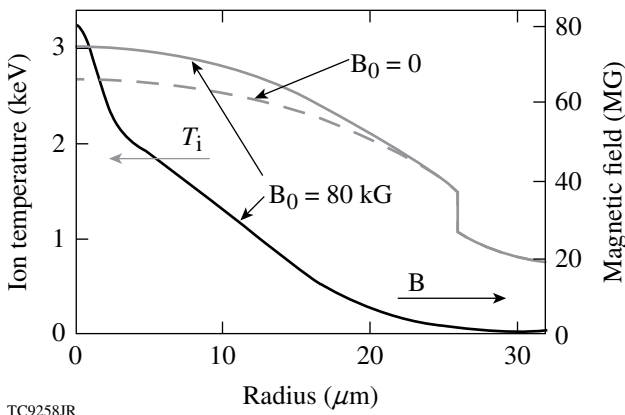


Figure 126.27
Compressed magnetic field (solid black) and ion temperature (solid gray) inside a spherical, magnetized hot spot simulated using *LILAC* MHD. The ion temperature is enhanced compared to the $B_0 = 0$ case (dashed gray).

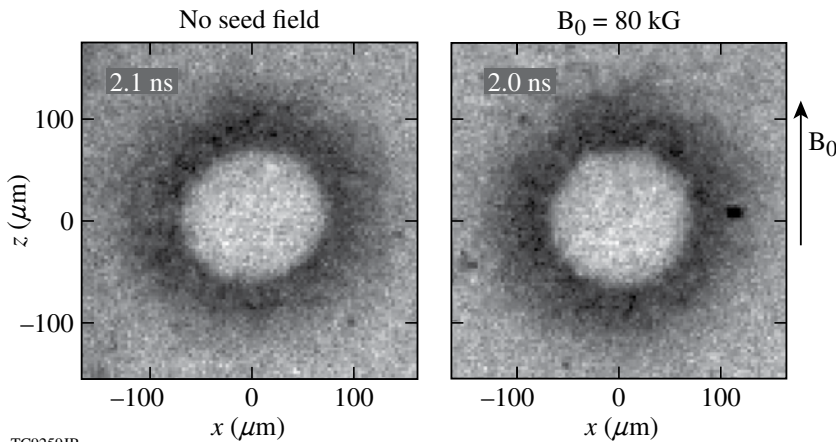
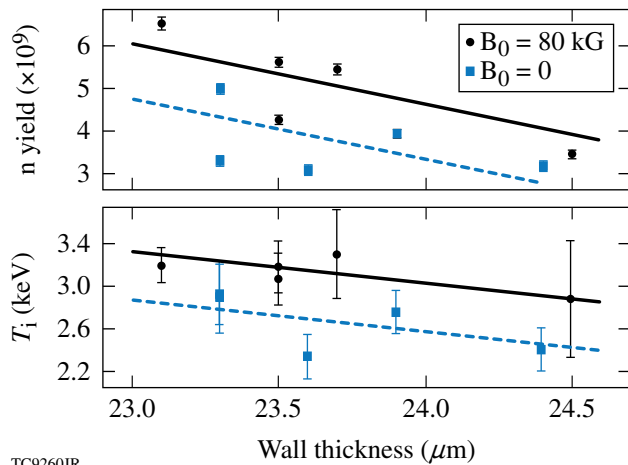


Figure 126.28
X-ray backlighter data show no impact by the magnetic seed field on the implosion uniformity.

T_i , a multiple linear regression method expressing these quantities as $Y_n = Y_{n0} + A_B B_0 + A_\Delta \Delta$ and $T_i = T_{i0} + C_B B_0 + C_\Delta \Delta$ is used. B_0 is the seed field (0 or 80 kG) and Δ denotes the shell thickness. A least squares fit to the data yields the fitting parameters listed in Table 126.V, giving the yield in units of 10^9 and the temperature in keV. The goodness of the fit is assessed through an F test that equates to a degree of confidence in the model of better than 94%. The result of the linear regression method is plotted as the lines in Fig. 126.29, showing a clear enhancement of both the neutron yield and the ion temperature. For shots where the magnetic seed field was applied, the yield was enhanced by 30% and the ion temperature by 15%. The overall scatter of data points for measurements with a magnetic field appears to be reduced compared to the no-field measurements. The data shown in Fig. 126.29 represent the first measurement of a fusion performance enhancement, resulting from embedding a strong magnetic field into an ICF capsule.

In previous experiments the compressed magnetic field was determined via proton deflectometry.^{6,8} The single coil

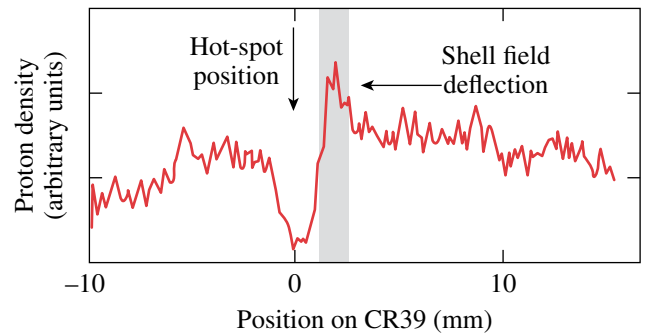


TC9260JR
Figure 126.29
Experimental neutron yield and ion temperature plotted against target wall thickness. A clear enhancement of the magnetized implosions (black dots) compared to the $B_0 = 0$ case (blue squares) is observed. The lines are fits to the data using the parameters listed in Table 126.V.

Table 126.V: Multiple linear regression coefficients for the fits to the experimental data in Fig. 126.29.

| | Y_{n0} | $A_B (10^{-5}/G)$ | $A_\Delta (1/\mu m)$ |
|---------------------|----------|-------------------|----------------------|
| | T_{i0} | $C_B (10^{-6}/G)$ | $C_\Delta (1/\mu m)$ |
| $Y_n (\times 10^9)$ | 37.6 | 1.7 ± 0.6 | -1.4 ± 0.6 |
| T_i (keV) | 8.57 | 4.8 ± 1.3 | -0.25 ± 0.11 |

used here blocked the line of sight through the target perpendicular to the field, preventing the use of a proton probe. To confirm the flux amplification in spherical implosions, the single coil was exchanged with a Helmholtz coil, as used in Ref. 6, while a glass sphere filled with D^3He gas and imploded using 12 OMEGA beams was used as an ~ 15.2 -MeV proton source. The protons traversing the target were deflected by the magnetic field and recorded on a CR39 track detector with the deflection pattern giving information about field topology and magnitude. This has been shown to result in a characteristic two-peak structure.^{6,8} Protons traversing the compressed hot-spot field (~ 30 MG) provided a strongly deflected peak, while protons propagating through the target wall experienced a lower field (~ 1 MG) and were weakly deflected but produced a higher-amplitude peak. Given the hot-spot size, the number of protons interacting with a spherical hot spot was lower than in the cylindrical case, thus decreasing the signal-to-noise ratio. Indeed, so far it has been impossible to obtain an unambiguous spherical hot-spot field measurement by observing a strongly deflected peak. Figure 126.30 shows a proton density lineout across a CR39 detector for ~ 14.8 -MeV protons that have slowed down in the dense shell. A strong peak is visible to the right of the hot spot (positioned at zero) caused by deflection in the target shell. While this does not provide the hot-spot field amplitude as discussed above, it is a signature of the magnetic field being trapped and amplified in the target and confirms the presence of a strong magnetic field inside the capsule.



TC9261JR
Figure 126.30
The cross-core proton deflectometry lineout exhibits a one-sided peak from protons traversing the magnetized target shell—a signature of a compressed B field inside the capsule.

In summary, a seed magnetic field of about 80-kG strength was embedded into spherical ICF targets imploded by the OMEGA laser in a PD beam-pointing geometry. As a result of the high implosion velocities and ionization of the target gas fill, the magnetic field inside the capsule was trapped and amplified through magnetic-flux compression, with simula-

tions indicating a flux-averaged hot-spot field of 15 MG at peak neutron yield. The implosion was confirmed to be spherically uniform by using x-ray radiography, showing no discernable difference in core symmetry with or without an applied seed field. At the strong magnetic fields reached in these experiments, the hot spot inside a spherical target becomes strongly magnetized, suppressing the heat losses by about 50% through electron confinement. As a result, the experimentally measured ion temperature and fusion yield were improved by 15% and 30%, respectively. This is in qualitative agreement with results from 1-D *LILAC*-MHD calculations, giving 8% and 13%, respectively. The difference can be attributed to the limited applicability of a 1-D code to the inherently 3-D problem of the magnetic field in a spherically compressed target. Extending these calculations to three dimensions will be the subject of future work. The data discussed here represent the first experimental verification of ICF target performance being enhanced by magnetizing the hot spot.

ACKNOWLEDGMENT

This work was supported by the U.S. Department of Energy Office of Inertial Confinement Fusion under Cooperative Agreement Nos. DE-FC02-04ER54789 and DE-FC52-08NA28302, the University of Rochester, and the New York State Energy Research and Development Authority. The support of DOE does not constitute an endorsement by DOE of the views expressed in this article.

REFERENCES

1. J. A. Wesson, *Tokamaks*, 3rd ed. (Clarendon Press, Oxford, 2004).
2. S. I. Braginskii, in *Reviews of Plasma Physics*, edited by Acad. M. A. Leontovich (Consultants Bureau, New York, 1965).
3. R. C. Kirkpatrick, I. R. Lindemuth, and M. S. Ward, *Fusion Technol.* **27**, 201 (1995).
4. R. Betti and C. Zhou, *Phys. Plasmas* **12**, 110702 (2005).
5. P. W. McKenty, V. N. Goncharov, R. P. J. Town, S. Skupsky, R. Betti, and R. L. McCrory, *Phys. Plasmas* **8**, 2315 (2001).
6. O. V. Gotchev, P. Y. Chang, J. P. Knauer, D. D. Meyerhofer, O. Polomarov, J. Frenje, C. K. Li, M. J.-E. Manuel, R. D. Petrasso, J. R. Rygg, F. H. Séguin, and R. Betti, *Phys. Rev. Lett.* **103**, 215004 (2009).
7. A. D. Sakharov, *Sov. Phys. Usp.* **9**, 294 (1966); F. S. Felber *et al.*, *Phys. Fluids* **31**, 2053 (1988).
8. J. P. Knauer, O. V. Gotchev, P. Y. Chang, D. D. Meyerhofer, O. Polomarov, R. Betti, J. A. Frenje, C. K. Li, M. J.-E. Manuel, R. D. Petrasso, J. R. Rygg, and F. H. Séguin, *Phys. Plasmas* **17**, 056318 (2010).
9. T. R. Boehly, D. L. Brown, R. S. Craxton, R. L. Keck, J. P. Knauer, J. H. Kelly, T. J. Kessler, S. A. Kumpan, S. J. Loucks, S. A. Letzring, F. J. Marshall, R. L. McCrory, S. F. B. Morse, W. Seka, J. M. Soures, and C. P. Verdon, *Opt. Commun.* **133**, 495 (1997).
10. O. V. Gotchev, J. P. Knauer, P. Y. Chang, N. W. Jang, M. J. Shoup III, D. D. Meyerhofer, and R. Betti, *Rev. Sci. Instrum.* **80**, 043504 (2009).
11. F. J. Marshall, J. A. Delettrez, V. Yu. Glebov, R. P. J. Town, B. Yaakobi, R. L. Kremens, and M. Cable, *Phys. Plasmas* **7**, 1006 (2000).
12. F. J. Marshall, R. S. Craxton, M. J. Bonino, R. Epstein, V. Yu. Glebov, D. Jacobs-Perkins, J. P. Knauer, J. A. Marozas, P. W. McKenty, S. G. Noyes, P. B. Radha, W. Seka, S. Skupsky, and V. A. Smalyuk, *J. Phys. IV France* **133**, 153 (2006).
13. F. J. Marshall, P. W. McKenty, J. A. Delettrez, R. Epstein, J. P. Knauer, V. A. Smalyuk, J. A. Frenje, C. K. Li, R. D. Petrasso, F. H. Séguin, and R. C. Mancini, *Phys. Rev. Lett.* **102**, 185004 (2009).
14. O. L. Landen *et al.*, *Rev. Sci. Instrum.* **72**, 627 (2001).
15. D. K. Bradley *et al.*, *Rev. Sci. Instrum.* **66**, 716 (1995).
16. R. A. Lerche, D. W. Phillion, and G. L. Tietbohl, *Rev. Sci. Instrum.* **66**, 933 (1995).
17. J. Delettrez, R. Epstein, M. C. Richardson, P. A. Jaanimagi, and B. L. Henke, *Phys. Rev. A* **36**, 3926 (1987).
18. N. W. Jang, R. Betti, J. P. Knauer, O. Gotchev, and D. D. Meyerhofer, *Bull. Am. Phys. Soc.* **51**, 144 (2006).

Amplifying Nanosecond Optical Pulses at 1053 nm with an All-Fiber Regenerative Amplifier

Fiber optical amplifiers based on rare-earth-doped fibers have been investigated because of their advantages, including inherent compactness and stability, broadband gain, and good beam quality. The energy gain of conventional fiber amplifiers for low-duty-cycle pulse sources is limited by their single-pass design since broadband amplified spontaneous emission (ASE) competes for the gain and degrades the signal-to-noise ratio (SNR). This limitation can be overcome by implementing regenerative amplification in an all-fiber system. With a gain fiber in a fiber cavity, optical pulses circulate inside the cavity and gain energy in many round-trips. All-fiber regenerative amplifiers (AFRA's) greatly improve the energy gain and SNR, while preserving the advantages of an all-fiber architecture. A ring-cavity, Q -switched fiber regenerative amplifier based on Er-doped fiber demonstrated a gain of more than 40 dB for 10-ns, 3-pJ pulses at 1530 nm (Ref. 1). Another Yb-doped fiber regenerative amplifier operating at 1030 nm amplified 40-ps, 9-pJ pulses to 55 nJ (Ref. 2).

An important potential AFRA application is to produce chirped optical pulses to seed chirped-pulse-amplification (CPA) systems. An approximately quadratic temporal-phase profile (a linear frequency chirp) is required for CPA seed pulses to be amplified and then compressed by grating-pulse compressors.³ The conventional approach to producing such seed pulses uses a mode-locked laser and a grating-pulse stretcher. This combination can be replaced by an AFRA with an electro-optic phase modulator (EOM) integrated inside the ring cavity.⁴ The required temporal phase can be imposed onto the optical pulse during many round-trips inside the cavity. Compared with the conventional approach, such an all-fiber CPA seed source can provide precise and flexible control over the phase profile, higher seed pulse energy to increase the SNR and temporal contrast of the CPA output, single-mode and alignment-free operation, and increased cost effectiveness.

This article reports on an AFRA based on Yb-doped fiber to amplify nanosecond, 1053-nm optical pulses with a repetition rate of 10.5 kHz. The pulses are amplified from 15 pJ to 240 nJ in five passes through the gain fiber. To the best of our

knowledge, this is the highest AFRA output-pulse energy ever reported. The wavelength of the AFRA is required by existing high-energy CPA systems based on Nd-phosphate laser glass.⁵ This wavelength is 23 nm off the gain peak of a Yb-doped fiber at 1030 nm, so ASE suppression techniques to favor the signal gain have been employed.⁶ Cavity build-up dynamics evident from leakage-pulse measurements and numerical modeling shows that the AFRA is not saturated in five round-trips and higher pulse energy can be extracted in more round-trips.⁷ This is limited, however, by the onset of bifurcation instability previously identified for solid-state regenerative amplifiers operating at high repetition rates.⁸ This limitation can be lifted by reducing the repetition rate from 10.5 kHz to below 0.5 kHz. Numerical simulations show that operating the AFRA at saturation not only increases the output level but also improves the output stability.

The experimental AFRA setup is shown in Fig. 126.31. The amplifier is seeded by 10-ns square pulses at 1053 nm. A fiber ring cavity is built with a section of polarization-maintaining (PM) Yb-doped fiber (3.5-m, 6- μ m core, 30 \pm 10 dB/m absorption at 980 nm) as the gain medium. The gain fiber is counter-pumped by a 500-mW continuous-wave diode laser at 976 nm (JDSU 29-7552-500) through a 976/1053-nm wavelength division multiplexer (WDM1). An additional 976/1053-nm WDM (WDM2) protects the pump diode against amplified optical signals at 1053 nm from the cavity. It provides 20-dB isolation over 1053 nm at the 976-nm port. A 2 \times 2 acousto-optic modulator (AOM) switch is used to switch the pulse in and out of the ring and to Q -switch the cavity. The two transmission states of the AOM switch, shown in the inset of Fig. 126.31, alternate the cavity between low- Q and high- Q phases. In the low- Q phase, lasing is suppressed and the gain fiber accumulates stored energy from pumping. The fiber cavity is essentially a single-pass system in this state. The cavity is switched to the high- Q phase after a seed pulse is injected, which gains energy in multiple passes through the gain fiber before being switched out at the end of this phase. A delay generator synchronized to the seed pulses controls the duration of the "on" state of the AOM and therefore the number of round-trips in the cavity. To

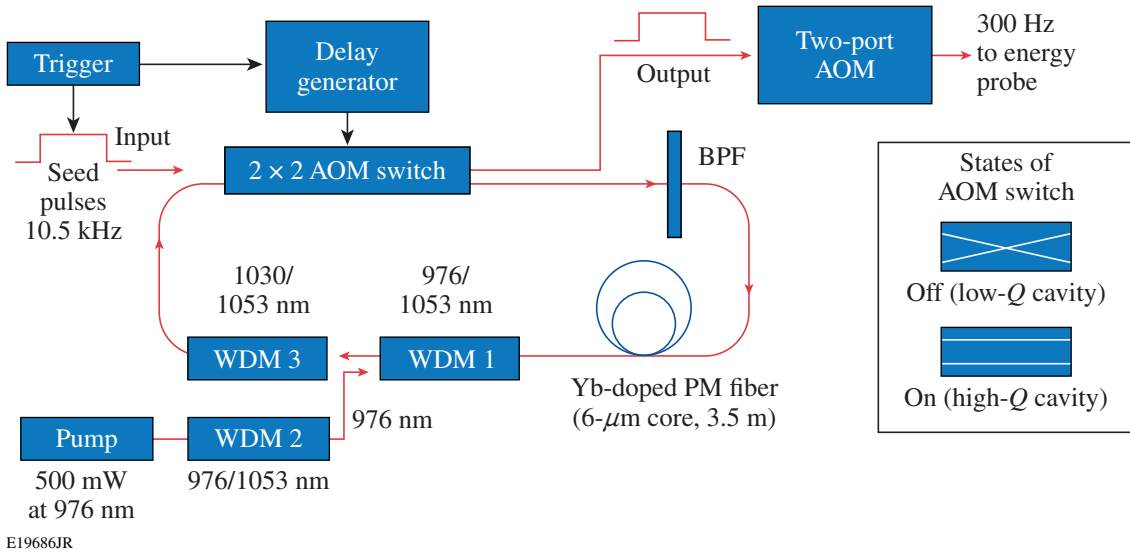


Figure 126.31

Experimental setup for the all-fiber regenerative amplifier (AFRA). In addition to the Yb-doped fiber as the gain medium, a 10-nm bandpass filter and a 1030/1053-nm WDM are built into the fiber cavity to suppress ASE and favor the signal gain. Optical pulses are switched in and out of the cavity by a 2×2 AOM switch. The two states of the switch are shown on the right.

favor the signal gain, a 1030/1053-nm WDM (WDM3) suppresses the 1030-nm gain peak, and a 10-nm bandpass filter (BPF) centered at 1055 nm further suppresses ASE at 1042 to 1046 nm. The output-pulse train's repetition rate is reduced to 300 Hz by a two-port AOM to enable one to directly measure the output-pulse energy with an energy probe limited to a maximum 2-kHz rate.

The effects of the ASE suppression techniques are shown in Fig. 126.32. The solid curve shows the spectrum of a 10-nJ

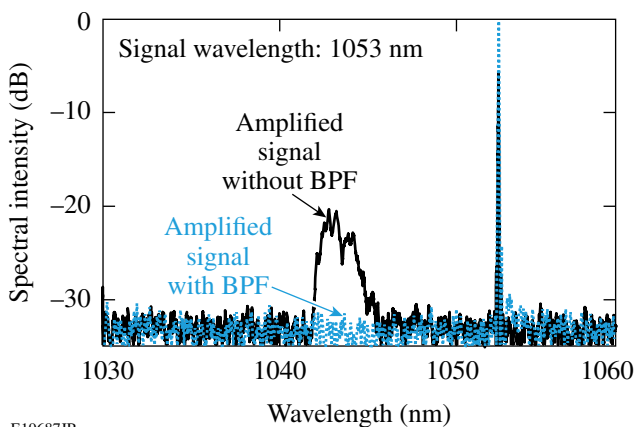


Figure 126.32

Spectra of 10-nJ output-pulse train from the fiber ring cavity without a BPF (dotted) and with a BPF (solid). The 1030-nm gain peak is suppressed by WDM3, and ASE at 1042 to 1046 nm is suppressed by the BPF.

output-pulse train without the bandpass filter in the cavity. WDM3 effectively suppresses ASE around 1030 nm, but ASE at 1042 to 1046 nm still develops. As the dotted curve shows, this ASE is completely suppressed by the bandpass filter. The bandpass filter also blocks any leakage pump beam from going back into the seed laser.

The 15-pJ seed pulses are amplified to 240 nJ in five round-trips in the cavity. Figure 126.33 shows the output-pulse energy and the total gain from five round-trips as the pump power is increased from 145 mW to 250 mW. The single-pass, small-signal gain of the Yb-doped fiber at pump levels up to 250 mW is plotted in the inset. Increasing the pump power beyond 250 mW does not increase the gain as the population inversion reaches maximum and additional pump is not absorbed, limiting the single-pass gain to about 18 dB and the total gain in five round-trips to 42 dB. At the highest output level, the pulse energy has a short-term (200 samples) fluctuation of 1.5% (rms) and a long-term drift of 6% (peak to valley).

Input and output pulses are measured using a 12-GHz photodiode (Discovery DSC50S) and single-shot oscilloscope (Tektronix DPO70604) to investigate the effect of the regenerative amplifier on the pulse shape. Normalized input and output waveforms are plotted in Fig. 126.34. The data are smoothed numerically to reduce instrumental noise. Compared to the input square pulse (solid), the output pulse (dashed) has a trailing edge 15% lower than the leading edge. This square-pulse

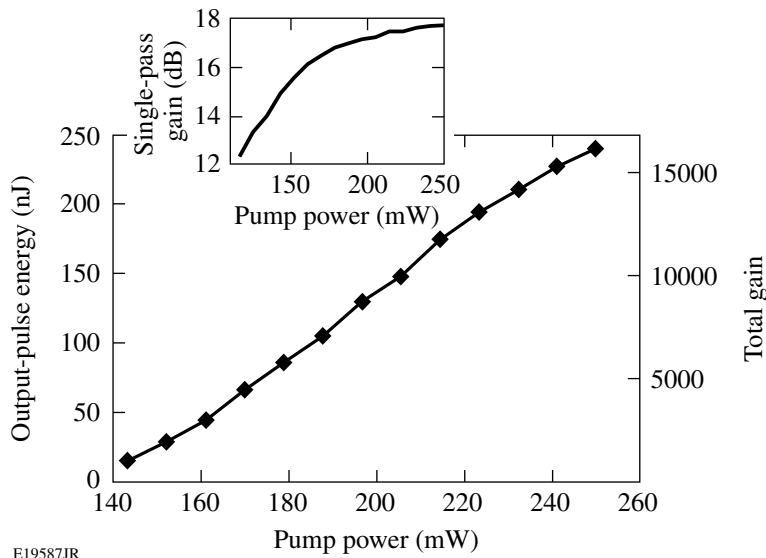


Figure 126.33
Measured pulse energy and total gain as pump power is increased. The pulse circulates in the ring cavity for five round-trips. Inset is the single-pass gain.

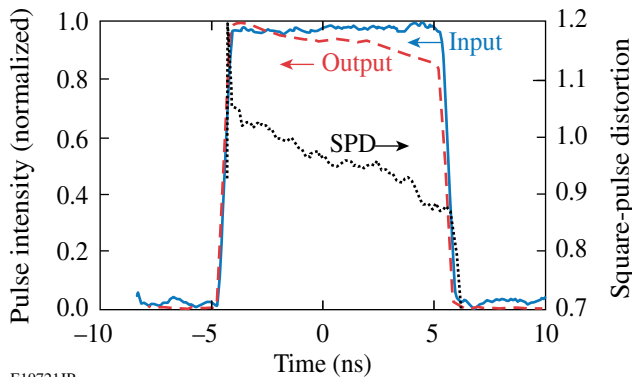
E19587JR

distortion (SPD), the ratio between the instantaneous intensities of the output pulse over the input pulse, originates from gain saturation of the regenerative amplifier and is also plotted (dotted) in Fig. 126.34.

Ideally for a regenerative amplifier, the pulse would circulate inside the cavity to accumulate energy until the stored energy is depleted and the gain is overcome by cavity loss (saturation). Maximum output-pulse energy is obtained when the pulse is ejected from the cavity at saturation. At the highest stable output level of the AFRA, the pulse energy increases exponentially (9 dB/RT) before cavity dump, which indicates that the amplifier does not saturate in five round-trips. This is further proved by numerical modeling.⁷ The laser pulse

amplification and population inversion in the gain medium are governed by rate equations that can be integrated to yield recurrence relations. The pulse fluence (proportional to pulse energy) and single-pass gain in the regenerative amplifier can be calculated for each pass using these recurrence relations. The solid curve in Fig. 126.35(a) shows the growth in pulse energy and the dashed curve shows the gain for each pass, calculated with this model. The gain is hardly depleted in five round-trips, and the AFRA has the potential to produce much higher pulse energy in more round-trips.

Producing higher pulse energy in the AFRA by increasing the number of round-trips is limited by the onset of period-doubling instability, where the output-pulse energy switches between different values.⁸ When the stored energy in the gain medium fully recovers through pumping between successive seed pulses, each pulse experiences the same gain and the output-pulse energy is stable. This may not be the case when the repetition rate of the regenerative amplifier is high enough that the time separation between seed pulses (cycle period) is comparable with or shorter than the upper-state lifetime of the gain medium. As the number of round-trips is increased and more energy is extracted in the high-*Q* phase, the population inversion will not have an opportunity to fully recover in the following low-*Q* phase because of its short duration. This reduces the gain for the next pulse and results in a lower pulse energy, which, in turn, leaves a larger amount of stored energy in the gain fiber to produce higher output in the cycle after the next. With the AFRA operating at 10.5 kHz, the cycle period (~95 μs) is much shorter than the Yb upper-state lifetime (~840 μs) and period-doubling instability is observed.



E19721JR

Figure 126.34
Input-pulse (solid) and output-pulse (dashed) shape and SPD (dotted) of the fiber amplifier. The output pulse has a 15%-lower trailing edge because of gain saturation.

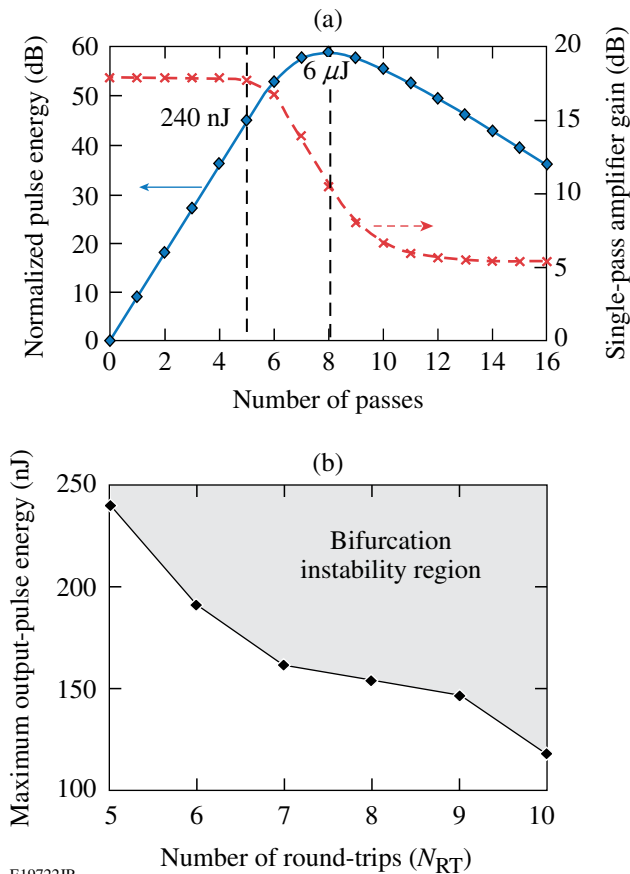


Figure 126.35

(a) Numerical simulation shows that the AFRA is not saturated after five round-trips and much higher pulse energy can be extracted from the amplifier in more round-trips. (b) The maximum stable output-pulse energy decreases when the number of round-trips is increased.

To avoid this, the pump level to the AFRA must be decreased as the number of round-trips increases. The maximum stable output-pulse energy decreases with more round-trips as shown in Fig. 126.35(b).

At repetition rates lower than 0.5 kHz, the cycle period will be long enough for the stored energy to fully recover.⁸ The pulse would circulate in the cavity for more round-trips and gain higher energy without causing period-doubling instability. Scaling the AFRA to higher pulse energies requires investigating detrimental nonlinear effects such as stimulated Brillouin scattering (SBS) and stimulated Raman scattering (SRS). For a 10-ns pulse, the estimated threshold pulse energy is 1.5 μJ for SBS⁹ and 5 μJ for SRS.¹⁰ With the single-pass gain reduced to

12.3 dB, the numerical model described above shows that the amplifier can produce 1.5- μJ pulse energy in 17 round-trips at saturation.

Operating the AFRA at saturation will not only increase the output level but also improve the output stability. As mentioned above, the AFRA output-pulse energy fluctuates because of variations in amplifier parameters like the single-pass small-signal gain (g_0) and loop transmission (T_0). The sensitivity of the output-pulse energy with respect to these parameters is determined by varying them in the numerical model described above. Figure 126.36 compares the output sensitivities of two operating points: five round-trips with a single-pass gain of 18 dB (unsaturated) and 18 round-trips with a single-pass gain of 12.3 dB (saturated). For the unsaturated case, the output fluctuation is 5 \times any variation of g_0 and T_0 . The output sensitivity is greatly reduced for the saturated case. Operating the amplifier for one round-trip after maximum pulse energy (reached in 17 round-trips) yields the best stability, with only 2% of energy penalty.

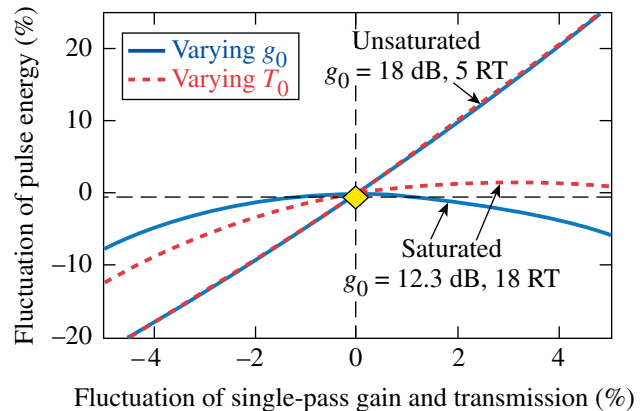


Figure 126.36

Variation of the amplifier output-pulse energy as small-signal gain (solid) and loop transmission (dashed) are varied. Comparing the output sensitivities of the saturated and unsaturated AFRA, it is found that operating the amplifier at saturation will greatly improve the output stability.

In conclusion, an all-fiber regenerative amplifier with Yb-doped fiber as the gain medium has been built. Nanosecond optical pulses at 1053 nm (23 nm off the gain peak of Yb-doped fiber) were amplified to as much as 240 nJ by the amplifier, achieving a total gain of 42 dB. The AFRA output level is limited by the onset of bifurcation instability previously iden-

tified for solid-state regenerative amplifiers operating at high repetition rates. Higher pulse energy may be expected from the AFRA at repetition rates lower than 0.5 kHz, limited by SBS. Sensitivity of the output-pulse energy with respect to amplifier parameters has been tested with numerical simulation, which suggests that operating the amplifier at saturation will greatly improve the output stability. The hundreds-of-nJ output-pulse energy makes the AFRA an attractive candidate as a CPA seed source (once a phase modulator is integrated into the cavity), compared to hundreds-of-pJ seed pulses commonly used in existing high-energy CPA systems.⁵

ACKNOWLEDGMENT

The authors are grateful for numerous conversations with and helpful support from J. R. Marciante, A. V. Okishev, and W. Bittle.

This work was supported by the U.S. Department of Energy Office of Inertial Confinement Fusion under Cooperative Agreement No. DE-FC52-08NA28302, the University of Rochester, and the New York State Energy Research and Development Authority. The support of DOE does not constitute an endorsement by DOE of the views expressed in this article.

REFERENCES

1. A. Yang, *Jpn. J. Appl. Phys.* **45**, L673 (2006).
2. S. Kanzelmeyer *et al.*, presented at Advanced Solid-State Photonics (ASSP), San Diego, CA, 31 January–3 February 2010 (Paper AWB15).
3. D. Strickland and G. Mourou, *Opt. Commun.* **56**, 219 (1985).
4. R. Xin and J. D. Zuegel, presented at Advanced Solid-State Photonics (ASSP), San Diego, CA, 31 January–3 February 2010 (Paper AMD3).
5. J. D. Zuegel, S. Borneis, C. Barty, B. LeGarrec, C. Danson, N. Miyanaga, P. K. Rambo, C. LeBlanc, T. J. Kessler, A. W. Schmid, L. J. Waxer, J. H. Kelly, B. Kruschwitz, R. Jungquist, E. Moses, J. Britten, I. Jovanovic, J. Dawson, and N. Blanchot, *Fusion Sci. Technol.* **49**, 453 (2006).
6. J. R. Marciante and J. D. Zuegel, *Appl. Opt.* **45**, 6798 (2006).
7. W. H. Lowdermilk and J. E. Murray, *J. Appl. Phys.* **51**, 2436 (1980).
8. J. Döring *et al.*, *Opt. Express* **12**, 1759 (2004).
9. H. Li and K. Ogusu, *Jpn. J. Appl. Phys.* **38**, 6309 (1999).
10. R. G. Smith, *Appl. Opt.* **11**, 2489 (1972).

Analysis and Suppression of Parasitic Processes in Noncollinear Optical Parametric Amplifiers

Introduction

Optical parametric amplifiers (OPA's) are widely used as sources of broadly tunable femtosecond pulses. Critically phase matched borate crystals, such as beta-barium borate (BBO), lithium borate (LBO), and bismuth borate (BiBO) have been employed to generate tunable ultrashort pulses from the visible to the near-infrared wavelength range.^{1–3} In particular, a noncollinear OPA (NOPA) allows for ultra-broad gain bandwidth that supports few-cycle pulse durations.^{4,5} Signal gain of 10^3 to 10^6 can be achieved within millimeter-long crystals as a result of perfect phase matching and large nonlinear coefficients. The lack of energy storage and low residual absorption in the crystals makes it possible to scale OPA's to several watts of average output power at pulse energies ranging from the sub- μJ level to $>100 \mu\text{J}$ (Refs. 6–8). Large-aperture crystals of deuterated potassium dihydrogen phosphate (DKDP) create the potential for ultra-intense optical parametric chirped-pulse-amplification (OPCPA) systems ($>10^{23} \text{ W/cm}^2$) using kilojoule Nd:glass lasers as pump sources.^{9,10}

Parasitic nonlinear processes can significantly degrade the performance of OPA's.^{2,11} For example, frequency doubling of one or more of the interacting waves can lead to spectral deformation and reduced efficiency. This article presents a detailed study of parasitic second-harmonic generation of signal and idler waves. The analysis focuses on critically phase matched NOPA's, but similar issues can occur in quasi-phase-matched materials.¹² Experimental observations are presented for two BBO-based NOPA systems. The first system is a MHz-rate NOPA that is seeded by white-light continuum generated in sapphire—a common choice for ultrafast time-dependent spectroscopy.¹³ The second system has been optimized for amplification of an ultra-broadband width ranging from 650 to 1050 nm to support few-cycle pulse durations. The experimental observations agree well with the results of a 2-D numerical model that was used to evaluate the influence of parasitic processes on the NOPA's overall efficiency.

To avoid unwanted parasitic processes, different crystals and noncollinear phase-matching configurations can be used. For

this purpose, calculations of the phase-matching properties for broadband BBO, LBO, BiBO, and DKDP NOPA's are presented. These results allow one to identify configurations that are free from phase-matched parasitic second-harmonic-generation (SHG) processes over the desired signal-wavelength range.

Noncollinear Phase-Matching Geometry

NOPA's achieve broadband gain by having a noncollinear angle α between the pump and signal to match the group velocity of the signal and idler.^{3,14} Figure 126.37 shows a common configuration for BBO, a crystal widely used for visible-wavelength NOPA's. The pump is extraordinary polarized (*e* wave) and its Poynting vector (S_p) and wave vector (k_p) are separated by an angle ρ . In BBO, the optimum α for the broadest gain is comparable to ρ . For example, $\rho = 3.3^\circ$ and $\alpha = 2.6^\circ$ when the wavelengths of the pump and signal are chosen to $\lambda_p = 523 \text{ nm}$ and $\lambda_s = 800 \text{ nm}$, respectively. Pump-signal birefringent walk-off is partially compensated by positioning the signal on the side to which the pump walks off, away from the crystal axis [see Fig. 126.37(b)]. In this case, the angle between the pump and signal Poynting vectors is $\rho - \alpha = 0.7^\circ$. The idler is angularly dispersed ($5 \times 10^{-3} \text{ deg/nm}$) and has an average angle relative to the signal of $\sim 7.4^\circ$.

Since the signal and idler are ordinary polarized (*o* waves), identical phase-matching conditions exist for any orientation of the signal *wave vector* around the pump wave vector, provided α is kept constant. This is shown in Fig. 126.37(a) as a circle around the pump wave vector. The largest pump-signal walk-off occurs when the angle between their Poynting vectors is $\rho + \alpha = 5.9^\circ$ [see Fig. 126.37(c)]. The two extremes are referred to as walk-off compensating (WC) and non-walk-off compensating (NWC), respectively.

Figure 126.38 shows the signal angles θ_s at which signal wavelengths are phase matched for a BBO NOPA pumped at 523 nm. Curves for several noncollinear angles α are shown (in red) for both the (a) WC and (b) NWC configurations. The NOPA phase matching has, to first order, the broadest bandwidth when the curves are horizontal,^{3,15} that is, a choice of

internal signal angle achieves perfect phase matching for the broadest range of signal wavelengths. Also shown (in blue) are the phase-matching curves for signal SHG. For the WC case, certain combinations of θ_S and α simultaneously phase match both the NOPA and signal SHG processes; therefore, parasitic SHG can occur.

Figure 126.39 shows a calculation of the phase-matching conditions for idler SHG. The internal angle of the idler wave to the crystal axis, θ_I , was calculated to compensate the pump

wave's vector component k_P , perpendicular to the signal wave vector k_S . Two values of α for both the WC and NWC configurations are shown (red curves). The phase-matching curves for idler SHG are shown in blue. In the WC configuration, phase matching is achieved at an idler wavelength of 1265 nm, and the angular deviations between the idler and the SHG phase-matching curve are small, in the wavelength range between 1100 nm and 1500 nm. In contrast, the NWC configuration avoids idler SHG since the phase-matched idler wavelengths (865 nm and 900 nm) are typically not present.

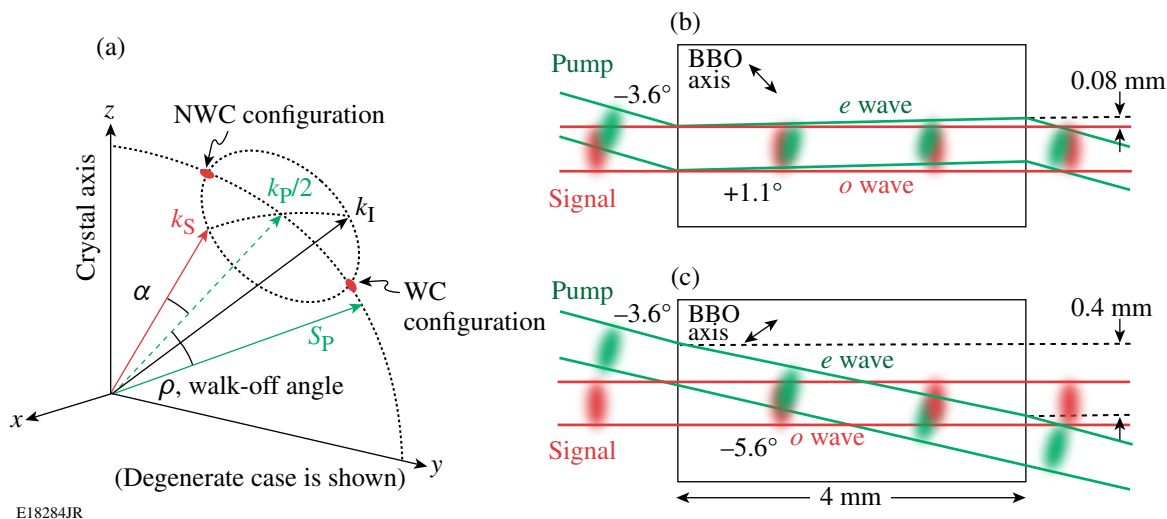


Figure 126.37

(a) Geometry for critical phase matching in a uniaxial crystal. The noncollinear angle between the pump and signal wave vectors is α . The walk-off angle between the pump Poynting vector (S_P) and signal wave vector is ρ . (b) Definition of the walk-off compensating (WC) configuration for negative uniaxial crystals. (c) Non-walk-off compensating (NWC) configuration. The idler wave vectors are angularly dispersed (not shown) and angles are exaggerated for clarity.

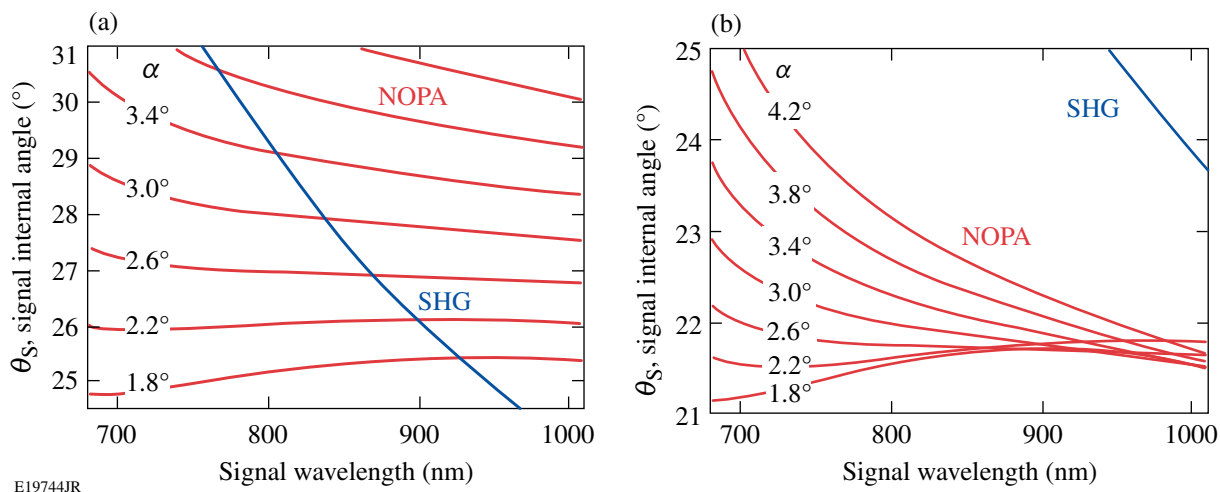
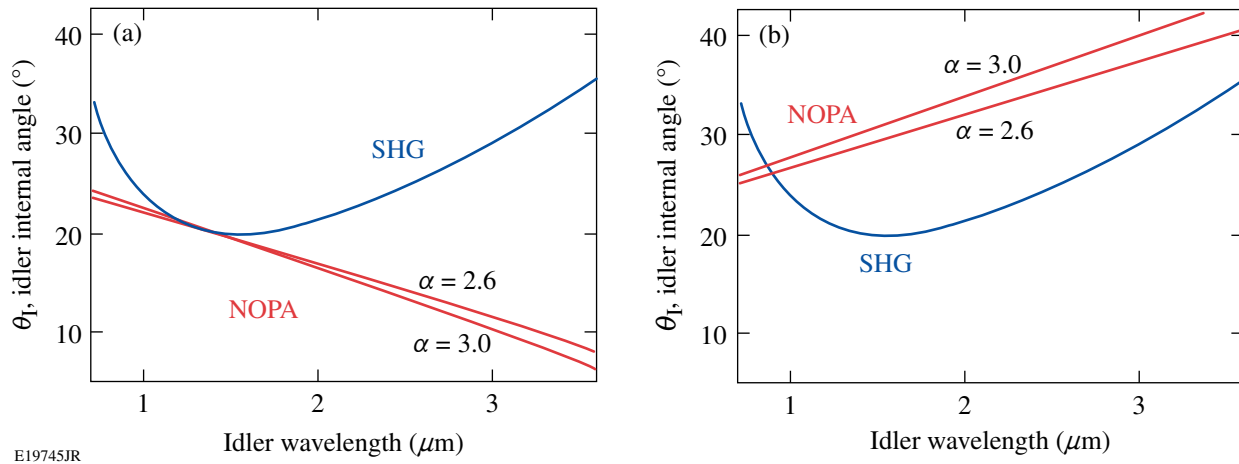


Figure 126.38

NOPA phase-matching curves (red) for BBO pumped at 523 nm for several noncollinear angles α : (a) the walk-off compensating (WC) and (b) the non-walk-off compensating (NWC) configurations. The phase-matching curves for signal SHG are shown in blue.



E19745JR

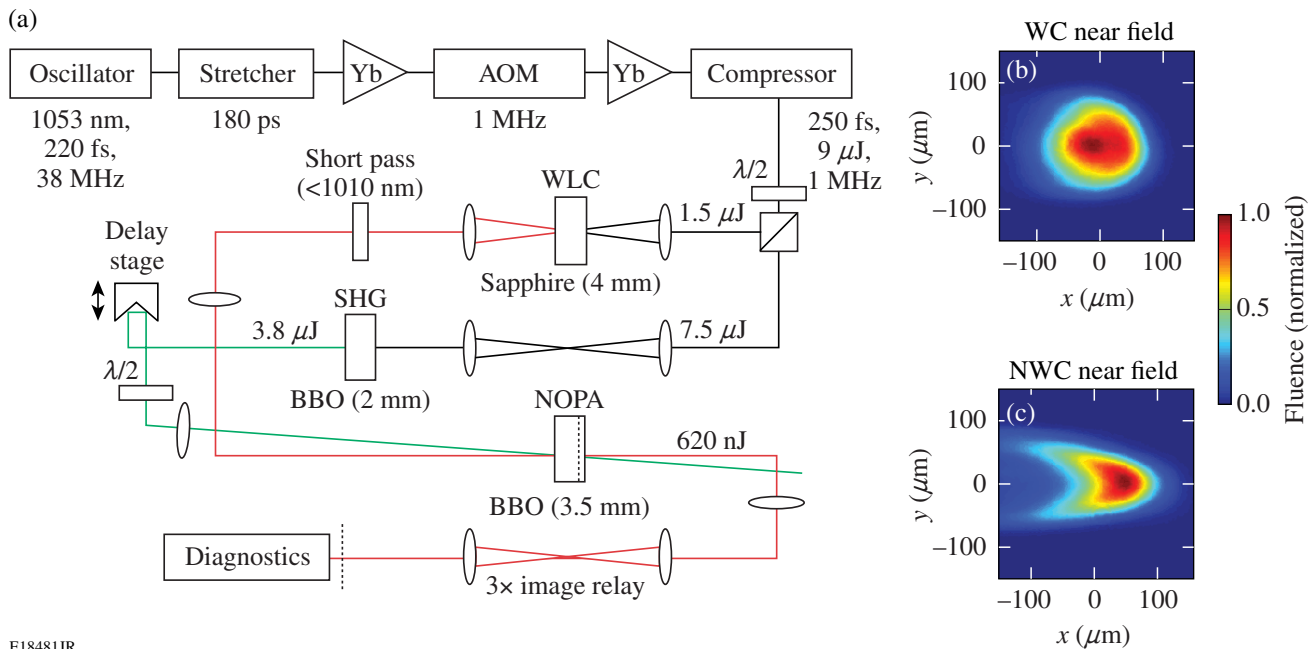
Figure 126.39

The idler wavelengths and internal angles for NOPA phase matching in BBO pumped at 523 nm for two values of α (in red): (a) the WC and (b) the NWC configurations. The phase-matching curves for idler SHG are shown in blue.

Experimental Observation of Parasitic Signal SHG

Parasitic processes were experimentally investigated using a BBO-based NOPA pumped at 1 MHz by a fiber chirped-pulse-amplifier (FCPA) system. A schematic of the system is shown in Fig. 126.40. Pulses from a mode-locked oscillator were stretched from 220 fs to 180 ps, down-selected from

38 MHz to 1 MHz, and amplified by a chain of four ytterbium-doped fiber amplifiers. A large-mode-area photonic-crystal fiber amplifier was used for the final stage, producing 12- μ J pulses centered at 1047 nm (Ref. 16). The compressor used two multilayer dielectric gratings (1740 lines/mm) to produce 9- μ J, 250-fs pulses. A portion of the energy (20%) was picked off and



E18481JR

Figure 126.40

(a) Experimental setup. Yb: ytterbium-doped fiber amplifiers; AOM: acousto-optic modulator; WLC: white-light continuum; SHG: second-harmonic generation; NOPA: noncollinear optical parametric amplifier. Near-field profiles of the amplified beams for (b) walk-off compensating (WC) and (c) non-walk-off compensating (NWC) configurations.

weakly focused into a static 4-mm sapphire plate to generate a chirped white-light continuum (WLC) seed.¹⁷ The rest was doubled in a 2-mm BBO crystal, producing 3.8- μ J pulses at 523 nm for pumping the NOPA.

The BBO crystal used in the NOPA was 4 mm long and was cut at an angle such that the seed beam was approximately perpendicular to the crystal face (27.1° and 21.6° for the WC and NWC geometries, respectively). The pump and seed were focused into the NOPA crystal with ~ 120 - μ m beam waists. The pump–signal walk-off lengths, defined as the distance required for a change in separation equal to their beam waists, were 8.2 mm for WC and 0.96 mm for NWC. The impact of pump–signal walk-off is clearly seen in the near-field beam profiles [Figs. 126.40(a) and 126.40(b)]. In the WC case, the near field is approximately Gaussian. In contrast, in the NWC case, there is a large asymmetry along the direction of walk-off (x - z plane). Despite this significant difference, the maximum signal power obtained for each configuration was roughly equal at ~ 850 nJ, when the seed delay and phase matching were optimized for 780 nm.

Amplified signal spectra for the two walk-off configurations are shown in Fig. 126.41. For the WC configuration, parasitic signal SHG was phase matched in the center of the gain band [Fig. 126.41(a)]. This resulted in a narrow spectral line at 412 nm (shown in blue), a large notch in the center of the signal spectrum at 824 nm, and smaller notches on either side at 788 nm and 865 nm. The side notches are due to non-degenerate sum–frequency generation: $(788 \text{ nm})^{-1} + (865 \text{ nm})^{-1} =$

$(412 \text{ nm})^{-1}$. No parasitic signal SHG was observed for the NWC configuration, and the signal spectrum had a smooth Gaussian-like shape [Fig. 126.41(b)].

Second-harmonic generation from the idler was also observed in the WC configuration. Figure 126.42 shows a measurement of its spectrum. Like the idler, which is angularly dispersed because of noncollinear phase matching, the idler second harmonic (SH) is angularly dispersed, producing a visible rainbow at the output of the amplifier that extends from

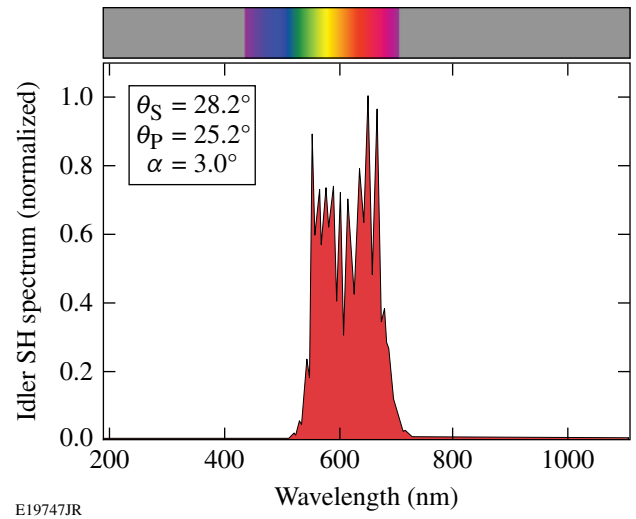


Figure 126.42
Spectra measured from idler SHG for the WC configuration. The spectrum spans much of the visible spectrum, as shown by the color bar above.

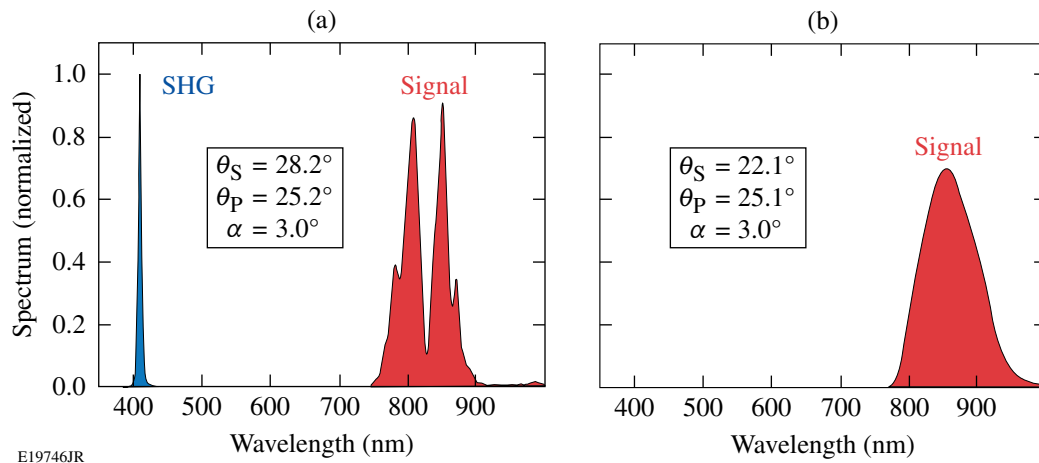


Figure 126.41
Signal spectra for (a) the WC and (b) the NWC configurations. The pump angle θ_p and noncollinear angle α were similar in both cases. In the WC configuration, the signal angle θ_s of 28.2° made it possible for parasitic second-harmonic generation to produce a narrow spectral line at 410 nm, leaving notches in the signal spectrum in the 780- to 870-nm range.

550 nm to 700 nm. This observation fits well to the phase-matching calculations shown in Fig. 126.39. A rough estimate of the idler SH energy is 0.1 to 0.4 nJ, which is less than 1% of the signal energy. Errors in this measurement result from calibration uncertainties for the broadband edge filter used to separate the idler and its second harmonic.

Numerical Model for Parasitic Signal and Idler SHG

The growth of parasitic signal and idler SHG was investigated using a 2-D numerical model. The equations of motion for the relevant optical fields were integrated using a split-step code that employed a fourth-order Runge–Kutta algorithm. The nonlinear propagation was modeled using Eqs. (1) for the field amplitudes in the time domain, $A_j(z, t)$, where $j = S, I, P, SSH$, and ISH for the signal, idler, pump, signal SH, and idler SH fields, respectively.

$$\begin{aligned} \frac{dA_S}{dz} &= i \frac{2\omega_S d_{\text{eff}}}{n_S c} (A_I^* A_P - A_S^* A_{SSH}), \\ \frac{dA_I}{dz} &= i \frac{2\omega_I d_{\text{eff}}}{n_I c} (A_S^* A_P - A_I^* A_{ISH}), \\ \frac{dA_P}{dz} &= i \frac{2\omega_P d_{\text{eff}}}{n_P c} A_S A_I, \\ \frac{dA_{SSH}}{dz} &= -i \frac{2\omega_{SSH} d_{\text{eff}}}{n_{SSH} c} A_S^2, \\ \frac{dA_{ISH}}{dz} &= -i \frac{2\omega_{ISH} d_{\text{eff}}}{n_{ISH} c} A_I^2. \end{aligned} \quad (1)$$

A constant nonlinear coefficient d_{eff} was assumed to be 2.16 pm/V (Ref. 18). Linear propagation effects such as dispersion and phase matching were included in the frequency domain using conjugate field amplitudes $a_j(z, \Omega)$, calculated from the time-domain amplitude using

$$a_j(z, \Omega) = \text{FFT}^{-1} [A_j(z, t), t \rightarrow \Omega]. \quad (2)$$

Ω is defined as the optical-frequency difference relative to the field's center frequency ω_j . The linear part of the split-step propagation, for step size h , was given by

$$a_j(z+h, \Omega) = a_j(z, \Omega) e^{in_j h(\omega_j + \Omega)/c - ih\Omega/v_S}, \quad (3)$$

where n_j is the frequency-dependent refractive index calculated using Sellmeier equations for BBO.¹⁹ The second term in the

exponent is added so that calculations are done in the frame of the signal pulse traveling with a group velocity v_S .

Figure 126.43 compares measured and simulated signal spectra for the WC configuration. Results are plotted for a range of signal angles θ_S . Similar features are seen in both, despite

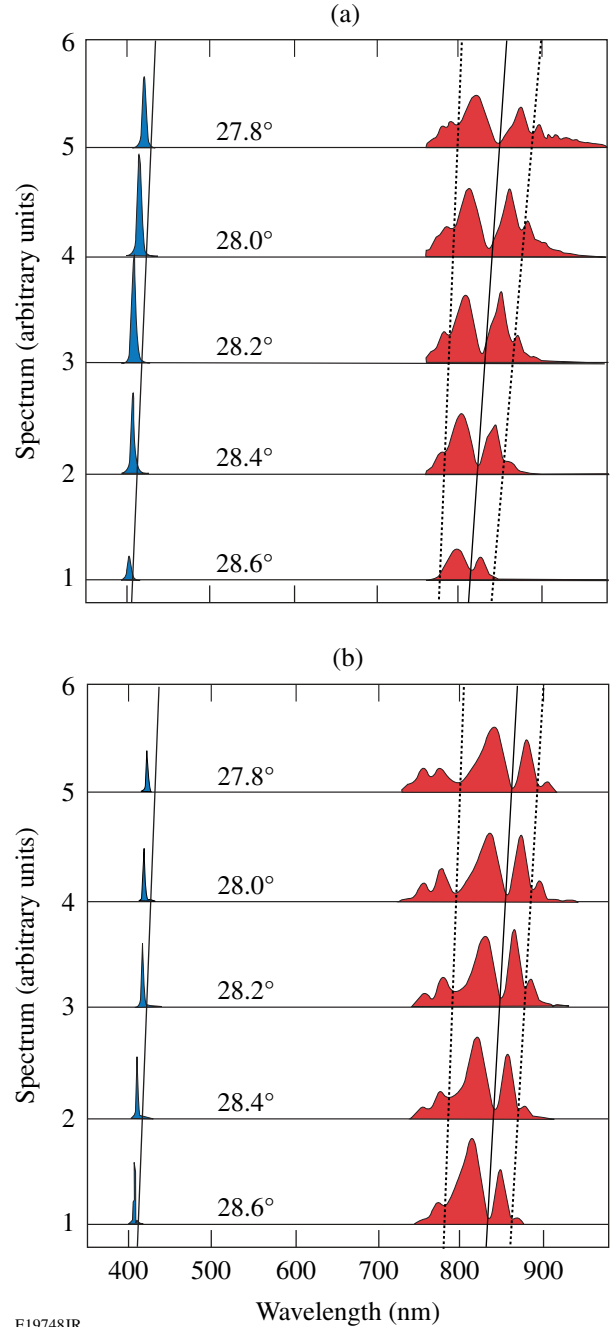


Figure 126.43

Comparison of (a) experimental measurements and (b) numerical simulations for a range of signal angles in the WC configuration.

the fact that the simulations use a simple 2-D model that does not include effects of spatial walk-off and intensity variation over the pump, signal, and idler beams. In both cases, notches are seen in the signal spectra corresponding to the generation of signal SHG, and the notches shift to longer signal wavelengths as the signal angle is reduced, consistent with the SHG phase-matching curves shown in Fig. 126.38. The calculated spectral features of parasitic signal SHG agree well with the experimental results.

Impact of Signal SHG on NOPA Efficiency

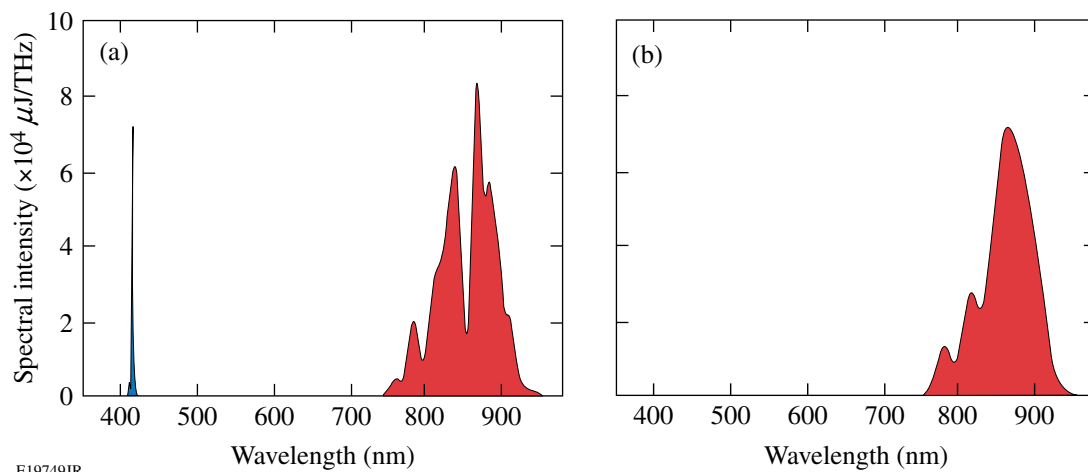
One benefit of an accurate model is the ability to evaluate the impact of parasitic processes by comparing results calculated either with or without the process. Furthermore, the axial evolution of each field within the crystal can be calculated to show the exchange of energy between the fields. The parameters shown in Table 126.VI were chosen for a case study of a BBO NOPA, corresponding approximately to the experimental configuration in Fig. 126.40.

Figure 126.44 shows amplified signal spectra for cases where the signal SHG was either included or suppressed in the model. The sharp notch and signal SH are evident in Fig. 126.44(a). Some spectral modulation is also seen in Fig. 126.44(b), even though SHG was suppressed in the simulation and the experimentally measured spectra were smooth [see Fig. 126.41(b)]. In this case the modulation is due to reconversion of the signal. The 2-D nature of the model, which considers only one value of peak temporal intensity for the pump and signal, means that averaging of reconversion effects over the Gaussian beam were not included and the spectral structure was not averaged away.

The impact of signal SHG on peak amplifier efficiency is shown in Fig. 126.45. Simulations predict that 10% of the signal pulse energy is lost to SHG at the optimum crystal length of 2.3 mm. In contrast, simulations of idler SHG show that a small *increase* in efficiency of a few percent can be expected when idler SHG is present. Similar effects have been observed in pulsed optical parametric oscillators (OPO's); absorption of

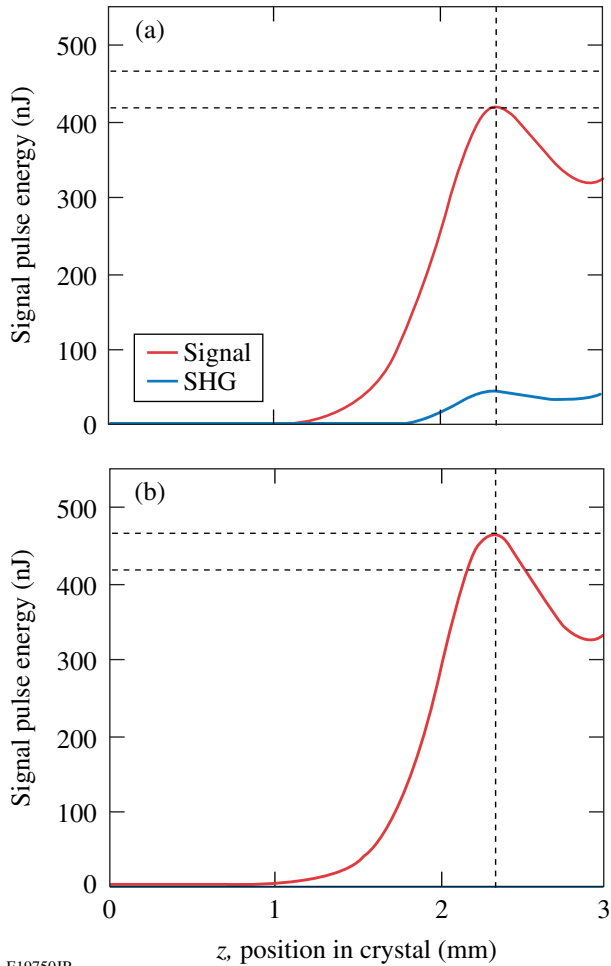
Table 126.VI: Input parameters for signal SHG case study.

| Parameter | Value | Parameter | Value |
|--|-------------|------------------------------------|---------------------|
| Noncollinear angle (α) | 3.1° | Signal spectral phase (ϕ_2) | 200 fs ² |
| Signal angle (θ_S) | 28.2° | Pump width (Gaussian) (τ) | 250 fs |
| Pump angle (θ_P) | 25.1° | Pump–signal delay at input | 75 fs |
| Signal center wavelength (λ_S) | 820 nm | Beam widths ($1/e^2$) | 120 μm |
| Pump wavelength (λ_P) | 523.5 nm | Signal input energy (E_S) | 0.1 nJ |
| Input signal bandwidth ($\Delta\lambda_S$) | 250 nm | Pump input energy (E_P) | 2 μJ |
| Order of Gaussian signal spectrum | Tenth order | BBO crystal length (l_C) | 3 mm |



E19749JR

Figure 126.44
Spectra for simulation case study. Signal SHG (a) turned on and (b) turned off in the model.



E19750JR

Figure 126.45

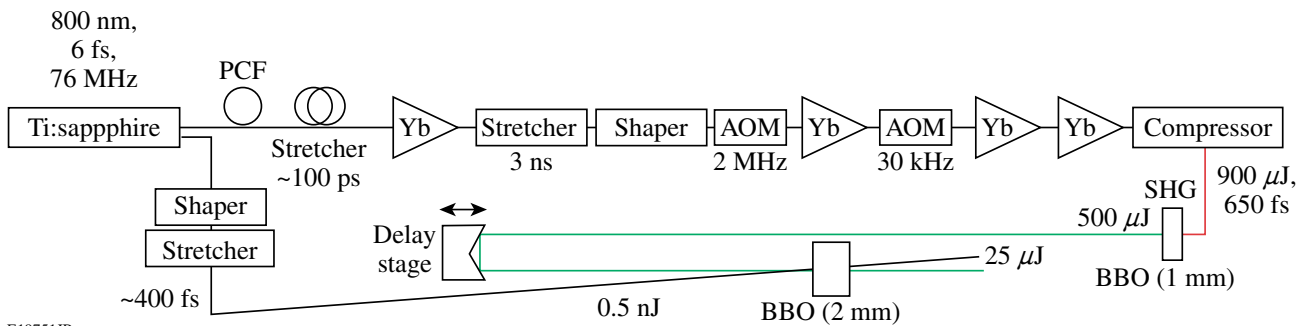
Simulated signal energy along the crystal, (a) with and (b) without signal SHG. In both cases signal reversion means that the length for optimum efficiency is 2.3 mm. When SHG is included in the simulations, 10% of the signal energy at this length is lost to the parasitic process.

the idler removes it from the three-wave interaction, increasing the threshold at which the signal is reconverted to the pump.²⁰

Parasitic Processes in Few-Cycle NOPA

NOPA's can support the extremely large optical bandwidth required by few-cycle pulses. Parasitic nonlinearities may occur over a significant wavelength range of the signal and idler. To investigate parasitic SHG effects over a larger spectral bandwidth, measurements with a few-cycle NOPA were performed. The experimental setup of the system is shown in Fig. 126.46 and is similar to the one presented in Refs. 5 and 7. A Ti:sapphire oscillator (Femtolasers Rainbow) delivering few-cycle pulses is used for seeding both the NOPA and a state-of-the-art FCPA system. The FCPA system delivers 900- μ J, 650-fs pump pulses that are frequency doubled in a 1-mm BBO crystal with an efficiency of 56%, resulting in 500- μ J pump pulses for the NOPA. Focusing to 100 GW/cm² provides a gain of 5×10^4 . The signal pulses traverse a pulse-shaping device and a prism stretcher before being imaged into the BBO crystal. The non-collinear angle is 2.5° to achieve broadband phase matching. This is slightly lower than the angle for group-velocity matching of signal and idler (2.6°). As a result, the phase matching is improved in the spectral wings, while a slight phase mismatch is generated in the center. This configuration leads to a larger effective gain bandwidth, therefore shorter pulses at the output of the system.¹⁵ Because of the high pump intensity, the 0.5-nJ oscillator pulses can be amplified to 25 μ J in a single stage in both the WC and NWC configurations.

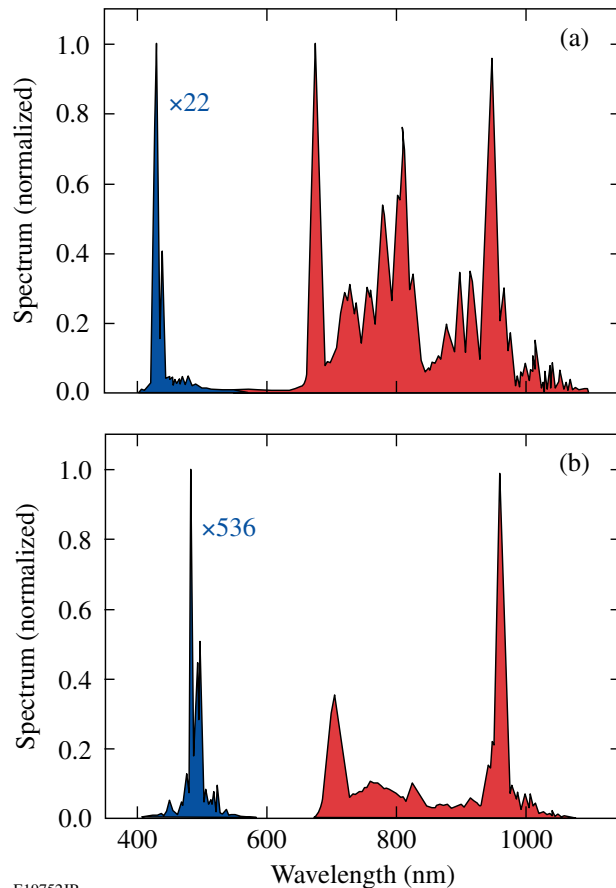
Quantitative measurements of the parasitic process were made using a bandpass filter (Newport BG.40) to separate the signal's fundamental and SH pulses. Their spectra for the WC and NWC configurations are shown in Figs. 126.47(a) and 126.47(b), respectively. The SH energy for the WC geometry measured after the filter is 1.1 μ J, corresponding to ~4% of the energy of the amplified signal. The measured spectra clearly show phase-matched SHG of 860-nm signal to 430 nm. This agrees with the phase-matching calculations for the NOPA configuration. The amplified signal spectrum shows modulation that may originate



E19751JR

Figure 126.46

A noncollinear OPCPA setup pumped by the second harmonic of a high-energy FCPA system.



E19752JR

Figure 126.47

Measured spectra for (a) the WC and (b) the NWC configurations containing the signal and its second harmonic. Note that both the fundamental and the second-harmonic spectra have been normalized to their peak value, independently.

not only from signal SHG, but also from sum-frequency generation (similar to the side notches shown in Fig. 126.41).

In contrast, the parasitic signal SHG is significantly reduced in the NWC configuration and the spectrum of the amplified

signal has less modulation. For the same amplified pulse energy, the signal SH power after the BG.40 filter is only 37 nJ, corresponding to $\sim 0.1\%$ of the amplified signal energy. Phase-matching calculations show that no signal wavelengths are perfectly phase matched in this configuration, resulting in inefficient signal SHG.

The idler SHG was also observed in the WC configuration and spanned from 550 nm to 750 nm. This is supported by the calculation of the phase-matching conditions shown in Fig. 126.39. As expected, no idler SHG was measured in the NWC configuration.

Parasitic Phase-Matching Curves for Other Common Nonlinear Crystals

Parasitic SHG processes are not limited to BBO-based NOPA's. The phase-matching curves for signal and idler SHG are shown in Fig. 126.48 for other common nonlinear crystals: LBO, BiBO, and DKDP. In all cases, the noncollinear angle was chosen for group-velocity matching of the signal and idler. The resulting signal angle within the crystal is plotted in dashed lines for both configurations, together with the corresponding SHG phase-matching curves, in Figs. 126.48(a), 126.48(c), and 126.48(e), respectively. The internal idler angles for idler SHG are plotted in Figs. 126.48(b), 126.48(d), and 126.48(f) (dashed lines). The SHG phase-matched signal and idler wavelengths for each crystal type and configuration are given in Table 126.VII.

The resulting idler wavelengths, which are phase matched for second-harmonic generation, and the corresponding signal wavelengths are displayed in Table 126.VII. The last row of Table 126.VII represents the usable parasitic SHG-free signal wavelength range around an 800-nm central wavelength. It has to be taken into account for the design of a broadband OPCPA system. In summary, the NWC configuration offers the largest parasitic-SHG-free bandwidth for all considered crystals. Furthermore, BBO in the NWC configuration seems

Table 126.VII: SHG phase-matched signal and idler wavelengths for BBO, LBO, BiBO, and DKDP in both WC and NWC configurations for NOPA's pumped by the second harmonic of Yb-based systems ($\lambda_p = 510$ to 525 nm). The corresponding signal wavelength for parasitic idler SHG is calculated from the energy conversion. The parasitic SHG free-wavelength range is summarized in the last row.

| Crystal material | BBO | | LBO | | BiBO | | DKDP | |
|---|------|-------|-----------|------------|-----------|-------|------|-------|
| | WC | NWC | WC | NWC | WC | NWC | WC | NWC |
| Signal SHG wavelength (nm) | 860 | 1119 | 963 | 1012 | 889 | 1025 | 942 | 1090 |
| Idler SHG wavelength (nm) | 1265 | 864 | 1031/1067 | 983/1794 | 1102/2338 | 969 | 1110 | 951 |
| Signal λ for idler SHG (nm) | 869 | 1275 | 1029/758 | 1082/722 | 966/660 | 1099 | 961 | 1123 |
| Parasitic SHG free λ range (nm) | <860 | <1119 | 758...963 | 722...1012 | 660...889 | <1025 | <942 | <1090 |

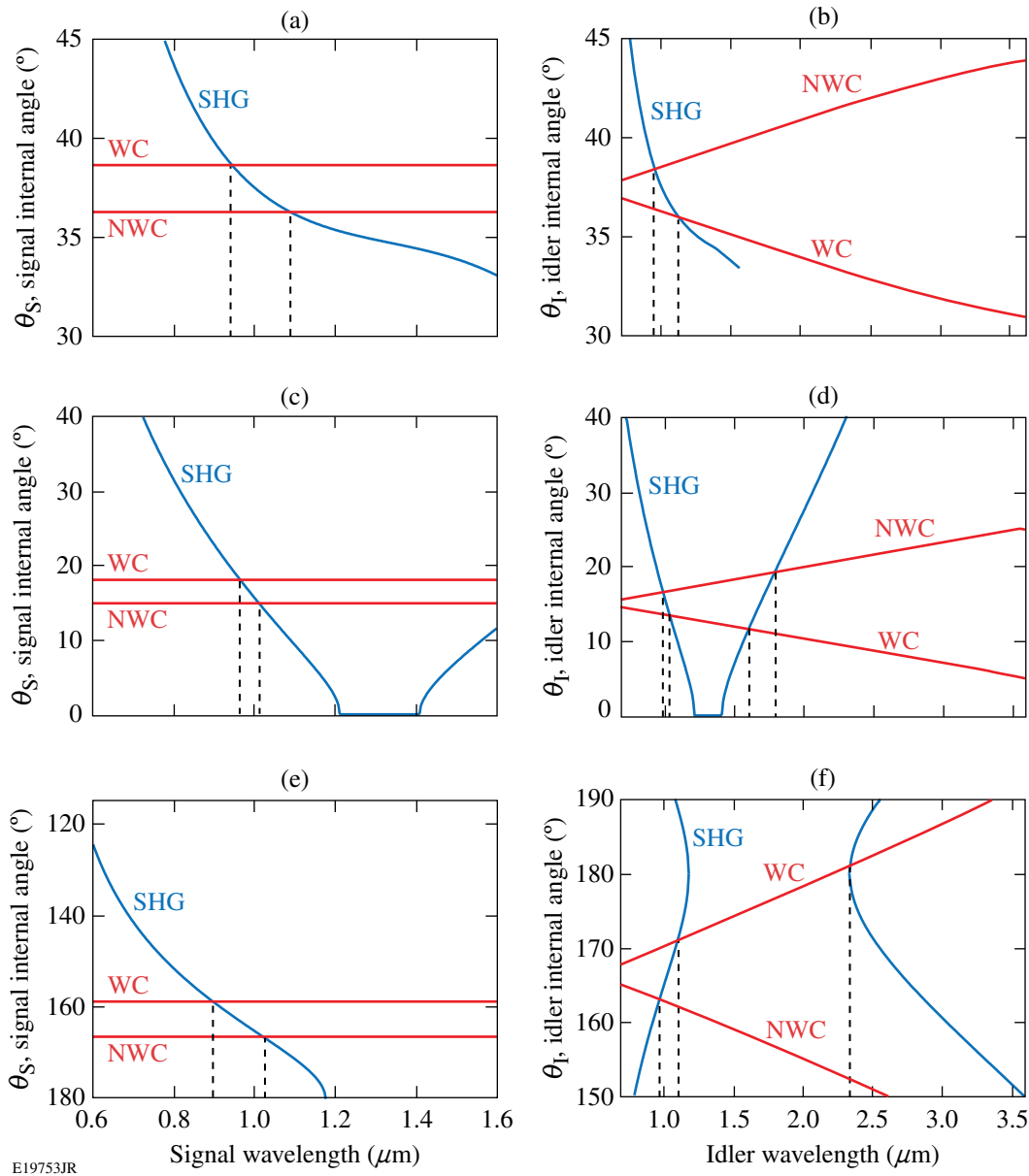


Figure 126.48

Phase-matching curves for signal (left column) and idler (right column) SHG for other common NOPA crystals: [(a),(b)] DKDP; [(c),(d)] LBO; and [(e),(f)] BiBO.

to be most suitable for ultra-broadband NOPA's since it is free of parasitic-SHG phase matching until 1129 nm. Deviations from the assumed noncollinear angles and pump wavelength will shift the SHG phase-matched wavelength slightly, although the general behavior remains the same.

Conclusions

A detailed analysis of parasitic nonlinear effects, namely second-harmonic generation of the signal and idler waves, on

broadband high-repetition-rate NOPA's has been presented. Results from an experimental study of a white-light-seeded NOPA agree well with 2-D numerical simulations. Modeling shows that second-harmonic generation of the signal can reduce the NOPA output energy by 10%.

A quantitative analysis was carried out for an ultra-broadband, few-cycle NOPA. For the WC configuration, a few percent of the output is converted into signal SH, while the

effect is reduced by at least an order of magnitude for the NWC configuration. Strong spectral modulation is observed in the WC configuration that originates from SHG and SFG of the spectral components of the signal and idler. Such modulation can significantly reduce the pulse quality of the output pulses and can be avoided by using the NWC configuration. A detailed phase-matching analysis for the most common nonlinear crystals is presented as a guide for designing NOPA systems.

The NOPA application dictates which configuration is best suited. For a laser front end, for example, a symmetric near-field profile and good spectral uniformity across the beam are required. In the case of low pump-pulse energy ($<10 \mu\text{J}$) and peak power ($\sim 10 \text{ MW}$), the WC geometry is the best choice, provided parasitic SHG can be avoided over the amplifier's wavelength range. For spectroscopic applications, where the bandwidth and tuning range of the signal are primary requirements, the NWC configuration is a better choice, provided that lower gain is acceptable or that the poor beam symmetry and spectral nonuniformity across the beam are tolerable. In the case of an ultra-broadband, few-cycle NOPA, the NWC configuration must be used to avoid power loss and spectral modulation on the ultra-broad spectrum. Distortions in the amplified beam can be avoided in this case by weakly focusing the high-peak-power pump laser.

ACKNOWLEDGMENT

This work has been supported by the U.S. Department of Energy Office of Inertial Confinement Fusion under Cooperative Agreement No. DE-FC52-08NA28302, the University of Rochester, and the New York State Energy Research and Development Authority. The support of DOE does not constitute an endorsement by DOE of the views expressed in this article.

This work was also supported by the German Federal Ministry of Education and Research (BMBF) with project 03ZIK455 "onCOOPtics," the Helmholtz Institute Jena, and the European Research Council under the European Union's Seventh Framework Programme (FP7/2007-2013)/ERC Grant agreement 240460. S. H. acknowledges financial support by the Carl Zeiss Stiftung Germany.

REFERENCES

1. C. Schriever *et al.*, *Opt. Lett.* **33**, 192 (2008).
2. J. Piel *et al.*, *Opt. Lett.* **31**, 1289 (2006).
3. G. Cerullo and S. De Silvestri, *Rev. Sci. Instrum.* **74**, 1 (2003).
4. A. Steinmann *et al.*, *Opt. Express* **14**, 10,627 (2006).
5. S. Hädrich *et al.*, *Opt. Lett.* **36**, 313 (2011).
6. J. Rothhardt *et al.*, *Opt. Express* **15**, 16,729 (2007).
7. J. Rothhardt *et al.*, *Opt. Express* **16**, 8981 (2008).
8. J. Rothhardt *et al.*, *Opt. Express* **18**, 12,719 (2010).
9. Y. Tang *et al.*, *Opt. Lett.* **33**, 2386 (2008).
10. V. V. Lozhkarev *et al.*, *Opt. Express* **14**, 446 (2006).
11. G. Arisholm *et al.*, *Opt. Express* **12**, 518 (2004).
12. J. Hellström *et al.*, *Opt. Lett.* **26**, 352 (2001).
13. E. Riedle *et al.*, *Appl. Phys. B* **71**, 457 (2000).
14. G. M. Gale *et al.*, *Opt. Lett.* **20**, 1562 (1995).
15. D. N. Schimpf *et al.*, *J. Opt. Soc. Am. B* **24**, 2837 (2007).
16. For more system details, see J. Bromage, J. M. Fini, C. Dorrer, and J. D. Zuegel, *Appl. Opt.* **50**, 2001 (2011).
17. R. R. Alfano, *The Supercontinuum Laser Source: Fundamentals with Updated References*, 2nd ed. (Springer, New York, 2006).
18. G. G. Gurzadian, V. G. Dmitriev, and D. N. Nikogosian, *Handbook of Nonlinear Optical Crystals*, 3rd rev. ed., Springer Series in Optical Sciences, Vol. 64 (Springer-Verlag, Berlin, 1999).
19. D. Eimerl *et al.*, *J. Appl. Phys.* **62**, 1968 (1987).
20. G. Rustad, O. Farsund, and G. Arisholm, presented at Advances in Optical Materials (AIOM), Istanbul, Turkey, 16–18 February 2011 (Paper AWA25).

Stress Compensation in Hafnia/Silica Optical Coatings by Inclusion of Alumina Layers

Introduction

Optical coatings are a critical technology for the successful construction and operation of high-peak-power laser systems. Optical coatings must provide appropriate spectral and photometric performance while maintaining high laser-damage resistance at the wavelength(s) and pulse duration(s) of interest. Additionally, the surface figure of the coated optics must be maintained to preserve the optical performance of the system. Thin-film stresses resulting from the optical coating process, both compressive and tensile, pose a risk to the performance and longevity of the coated components.

Electron-beam deposition of optical coatings has been the standard process for fabricating multilayer coatings for high-peak-power laser applications. The ability to scale the process to large substrates, flexibility in source materials and coating designs, and relatively low cost encourage the selection of this deposition process. Ultimately, however, the determination to date that such coatings produce the highest laser-damage thresholds has led to the use of electron-beam evaporation as the primary deposition process for large, high-peak-power laser components for systems such as OMEGA, OMEGA EP, the National Ignition Facility, Laser Megajoule, and others.

Multilayer coatings consisting of hafnium dioxide and silicon dioxide have been the standard choice for applications at both 1053 nm and 351 nm for these laser systems.¹⁻⁶ These materials provide good spectral and uniformity control while maintaining high laser-damage thresholds. Hafnia/silica multilayers, however, exhibit high tensile stresses, particularly on low-thermal-expansion substrates in low-relative-humidity environments, sufficient to provide significant substrate deformation and potentially cracking of the coated surface.^{2,7} Modification of the electron-beam deposition process for hafnia/silica coatings has been explored elsewhere, both through evaporation parameters and energetic assistance.⁷⁻⁹ In this work, the use of aluminum oxide is explored as a means of adjusting the stress in multilayer reflective coatings.

Aluminum oxide has a high bandgap with a corresponding high laser-damage resistance.^{10,11} Its relatively low refractive index makes it unattractive choice, however, for the high-index material in interference coating designs since such a refractive index leads to significantly thicker coatings with far greater numbers of layers. Alumina films deposited by electron-beam evaporation have been shown to exhibit tensile film stresses with a very slow diffusion of water, suggesting a relatively dense film structure without large, columnar pores in the coating.¹² The limited number of available coating materials with sufficiently high laser-damage resistance requires the exploration of all available choices. The diffusion behavior of alumina, coupled with its band gap and laser-damage resistance, suggests that further investigation of alumina performance could be beneficial to modifying the performance of hafnia/silica coatings.

Background

Tensile stresses pose significant challenges for implementation of optical components. First, any film stress leads to a deformation of the optic surface in accordance with the mechanical properties of the film and substrate, as described by Stoney's equation:¹³

$$\sigma = \frac{E_s t_s^2}{6(1 - \nu_s) t_f R}, \quad (1)$$

where σ is the film stress, R is the radius of curvature of the surface, E_s is Young's modulus of the substrate, ν_s is Poisson's ratio for the substrate, and t_f and t_s are the thickness of the film and substrate, respectively. This describes the impact of the stress on the radius of curvature of the optic surface, leading to changes in the flatness and corresponding optical performance of the component. While mechanically stiff substrate materials of sufficient thickness t_s will exhibit minimal bending from film stress, tensile stresses remain a problem if they lead to cracking, or crazing, of the coating.¹⁴

Fracture of a coating's surface results when tensile stresses exceed the fracture toughness of the film. Fracture will initiate at a defect in the coating, whether initiated by a scratch at the edge caused by coating tooling or optic mounting, or at a defect within the film such as shown in Fig. 126.49. Fracture also requires a sufficiently thick film in which the stress can be relieved through fracture at the surface, given the strain at that point. This relationship is given by Hutchinson and Suo:¹⁴

$$h_c = \frac{\Gamma E_f}{Z\sigma^2}, \quad (2)$$

where h_c is the critical coating thickness, Γ is the fracture resistance of the film, E_f is Young's modulus of the film, Z is a geometrical constant dependent on the fracture type (1.976 for film crazing), and σ is the tensile stress in the film. Compressive stresses will not lead to fracture of the coating surface; instead, excessive compressive stresses may lead to a buckling of the coating, potentially with delamination from the surface. This dependence on the thickness of the film relative to the film stress provides a means for understanding failure mechanisms in the coating.

Given the relationships in Eqs. (1) and (2), it is important to reduce the film stress such that optical performance of the component is preserved while fracture of the coating is avoided. Thicker substrates may aid in maintaining flatter optical surfaces and thinner coatings help to prevent cracking, but both of

these approaches result in a cost in substrate size and/or achievable coating performance. To provide optimal performance of the optical coating, the magnitude of the tensile film stress must be kept low or ideally moved to a compressive state. Compressive stress also must be kept low in order to maintain surface flatness of the optical component in accordance with Eq. (1).

Stresses in a multilayer coating are a function of the film thickness of each constituent material in the coating, as well as the stress in each material. Equation (1) may be modified to account for the individual stress in each layer by¹⁵

$$\sigma_1 t_1 + \sigma_2 t_2 + \dots + \sigma_n t_n = \frac{E_s t_s^2}{6(1-\nu_s)R}, \quad (3)$$

where σ_i and t_i are now the stress and thickness of each layer of the coating, respectively. Likewise, the total stress in the multilayer will be given by

$$\sigma_{\text{total}} = \frac{\sigma_1 t_1 + \sigma_2 t_2 + \dots + \sigma_n t_n}{\sum_i t_i} \quad (4)$$

since the individual stress contributions are simply weighted by the relative layer thicknesses of each. Modification of selected layers provides a means of adjusting the overall stress, with the use of three materials providing the ability to calculate the stress according to

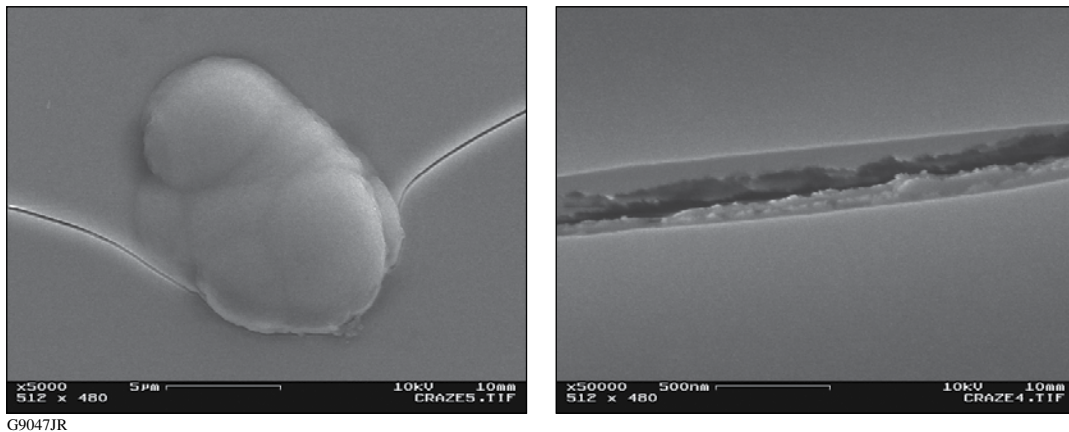


Figure 126.49

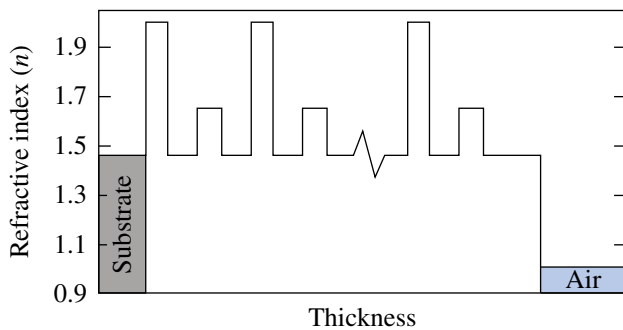
Scanning electron microscope imaging of the initiation site and crack that forms as a result of the high tensile stress in the film. A defect site in the coating provides an initiation site for tensile stress failure, while tearing of the film is evident within the crack that forms.

$$\sigma_{\text{total}} = \frac{\sigma_{\text{H}}T_{\text{H}} + \sigma_{\text{L}}T_{\text{L}} + \sigma_{\text{A}}T_{\text{A}}}{T_{\text{H}} + T_{\text{L}} + T_{\text{A}}}, \quad (5)$$

where T_i is now the total thickness of a given material in the entire multilayer since the stress is assumed to be constant for all layers of the same material deposited in the same manner. Subscripts H, L, and A denote hafnia (high refractive index), silica (low refractive index), and alumina, respectively. Given individual material stresses, coating designs may then be modified to yield the desired overall stress.

Experimental Procedure

Coating depositions were performed in a 54-in. coating chamber equipped with quartz heater lamps, dual electron-beam guns, and planetary substrate rotation. Granular silicon dioxide was evaporated from a continuously rotating pan while hafnium metal or aluminum oxide was deposited from a stationary six-pocket electron-beam gun. The baseline coating is a 32-layer hafnia/silica quarter-wave mirror centered at $\lambda_0 = 1053$ nm with a half-wave silica overcoat on fused-silica substrates. Alumina layers were substituted for selected hafnia layers, uniformly distributing the alumina layers throughout the coating. In addition, the first high-index layer on the incident side of the coating was always replaced by alumina to take advantage of its higher band gap in the region of highest electric-field intensity. In this manner, the coating has alumina/silica interfaces but no hafnia/alumina interfaces. The refractive-index profile of such a coating is shown in Fig. 126.50, with the outermost layers on the air side being a half-wave optical thickness of silica, with a quarter-wave optical thickness of alumina immediately beneath it.



G9050JR

Figure 126.50

Refractive index profile of a hafnia/silica/alumina high-reflector coating. Selected hafnia layers are replaced with alumina layers of equivalent optical thickness with the alumina layers being equally distributed throughout the overall thickness of the coating.

The primary means of altering the coating in this study was through the amount of alumina introduced in the coating design, relative to the overall thickness, as well as through the number of interfaces of each material. Depositions were performed with different overall coating thicknesses, relative numbers of layers and associated interfaces, and individual layer thicknesses. Deposition parameters such as oxygen backfill pressures, deposition rate, and substrate temperature remained constant throughout, in an effort to maintain a consistent film stress for each material between depositions.

Spectral measurements were performed on a Perkin-Elmer Lambda 900 spectrophotometer operating in transmission at normal incidence. The spectrophotometer environment was maintained at 0% relative humidity in order to eliminate optical thickness variations as a result of film water content. Photometric measurements were executed on a laser-based reflectometer system, again in a nitrogen-purged environment to achieve 0% relative humidity; measurements were performed at a constant wavelength while scanning the incident angle on the substrate. The measurement procedure incorporates a dual-beam configuration, using lock-in amplifiers and a chopped signal to minimize signal noise. Extended integration times at each point in the measurement scan further improve the quality of the measured result.

Surface flatness measurements of the 1-in.-diam substrates were performed on a Zygo New View white-light interferometer in a nitrogen-purged enclosure at approximately 0% relative humidity. Samples were purged for 15 h prior to measurement to stabilize the coating stress; measurement routines were automated to ensure consistent purge times. Samples measured after 6 h of purging exhibited irregular measurement results, with a significant decrease in correlation with deposition parameters. Measurements were corrected for cavity irregularity by referencing a $\lambda/50$ calibration flat, and all measurements subtracted the pre-coating flatness measurement of the individual substrate. Samples were supported on a three-point ball bearing mount, with each point positioned 120° apart at 65% of the radius of the substrate to minimize distortion caused by gravity in mounting. The uncoated surface of the samples was measured to avoid interferometric phase errors resulting from the coating. Film stresses based on these surface measurements were compared to those carried out on 310-mm-diam \times 14-mm-thick fused-silica substrates measured on an 18-in. Zygo interferometer, with calculated stresses agreeing to within ± 8 MPa. Film stresses were also compared to measurements taken in a custom vacuum cell on the Zygo New View; vacuum film stresses were measured to be approximately 8 MPa more tensile than those determined in a

nitrogen environment. Given the relative difficulty in making in-vacuum measurements, this shift in determined film stress was considered acceptable at this time.

Laser-damage testing was performed using 1-ns pulses at a wavelength of 1053 nm. The irradiation spot size, illuminated by a 2-m-focal-length lens, was 600 mm, making it possible to use fluences up to 100 J/cm². The sample was inspected under 110× magnification using dark-field microscopy, with an observable change in the surface being defined as damage. Testing may be targeted on defects present in the coating, as a means of identifying the weakest points in the film structure, or on sites that appear pristine, as a means of evaluating the maximum-possible damage threshold for a clean substrate and zero-particulate process. Modes of testing included 1-on-1, where each site on the substrate is illuminated only once, and N-on-1, where the fluence on a given site is gradually ramped through a series of shots until damage is observed.¹⁶

Results and Discussion

The goal of this work is to alter the tensile stress in the hafnia/silica multilayer coatings, shifting it to a low-magnitude compressive stress to eliminate the risk of cracking the coating while minimizing substrate deformation. Observations of current hafnia/silica coatings in vacuum have indicated that multilayers of greater-than-5-μm total film thickness consistently exhibit tensile stress failures in accordance with Eq. (2), providing the motivation for this effort. In addition, such coatings have tensile stresses of 80 MPa or greater, significantly deforming the substrate surface.^{4,9} Since polarizer coatings for use in the near-infrared cannot be realized with coatings of less than 5-μm thickness, the stress in the film must be shifted to a more compressive state.⁴

Evaporated alumina films have been reported in the literature as both tensile and compressive.^{11,17} The films being studied were found to have a tensile stress when deposited as a monolayer, with a stress of the order of 70±15 MPa. This would suggest alumina is not a viable material for compensation of tensile stresses in high-damage-threshold coatings since it would not offset the tensile stress generated in high-refractive-index hafnia layers. Composite film stresses in hafnia/silica multilayers, however, were tensile, but alumina/silica multilayers remained quite compressive. This could in part be a result of the magnitude of the tensile stress in alumina being less than that in hafnia, allowing it to be compensated by the compressive silica stress.

The film stresses as measured in the hafnia/silica multilayers, alumina/silica multilayers, and the hafnia/alumina/silica (hybrid)

multilayers indicate an unexpected interaction between the different layer materials. The hybrid three-material coating design is more compressive than either of the two-material designs; given the relative proportion of materials in each design, this should not be possible in order for Eq. (5) to be valid for all coatings using comparable stress values for the materials in each. This suggests that a modification to Eq. (5) is necessary, possibly to account for inhomogeneous layer stresses and/or interfacial effects.¹⁸ Either effect will be a function of the number of interfaces of the given material, so Eq. (5) is modified to a form

$$\sigma_{\text{total}} = \frac{\sigma_{\text{H}}T_{\text{H}} + \sigma_{\text{L}}T_{\text{L}} + \sigma_{\text{A}}T_{\text{A}}}{T_{\text{H}} + T_{\text{L}} + T_{\text{A}}} + \sigma_{\text{H/L}}I_{\text{H/L}} + \sigma_{\text{A/L}}I_{\text{A/L}}, \quad (6)$$

where $\sigma_{\text{H/L}}$ and $\sigma_{\text{A/L}}$ are the stresses resulting from interfacial and film-growth effects at each of the hafnia/silica ($I_{\text{H/L}}$) and alumina/silica ($I_{\text{A/L}}$) interfaces, respectively. The number of interfaces in the coating design is counted for each combination of materials, and since both hafnia and alumina have silica layers above and below each layer, the directional dependence is eliminated.

It is possible to determine values for each of the five stresses included in Eq. (6) by establishing a linear series of five equations for simultaneous solution. The six depositions provide a means of calculating the stresses six times, by eliminating one of the depositions from consideration for each calculation. The calculation is most readily constructed in matrix form, for five given depositions:

$$\begin{pmatrix} T_{\text{H1}} & T_{\text{L1}} & T_{\text{A1}} & I_{\text{H/L1}} & I_{\text{A/L1}} \\ T_{\text{H2}} & T_{\text{L2}} & T_{\text{A2}} & I_{\text{H/L2}} & I_{\text{A/L2}} \\ T_{\text{H3}} & T_{\text{L3}} & T_{\text{A3}} & I_{\text{H/L3}} & I_{\text{A/L3}} \\ T_{\text{H4}} & T_{\text{L4}} & T_{\text{A4}} & I_{\text{H/L4}} & I_{\text{A/L4}} \\ T_{\text{H5}} & T_{\text{L5}} & T_{\text{A5}} & I_{\text{H/L5}} & I_{\text{A/L5}} \end{pmatrix} \times \begin{pmatrix} \sigma_{\text{H}} \\ \sigma_{\text{L}} \\ \sigma_{\text{A}} \\ \sigma_{\text{H/L}} \\ \sigma_{\text{A/L}} \end{pmatrix} = \begin{pmatrix} \sigma_{\text{total1}} \\ \sigma_{\text{total2}} \\ \sigma_{\text{total3}} \\ \sigma_{\text{total4}} \\ \sigma_{\text{total5}} \end{pmatrix}, \quad (7)$$

where σ_{total_i} are the measured stress values of the multilayer coatings, after having stabilized with age. Rearranging this for solution yields

$$\begin{pmatrix} T_{\text{H1}} & T_{\text{L1}} & T_{\text{A1}} & I_{\text{H/L1}} & I_{\text{A/L1}} \\ T_{\text{H2}} & T_{\text{L2}} & T_{\text{A2}} & I_{\text{H/L2}} & I_{\text{A/L2}} \\ T_{\text{H3}} & T_{\text{L3}} & T_{\text{A3}} & I_{\text{H/L3}} & I_{\text{A/L3}} \\ T_{\text{H4}} & T_{\text{L4}} & T_{\text{A4}} & I_{\text{H/L4}} & I_{\text{A/L4}} \\ T_{\text{H5}} & T_{\text{L5}} & T_{\text{A5}} & I_{\text{H/L5}} & I_{\text{A/L5}} \end{pmatrix}^{-1} \times \begin{pmatrix} \sigma_{\text{total1}} \\ \sigma_{\text{total2}} \\ \sigma_{\text{total3}} \\ \sigma_{\text{total4}} \\ \sigma_{\text{total5}} \end{pmatrix} = \begin{pmatrix} \sigma_{\text{H}} \\ \sigma_{\text{L}} \\ \sigma_{\text{A}} \\ \sigma_{\text{H/L}} \\ \sigma_{\text{A/L}} \end{pmatrix}. \quad (8)$$

The six possible solutions, based on elimination of each of depositions 1–6, are summarized in Table 126.VIII.

Table 126.VIII. Solutions to the system of equations describing the individual stress contributions. Only solutions B and F fit the constraints of the problem.

| | A | B | C | D | E | F |
|----------------|---------|--------|---------|-----------------------|-----|--------|
| σ_H | -200.5 | 234.3 | -5869.5 | -252.3 | NaN | 246.1 |
| σ_L | 283.9 | -92.8 | 4367.0 | 248.4 | NaN | -81.0 |
| σ_A | -1058.0 | -622.9 | -5024.7 | 1.2×10^{18} | NaN | -630.9 |
| $\sigma_{H/L}$ | -0.8 | 0.6 | -8.9 | 0.1 | NaN | 0.1 |
| $\sigma_{A/L}$ | 3.9 | 3.9 | -0.8 | -7.9×10^{15} | NaN | 3.9 |

Analysis of the results shows a number of the mathematical solutions do not fit the parameters of the problem. Based on single-layer stress measurements, σ_H is expected to be of the order of 200 MPa and σ_L is of the order of -80 MPa. Only solutions B and F appear to fit the constraints of the problem. While the solutions are very similar, the calculated stress in the alumina films is excessively compressive; this may be due to inhomogeneous stresses that are poorly described by Eq. (6), errors in the stress measurements, or other effects. Given that the magnitude of the stress in the alumina layers is expected to be a maximum of ± 100 MPa, rather than the -600 MPa calculated, the modeled values fit the mathematical constraints of the system of equations without necessarily identifying the physical stress contributions accurately.¹¹ Using an average solution of B and F for coating designs containing different numbers of alumina layers, the determined stress is compared to measured values for selected coatings in Fig. 126.51. While the various stress contributions may not be appropriately distributed among the film materials, the model does provide an indication of the trends in expected film stress for a composite hafnia/silica/alumina coating.

The previous results were used to predict the stresses likely to be achieved for two additional coating depositions, with designs $\{(HL)^3 [AL(HL)^3]^3 A2L\}$ designated sample #7 and $\{[AL(HL)^2]^5 A2L\}$ designated #8, where A, L, and H represent quarter-wave optical thicknesses at 1053 nm of alumina, silica, and hafnia, respectively, coefficients indicate a multiple of quarter-wave thickness, and superscripts signify the repetition of that portion of the coating design. The key difference with these hybrid designs is the alteration of the alumina content and the number of alumina/silica interfaces. Calculation of the expected film stress upon aging, using an average of solutions B and F, yields stresses of -11 MPa for #7 and -49 MPa for #8. Calculated stresses based on the measured surface flatness of samples #7 and #8 resulted in -34.5 MPa and -77 MPa, respectively, in both instances understating the compressive stress in the film. While the inaccuracy in the model's predic-

tion is undesirable, the presence of additional compressive stress avoids the risk of tensile stress failure.

The developed model provided general trends for the stress in the film but yielded errors in the predicted stress of -23.5 MPa and -28 MPa in samples #7 and #8. While efforts have been taken to account for the stresses in each material and any differences in stresses attributed to the number of interfaces, no allowance has been made for the potential modification of the stress in one material resulting from the presence of a different material in the multilayer coating. In particular, alumina has been shown to inhibit diffusion of water; it is likely that the presence of alumina layers influences the hydrolysis of silica, with the aging of the film to a more-tensile state over time being largely avoided.^{4,6} Refining the model to include such effects would require that all samples contain similar materials, and that the stress in any given layer be a function of the layers above it. The complexity of the model would increase significantly, in order to provide a functional dependence of the stress in each layer to all layers to the incident side, as well as the relative porosity. It is currently expected that such complexity is necessary, however, to fully describe the influence of alumina on the stresses in a hafnia/silica film.

It is suggested by the observed stresses that the changes in coating stress caused by the inclusion of alumina layers are a result of the reduced diffusion of water through the coating

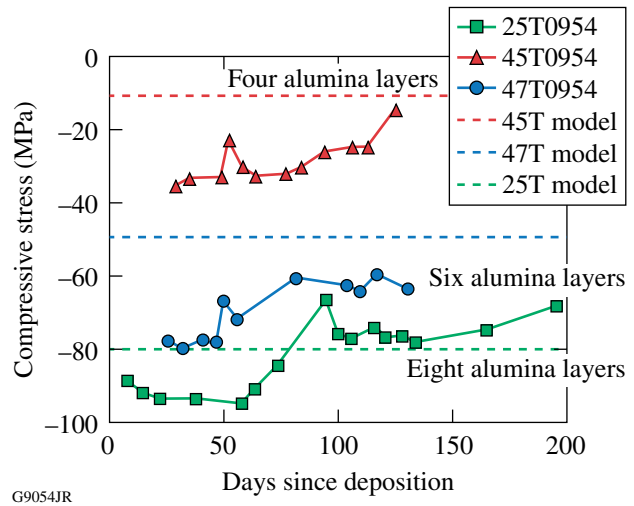
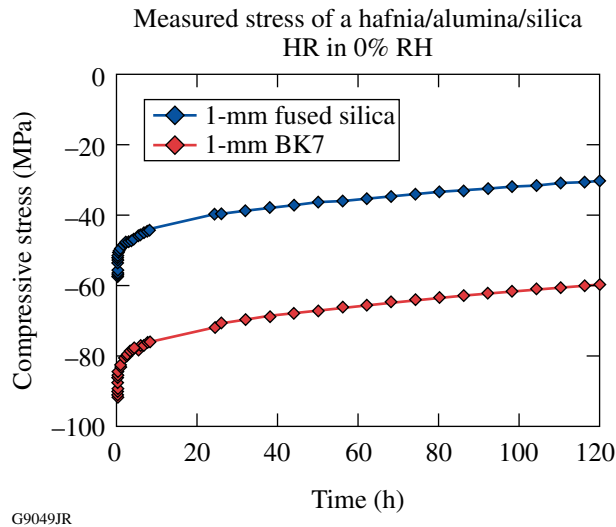


Figure 126.51 Influence of the number of alumina layers on the resulting stress in the multilayer coating. Use of a greater proportion of alumina instead of hafnia shifts the composite multilayer stress more compressively, making the coating suitable for use in a dry or vacuum environment.

structure. As shown in Fig. 126.52, the stress in an alumina/hafnia/silica coating exhibits a very slow drift as the coating is dried in a nitrogen-purged environment. This leads to a strong time dependence for all measured values of stress in order to stabilize the coating performance as much as possible. This uncertainty makes it very difficult to precisely determine the stress of coatings containing alumina since even after a week of drying time, the stress is not fully stabilized.



G9049JR

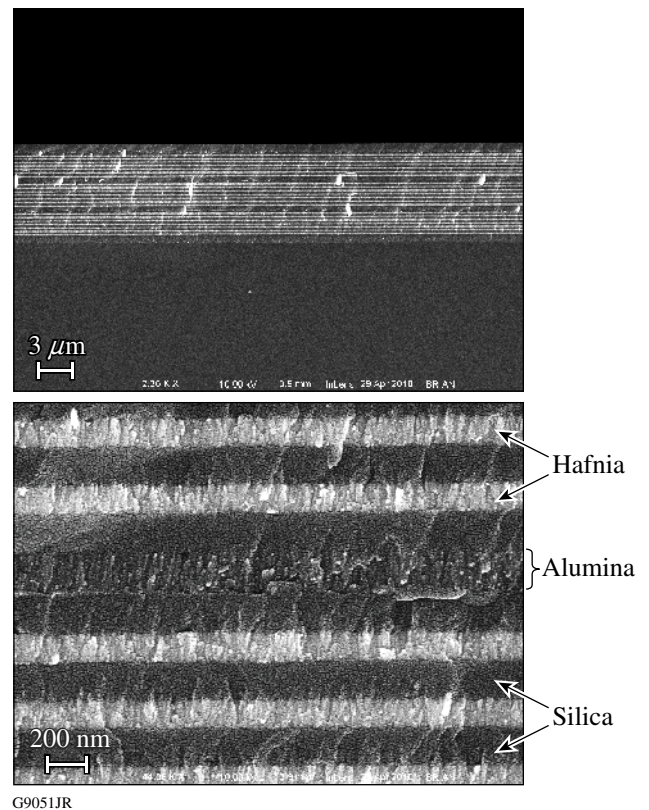
Figure 126.52

Change in stress in an alumina/silica coating as a function of time in dry nitrogen. Note that the stress changes quite slowly, leading to instability in the optical performance over an extended period of time since the surface flatness continues to change.

Implementation

A key advantage of this type of coating modification is that it can be readily performed in a standard evaporation system with minimal equipment changes required. This process was implemented in a 1.8-m coating chamber to alter the stress in a 0.9-m-aperture polarizer coating for use in vacuum on the OMEGA EP Laser System, as previously produced with evaporated hafnia/silica.⁴ To integrate this process, the standard six-pocket electron-beam gun used for hafnium metal evaporation was replaced with an EB Sources large-capacity, 12-pocket electron-beam gun, providing additional capacity for alumina evaporation. All deposition monitoring was performed with weighted averaging using an Inficon IC5 and three SensorsTech cartridge-type quartz crystal monitors mounted under stationary uniformity-correction masks, with the substrate mounted in a counter-rotating planetary rotation system.^{19,20} Silica was deposited using granular silica in a continuously rotating EB Sources large-capacity, pan-type electron-beam gun.

The original 48-layer polarizer coating design developed for this application was replaced with a 50-layer design containing four alumina layers, with all alumina layers adjoining only silica layers.⁴ The alumina layers are nominally one quarter-wave optical thickness, except the layer on the substrate, which is approximately three quarter-waves in optical thickness. The coating design was fully optimized with Optilayer refinement to maximize the photometric coating performance.²¹ The alumina layers were inserted every 16th layer, such that the layer on the substrate was alumina and the final high-index layer was alumina. The outermost layer of the coating remained a thick silica layer of greater than one half-wave optical thickness. The overall coating thickness was $9.1 \mu\text{m}$, requiring approximately 10 h of deposition time. Cross-sectional scanning electron microscope images of the completed polarizer coating are shown in Fig. 126.53, with the alumina layers appearing very similar to the surrounding silica layers; only the film microstructure differentiates it from the adjoining layers.



G9051JR

Figure 126.53

Cross-sectional scanning electron micrographs of the polarizer coating modified with four alumina layers. The alumina layers appear to have a more-columnar structure than the surrounding silica layers, which appear amorphous. The hafnia layers appear columnar and much brighter in the image.

Coating performance was measured using a laser-based photometer, providing a highly collimated source, a precise angle of incidence, and high polarization contrast. The performance of this polarizer is shown in Fig. 126.54, indicating p -polarized transmission of greater than 98% through the component over an angular range of nearly 9° incidence; polarizer contrast, defined as T_p/T_s , exceeds 200:1 over 8° of this range. In wavelength space, this component has a useful bandwidth of 30 nm after accounting for slight uniformity errors over the 0.9-m aperture and installation alignment tolerances.

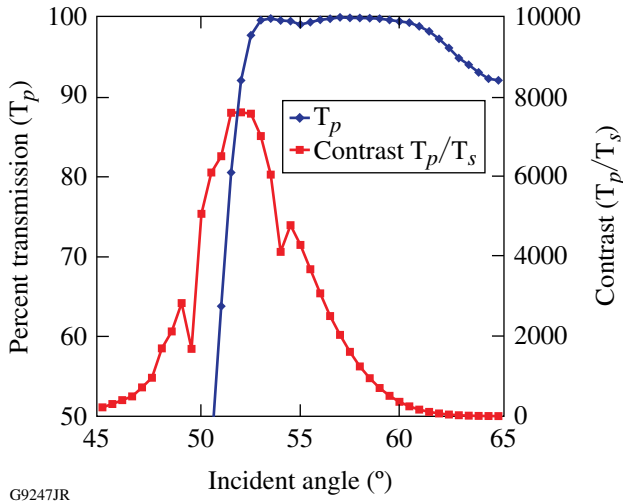


Figure 126.54

Photometric measurement of short-pulse polarizer Z011 installed on OMEGA EP, utilizing alumina for stress control in a dry environment. This polarizer coating provides high transmission and contrast over a wavelength range of 30 nm with incident 1053-nm light.

Laser-damage testing of this coating using a 1053-nm laser with s -polarized light in a 1:1 mode indicated damage thresholds of greater than 74 J/cm² when tested at 1 ns (clean sites, with no testing performed above this fluence) and 44 J/cm² when targeting defects visible using dark-field microscopic inspection.¹⁶ Transmitted laser-damage tests in p -polarization remained above 20 J/cm². Stress measurements indicate the coating on a BK7 substrate maintains a compressive stress of approximately -100 MPa when measured in an N₂-purged environment at 0% relative humidity. This controlled compressive stress provides a coating that will not fail in tension, even when used in a vacuum environment. As noted previously, the slow drift in film stress as a function of drying time makes it very difficult to accurately determine the stress, with an expected measurement uncertainty of ± 20 MPa.

While this coating effort was highly effective—far exceeding the performance requirements for this component—the use of alumina poses significant challenges to the successful implementation in the laser system. The diffusion-barrier properties of the coating significantly restrict the movement of water into and out of the film structure, leading to very slow changes in the coating stress and photometric performance as the relative humidity changes. This change in photometric performance was measured for the polarizer coating, initially stored in an ambient-humidity environment, over a period of multiple days in an N₂-purged, 0%-relative-humidity environment as shown in Fig. 126.55. The coating performance undergoes a substantial change in photometric performance, requiring days or even weeks of recovery time if the optic is stored for long periods in an ambient-humidity environment. Provided the water penetration is slow, short exposure times during installation and alignment can be overcome relatively quickly.

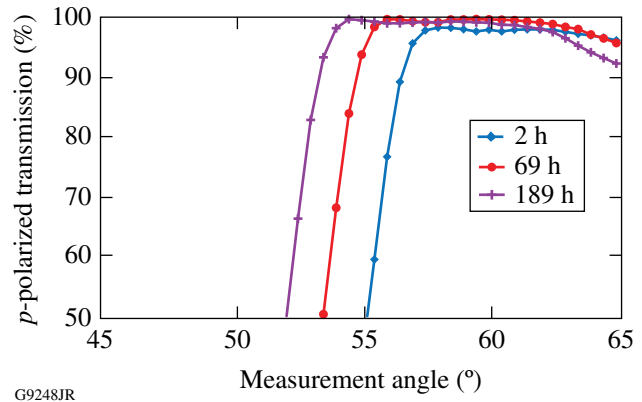
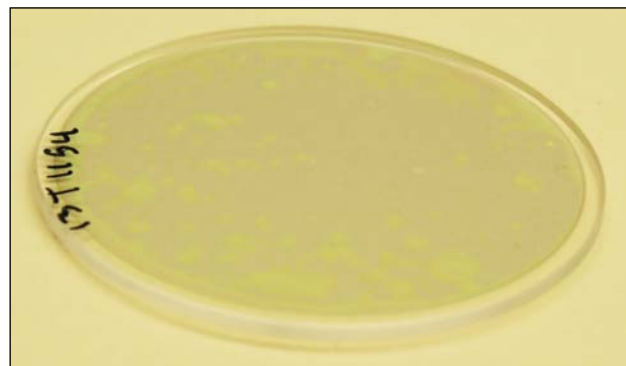


Figure 126.55

Change in photometric performance of a hafnia/silica polarizer coating containing alumina layers. Note that similar to the stress changes in Fig. 126.52, the optical performance of the coating changes significantly over an extended period of time in a dry nitrogen environment. In this case, measurements were performed over a period of approximately 8 days.

The slow drift in performance may be overcome by maintaining the storage and transport of such coatings in a dry atmosphere, while minimizing exposure to humid air during installation and use. Initial evaluation suggests the movement of water into the coating also takes place over a long time scale, as evidenced by the “mottled” appearance that develops as the coating is exposed to moist, ambient air. It is understood that moisture penetration through defect sites in the coating leads to the localized exchange of water for void in the coating, resulting in an increase in the optical thickness and a change

in the color of the coating as shown in Fig. 126.56. Over time, diffusion of the water within the coating structure will bring the water content in the coating to equilibrium, with the coating once again appearing to be a consistent color as the individual moisture-penetration sites through the diffusion barrier coalesce, eliminating the mottled appearance. Alumina is a highly effective diffusion barrier to water penetration and, as such, may require many days of exposure to moist air before the coating once again appears uniform. As shown in Fig. 126.56, a hafnia/silica coating containing alumina barrier layers continues to exhibit a mottled appearance 2 days after deposition. The alumina is quite dense, with isolated defects providing a path for the moisture through the layer, with the surrounding hafnia/silica layers in the multilayer remaining relatively porous.



G9249JR

Figure 126.56
Multilayer dielectric coating containing alumina layers 2 days after deposition. Note the “mottled” appearance of the coating color in reflection, indicating an irregular absorption of water into the coating structure.

Conclusions

The inclusion of alumina layers in standard hafnia/silica high-reflectance coatings leads to a significantly more compressive overall film stress, enabling one to use such coatings in vacuum environments on low-thermal-expansion substrates without the risk of tensile-stress failure causing cracking, or crazing, of the film. The use of multiple designs incorporating different numbers of layers, numbers of interfaces, and thicknesses of the constituent materials provides the opportunity to determine the individual contributions of hafnia, silica, and alumina to the overall stress in the multilayer optical coating—a contribution found to be very different than that expected by monolayer stresses. Additionally, interfacial

effects were incorporated to account for the inhomogeneous film stresses as each layer was formed. Such calculations, while likely not appropriately allocating the stress contributions of each material, have been demonstrated to provide a somewhat predictive ability for arbitrary multilayer coating designs. The stress in hafnia/silica coating designs, including alumina stress compensation layers, has been demonstrated to agree with theoretical predictions, and hafnia/silica/alumina films can be manufactured without degradation of spectral performance or laser-damage resistance. This process was used to produce large-aperture polarizer coatings for use in an N_2 -purged environment on OMEGA EP. It has been shown that such coating designs may be readily implemented using standard electron-beam evaporation systems, are easily scaled to large-aperture substrates, and provide a means of addressing the need for vacuum-use coatings in pulse-compressed laser systems. The slow diffusion of water in such coatings poses some difficulties in implementation, but this may be overcome by storage in a low-relative-humidity environment.

ACKNOWLEDGMENT

The authors wish to express their appreciation to Alex Maltsev for his efforts on the fabrication of extremely high quality, high-aspect-ratio substrates for this study.

This work was supported by the U.S. Department of Energy Office of Inertial Confinement Fusion under Cooperative Agreement No. DE-FC52-08NA28302, the University of Rochester, and the New York State Energy Research and Development Authority. The support of DOE does not constitute an endorsement by DOE of the views expressed in this article.

REFERENCES

1. R. Chow *et al.*, *Appl. Opt.* **32**, 5567 (1993).
2. J. F. Anzellotti, D. J. Smith, R. J. Sczupak, and Z. R. Chrzan, in *Laser-Induced Damage in Optical Materials: 1996*, edited by H. E. Bennett *et al.* (SPIE, Bellingham, WA, 1997), Vol. 2966, pp. 258–264.
3. J. B. Oliver, J. Howe, A. Rigatti, D. J. Smith, and C. Stolz, in *Optical Interference Coatings*, OSA Technical Digest (Optical Society of America, Washington, DC, 2001), Paper ThD2.
4. J. B. Oliver, A. L. Rigatti, J. D. Howe, J. Keck, J. Szczepanski, A. W. Schmid, S. Papernov, A. Kozlov, and T. Z. Kosc, in *Laser-Induced Damage in Optical Materials: 2005*, edited by G. J. Exarhos *et al.* (SPIE, Bellingham, WA, 2005), Vol. 5991, pp. 394–401.
5. J. B. Oliver, S. Papernov, A. W. Schmid, and J. C. Lambropoulos, in *Laser-Induced Damage in Optical Materials: 2008*, edited by G. J. Exarhos *et al.* (SPIE, Bellingham, WA, 2008), Vol. 7132, p. 71320J.
6. H. Leplan *et al.*, *J. Appl. Phys.* **78**, 962 (1995).

7. D. J. Smith, M. McCullough, C. Smith, T. Mikami, and T. Jitsuno, in *Laser-Induced Damage in Optical Materials: 2008*, edited by G. J. Exarhos *et al.* (SPIE, Bellingham, WA, 2008), Vol. 7132, p. 71320E.
8. E. Lavastre *et al.*, in *Optical Interference Coatings*, OSA Technical Digest (Optical Society of America, Washington, DC, 2004), Paper TuF3.
9. J. B. Oliver, P. Kupinski, A. L. Rigatti, A. W. Schmid, J. C. Lambropoulos, S. Papernov, A. Kozlov, and R. D. Hand, in *Optical Interference Coatings*, OSA Technical Digest (Optical Society of America, Washington, DC, 2010), Paper WD6.
10. M. Henyk, D. Wolfram, and J. Reif, *Appl. Surf. Sci.* **168**, 263 (2000).
11. M. Reichling, A. Bodemann, and N. Kaiser, *Thin Solid Films* **320**, 264 (1998).
12. R. Thielsch, A. Gatto, J. Herber, and N. Kaiser, *Thin Solid Films* **410**, 86 (2002).
13. G. G. Stoney, *Proc. R. Soc. Lond. A* **82**, 172 (1909).
14. J. W. Hutchison and T. Y. Wu, eds. *Advances in Applied Mechanics*, Vol. 29 (Academic Press, San Diego, CA, 1992).
15. M. Ohring, *Materials Science of Thin Films: Deposition and Structure*, 2nd ed. (Academic Press, San Diego, 2002), pp. 723–730.
16. S. Papernov and A. W. Schmid, *J. Appl. Phys.* **82**, 5422 (1997).
17. J. Proost and F. Spaepen, *J. Appl. Phys.* **91**, 204 (2002).
18. Y. Shen *et al.*, *Rare Met. Mater. Eng.* **36**, 412 (2007).
19. J. B. Oliver and D. Talbot, *Appl. Opt.* **45**, 3097 (2006).
20. D. J. Smith, A. Staley, R. Eriksson, and G. Algar, in *Proceedings of the 41st Annual Technical Conference of the Society of Vacuum Coaters* (Society of Vacuum Coaters, Albuquerque, NM, 1998), pp. 193–196.
21. A. V. Tikhonravov and M. K. Trubetskov, *OptiLayer Thin Film Software*, Optilayer Ltd., <http://www.optilayer.com> (9 June 2005).

Publications and Conference Presentations

Publications

- W. R. Donaldson, D. N. Maywar, J. H. Kelly, and R. E. Bahr, "Measurement of the Self-Phase Modulation-Induced Bandwidth in a 30 kJ Class Laser Amplifier Chain," *J. Opt. Soc. Am. B* **28**, 445 (2011).
- D. H. Froula, S. H. Glenzer, N. C. Luhmann, and J. Sheffield, *Plasma Scattering of Electromagnetic Radiation: Theory and Measurement Techniques* (Elsevier, Burlington, MA, 2011).
- M. C. Ghilea, D. D. Meyerhofer, and T. C. Sangster, "A Freon-Filled Bubble Chamber for Neutron Detection in Inertial Confinement Fusion Experiments," *Rev. Sci. Instrum.* **82**, 033305 (2011).
- M. J. Guardalben and L. J. Waxer, "Improvements to Long-Pulse System Performance and Operational Efficiency on OMEGA EP," in *High Power Lasers for Fusion Research*, edited by A. A. S. Awwal, A. M. Dunne, H. Azechi, and B. E. Kruschwitz (SPIE, Bellingham, WA, 2011), Vol. 7916, Paper 79160G.
- J. B. Oliver, P. Kupinski, A. L. Rigatti, A. W. Schmid, J. C. Lambropoulos, S. Papernov, A. Kozlov, J. Spaulding, D. Sadowski, Z. R. Chrzan, R. D. Hand, D. R. Gibson, I. Brinkley, and F. Placido, "Large-Aperture Plasma-Assisted Deposition of Inertial Confinement Fusion Laser Coatings," *Appl. Opt.* **50**, C19 (2011).
- P. B. Radha, C. Stoeckl, V. N. Goncharov, J. A. Delettrez, D. H. Edgell, J. A. Frenje, I. V. Igumenshchev, J. P. Knauer, J. A. Marozas, R. L. McCrory, D. D. Meyerhofer, R. D. Petrasso, S. P. Regan, T. C. Sangster, W. Seka, and S. Skupsky, "Triple-Picket Warm Plastic-Shell Implosions on OMEGA," *Phys. Plasmas* **18**, 012705 (2011).
- J. M. Soures, "Opportunities for Inertial Fusion and High-Energy-Density Physics Research at the National Laser Users' Facility," in *High Power Lasers for Fusion Research*, edited by A. A. S. Awwal, A. M. Dunne, H. Azechi, and B. E. Kruschwitz (SPIE, Bellingham, WA, 2011), Vol. 7916, Paper 791603.
- L. Steponaviciene, J. Sulcas, A. Jukna, G. Jung, V. Plausinaitiene, A. Abrutis, A. Maneikis, M. Gong, and R. Sobolewski, "Investigation of Vortex Density in Laser-Written Π -Shaped Channel of YBCO Bridge by Means of I - V Dependences," *Acta Phys. Pol. A* **119**, 180 (2011).
- J. Sulcas, L. Steponaviciene, A. Jukna, G. Jung, V. Plausinaitiene, A. Abrutis, M. Gong, and R. Sobolewski, "Current Distribution in Y-Ba-Cu-O Superconducting Microbridges Containing Π -Shaped Channel for Easy Vortex Motion," *Acta Phys. Pol. A* **119**, 183 (2011).
- W. Wang, T. B. Jones, and D. R. Harding, "On-Chip Double Emulsion Droplet Assembly Using Electrowetting-on-Dielectric and Dielectrophoresis," *Fusion Sci. Technol.* **59**, 240 (2011).
- S. K. H. Wei and S. H. Chen, "Spatially Resolved Lasers Using a Glassy Cholesteric Liquid Crystal Film with Lateral Pitch Gradient," *Appl. Phys. Lett.* **98**, 111112 (2011).
- S. K.-H. Wei, L. Zeng, K. L. Marshall, and S. H. Chen, "Room-Temperature Processing of π -Conjugated Oligomers into Uniaxially Oriented Monodomain Films on Coumarin-Based Photoalignment Layers," *J. Polym. Sci. B, Polym. Phys.* **49**, 725 (2011).

Forthcoming Publications

T. R. Boehly, V. N. Goncharov, W. Seka, M. A. Barrios, P. M. Celliers, D. G. Hicks, G. W. Collins, S. X. Hu, J. A. Marozas, and D. D. Meyerhofer, "Velocity and Timing of Multiple Spherically Converging Shock Waves in Deuterium," to be published in *Physical Review Letters*.

J. Bromage, J. M. Fini, C. Dorrer, and J. D. Zuegel, "Characterization and Optimization of Yb-Doped Photonic-Crystal Fiber Rod Amplifiers Using Spatially Resolved Spectral Interferometry," to be published in *Applied Optics*.

D. E. Fratanduono, T. R. Boehly, M. A. Barrios, D. D. Meyerhofer, J. H. Eggert, R. F. Smith, D. G. Hicks, P. M. Celliers, D. G. Braun, and G. W. Collins, "Refractive Index of Lithium Fluoride Ramp Compressed to 800 GPa," to be published in the *Journal of Applied Physics*.

M. C. Ghilea, D. D. Meyerhofer, and T. C. Sangster, "Neutron-Induced Nucleation Inside Bubble Chambers Using Freon 115 as the Active Medium," to be published in *Nuclear Instruments and Methods*.

S. X. Hu, "Attosecond Timing the Ultrafast Charge-Transfer Process in Atomic Collisions," to be published in *Physical Review A*.

I. Íñiguez-de-la-Torre, S. Purohit, V. Kaushal, M. Margala, M. Gong, R. Sobolewski, D. Wolpert, P. Ampadu, T. González, and J. Mateos, "Exploring Digital Logic Design Using Nanometer-Scale Devices Through Monte Carlo Simulations," to be published in *IEEE Transactions on Nanotechnology*.

D. D. Meyerhofer, R. L. McCrory, R. Betti, T. R. Boehly, D. T. Casey, T. J. B. Collins, R. S. Craxton, J. A. Delettrez, D. H. Edgell, R. Epstein, K. A. Fletcher, J. A. Frenje, Y. Yu. Glebov, V. N. Goncharov, D. R. Harding, S. X. Hu, I. V. Igumenshchev, J. P. Knauer, C. K. Li, J. A. Marozas, F. J. Marshall, P. W. McKenty, P. M. Nilson, S. P. Padalino, R. D. Petrasso, P. B. Radha, S. P. Regan, T. C. Sangster, F. H. Séguin, W. Seka, R. W. Short, D. Shvarts, S. Skupsky, J. M. Soures, C. Stoeckl, W. Theobald, and B. Yaakobi, "High-Performance Inertial Confinement Fusion Target Implosions on OMEGA," to be published in *Nuclear Fusion*.

C. Miao, R. Shen, M. Wang, S. N. Shafrir, H. Yang, and S. D. Jacobs, "Rheological Study of Aqueous Magnetorheological Fluid Using Dual Oxide-Coated Carbonyl Iron Particles," to be published in the *Journal of the American Ceramic Society*.

P. M. Nilson, A. A. Solodov, J. F. Myatt, W. Theobald, P. A. Jaanimagi, L. Gao, C. Stoeckl, R. S. Craxton, J. A. Delettrez, B. Yaakobi, J. D. Zuegel, B. E. Kruschwitz, C. Dorrer, J. H. Kelly, K. U. Akli, P. K. Patel, A. J. Mackinnon, R. Betti, T. C. Sangster, and D. D. Meyerhofer, "Scaling Hot-Electron Generation to Long-Pulse, High-Intensity Laser-Solid Interactions," to be published in *Physics of Plasmas*.

P. M. Nilson, W. Theobald, C. Mileham, C. Stoeckl, J. F. Myatt, J. A. Delettrez, J. MacFarlane, I. A. Begishev, J. D. Zuegel, R. Betti, T. C. Sangster, and D. D. Meyerhofer, "Target-Heating Effects on the $K_{\alpha 1,2}$ -Emission Spectrum from Solid Targets Heated by Laser-Generated Hot Electrons," to be published in *Physics of Plasmas*.

A. V. Okishev, "Characterization of Highly Stable, Mid-IR, GaSb-Based Laser Diodes," to be published in *Optics Express*.

P. B. Radha, R. Betti, T. R. Boehly, J. A. Delettrez, D. H. Edgell, V. N. Goncharov, I. V. Igumenshchev, J. P. Knauer, J. A. Marozas, F. J. Marshall, R. L. McCrory, D. D. Meyerhofer, S. P. Regan, T. C. Sangster, W. Seka, S. Skupsky, A. A. Solodov, C. Stoeckl, W. Theobald, J. A. Frenje, D. T. Casey, C. K. Li, and R. D. Petrasso, "Inertial Confinement Fusion Using the OMEGA Laser System," to be published in *IEEE Transactions on Plasma Science*.

W. Theobald, A. A. Solodov, C. Stoeckl, K. S. Anderson, R. Betti, T. R. Boehly, R. S. Craxton, J. A. Delettrez, C. Dorrer, J. A. Frenje, V. Yu. Glebov, H. Habara, K. A. Tanaka, J. P. Knauer, F. J. Marshall, K. L. Marshall, D. D. Meyerhofer, P. M. Nilson, P. K. Patel, H. Chen, T. C. Sangster, W. Seka, N. Sinenian, T. Ma, F. N. Beg, E. Giraldez, and R. B. Stephens, "Initial Cone-in-Shell Target Fast-Ignition Experiments on OMEGA," to be published in *Physics of Plasmas*.

Conference Presentations

The following presentations were made at LASE—SPIE Photonics West, San Francisco, CA, 22–27 January 2011:

M. J. Guardalben and L. J. Waxer, “Improvements to Long-Pulse System Performance and Operational Efficiency on OMEGA EP.”

J. M. Soures, “Opportunities for Inertial Fusion and High-Energy-Density Physics Research at the National Laser Users’ Facility.”

J. D. Zuegel and J. Bromage, “Lasers at the University of Rochester’s Laboratory for Laser Energetics: Laser Fusion to Ultra-Intense Lasers,” ETH-Hönggerberg Seminar, Zurich, Switzerland, 10 February 2011.

The following presentations were made at Advanced Solid-State Photonics, Istanbul, Turkey, 13–16 February 2011:

J. Bromage, C. Dorrer, and J. D. Zuegel, “Temporal Contrast Measurements of a Noncollinear Optical Parametric Amplifier Seeded by White-Light Continuum.”

R. Xin and J. D. Zuegel, “All-Fiber Regenerative Amplifier for Nanosecond Optical Pulses at 1053 nm.”

J. D. Zuegel, M. J. Shoup III, J. H. Kelly, and C. Frederickson, “Novel Actively Cooled Split-Disk Nd:Glass Laser Amplifier for High-Energy Applications with Improved Repetition Rate.”

P. M. Nilson, R. Betti, J. A. Delettrez, L. Gao, P. A. Jaanimagi, J. F. Myatt, T. C. Sangster, A. A. Solodov, C. Stoeckl, W. Theobald, B. Yaakobi, J. D. Zuegel, A. J. MacKinnon, and P. K. Patel, “Hot-Electron Lifetime Measurements,” Fusion Science Center for Extreme States of Matter 10th Meeting, Rochester, NY, 7 March 2011.

The following presentations were made at the International Workshop on ICF Shock Ignition, Rochester, NY, 8–10 March 2011:

K. S. Anderson, R. Betti, P. W. McKenty, T. J. B. Collins, R. S. Craxton, R. Nora, A. A. Solodov, and L. J. Perkins, “Shock Ignition with Plastic-Ablator Cryogenic Shells on the NIF.”

K. S. Anderson, W. Theobald, C. Stoeckl, R. Betti, R. S. Craxton, J. A. Delettrez, O. V. Gotchev, V. Yu. Glebov, V. N. Goncharov, F. J. Marshall, D. N. Maywar, R. L. McCrory, D. D. Meyerhofer, R. Nora, P. B. Radha, W. Seka, T. C. Sangster, V. A. Smalyuk, B. Yaakobi, C. D. Zhou, J. A. Frenje, C. K. Li, F. H. Séguin, R. D. Petrasso, L. J. Perkins, M. Lafon, X. Ribeyre, G. Schurtz, A. Casner “60-Beam Shock-Ignition OMEGA Experiments and Simulations.”

R. Betti, “An Overview of Shock Ignition.”

T. J. B. Collins, J. A. Marozas, A. Shvydky, R. S. Craxton, and P. W. McKenty, “Polar-Drive Hot-Spot Ignition on the NIF.”

R. S. Craxton, P. W. McKenty, E. Bond, S. LePape, A. J. MacKinnon, P. A. Michel, and J. D. Moody, “Three-Dimensional Distributions of Deposited Energy and Scattered Light in NIF ‘Exploding-Pusher’ Polar-Drive Experiments.”

R. S. Craxton, L. Tucker, T. Mo, K. S. Anderson, R. Betti, L. J. Perkins, G. P. Schurtz, X. Ribeyre, and A. Casner, “Three-Dimensional Design of a 96-Beam NIF Target to Test the Compression Phase of Shock Ignition.”

T. J. Kessler, “Phase and Polarization Plates for NIF Polar Drive.”

J. A. Marozas, “Picket Pulses with 1-D Multi-FM Smoothing by Spectral Dispersion (SSD) for the NIF Drive.”

F. J. Marshall, P. B. Radha, and A. Shvydky, “Backlighting of OMEGA Polar-Drive Experiments.”

P. W. McKenty, R. S. Craxton, F. J. Marshall, A. Shvydky, R. Epstein, A. M. Cok, J. A. Marozas, T. J. B. Collins, S. Skupsky, C. Stoeckl, T. C. Sangster, M. J. Bonino,

R. Janezic, D. R. Harding, W. T. Shmayda, S. F. B. Morse, D. D. Meyerhofer, R. L. McCrory, A. Nikroo, J. D. Kilkenny, M. L. Hoppe, J. Fooks, A. J. MacKinnon, S. LePape, R. J. Wallace, D. K. Bradley, and G. A. Kyrala, "Results of Polar-Drive, Exploding-Pusher Shots on the NIF."

P. B. Radha, F. J. Marshall, R. S. Craxton, and A. Shvydky, "Results from Polar-Drive OMEGA Experiments."

A. Shvydky, P. W. McKenty, F. J. Marshall, R. S. Craxton, J. A. Marozas, R. Epstein, S. Skupsky, and R. L. McCrory, "Numerical Investigation of NIF Diagnostic Commissioning Experiments on OMEGA."

W. Theobald, M. Hohenberger, R. Nora, K. S. Anderson, R. Betti, T. R. Boehly, D. E. Fratanduono, J. A. Frenje, S. X. Hu, D. D. Meyerhofer, T. C. Sangster, W. Seka, C. Stoeckl, B. Yaakobi, A. Casner, X. Ribeyre, and G. Schurtz, "Shock-Ignition Experiments on OMEGA."

J. D. Zuegel, "Demonstrating Polar-Drive Smoothing Technology for the NIF on OMEGA EP"

J. E. Schoenly, W. Seka, and P. Rechmann, "Fluence Dependency of the 400-nm Ablation Rates of Supra- and Subgingival Dental Calculus," American Society of Laser Medicine and Surgery 2011 Annual Conference, Grapevine, TX, 30 March–3 April 2011.

